

Communicating with Transverse Modes of Light

by

Brandon Rodenburg

Submitted in Partial Fulfillment of the

Requirements for the Degree

Doctor of Philosophy

Supervised by Professor Robert W. Boyd

The Institute of Optics
Arts, Sciences and Engineering
Edmund A. Hajim School of Engineering and Applied Sciences

University of Rochester
Rochester, New York

2015

To my wonderful wife Liz:

Achievement unlocked!

Biographical Sketch

Brandon V. Rodenburg was born in Omaha, Nebraska in 1984. He attended Creighton University (Omaha, Nebraska) from which he graduated cum laude with both a bachelor of science in physics, and a bachelor of science major in mathematics in 2007. During his undergraduate program he performed research studying the dynamics of glass-forming liquids using photon correlation spectroscopy which led to publications in *Physical Review B* and *The Journal of Chemical Physics*, and for which he was awarded the Thomas Zepf Award for excellence in research, scholarship and service. In addition he won the 2006 – 2007 Alumni Award for best modern physics score on the Graduate Comprehensive Exam. He began his doctoral studies in optics at the University of Rochester in 2007, where he worked under the direction of Professor Robert W. Boyd.

List of Graduate Publications

- [1] R. W. Boyd, A. Jha, M. Malik, C. O’Sullivan, B. Rodenburg, and D. J. Gauthier. Quantum key distribution in a high-dimensional state space: exploiting the transverse degree of freedom of the photon. *Proceedings of SPIE* **7948**, 79480L–6. doi:10.1117/12.873491 (2011).
- [2] P. B. Dixon, G. Howland, K. Chan, C. O’Sullivan-Hale, B. Rodenburg, N. Hardy, J. H. Shapiro, D. S. Simon, A. V. Sergienko, R. W. Boyd, and J. Howell. Quantum ghost imaging through turbulence. *Physical Review A* **83**. doi:10.1103/PhysRevA.83.051803 (2011).
- [3] R. W. Boyd, B. Rodenburg, M. Mirhosseini, and S. M. Barnett. Influence of atmospheric turbulence on the propagation of quantum states of light using plane-wave encoding. *Optics Express* **19**, 18310. doi:10.1364/OE.19.018310 (2011).
- [4] K. Chan, D. S. Simon, A. V. Sergienko, N. Hardy, J. H. Shapiro, P. B. Dixon, G. Howland, J. Howell, J. Eberly, M. N. O’Sullivan, B. Rodenburg, and R. W. Boyd. Theoretical analysis of quantum ghost imaging through turbulence. *Physical Review A* **84**. doi:10.1103/PhysRevA.84.043807 (2011).
- [5] M. P. J. Lavery, D. Robertson, M. Malik, B. Rodenburg, J. Courtial, R. W. Boyd, and M. J. Padgett. The efficient sorting of light’s orbital angular momentum for optical communications. *Proceedings of SPIE* **8542**, 85421R. doi:10.1117/12.979934 (2012).
- [6] M. Malik, M. N. O’Sullivan, B. Rodenburg, M. Mirhosseini, J. Leach, M. P. J. Lavery, M. J. Padgett, and R. W. Boyd. Influence of atmospheric turbulence on optical communications using orbital angular momentum for encoding. *Optics Express* **20**, 13195. doi:10.1364/OE.20.013195 (2012).
- [7] B. Rodenburg, M. P. J. Lavery, M. Malik, M. N. O’Sullivan, M. Mirhosseini, D. J. Robertson, M. J. Padgett, and R. W. Boyd. Influence of atmospheric

- turbulence on states of light carrying orbital angular momentum. *Optics Letters* **37**, 3735. doi:10.1364/OL.37.003735 (2012).
- [8] M. Mirhosseini, O. S. Magaña Loaiza, C. Chen, B. Rodenburg, M. Malik, and R. W. Boyd. Rapid generation of light beams carrying orbital angular momentum. *Optics Express* **21**, 30196. doi:10.1364/OE.21.030196 (2013).
- [9] M. Mirhosseini, B. Rodenburg, M. Malik, and R. W. Boyd. Free-space communication through turbulence: a comparison of plane-wave and orbital-angular-momentum encodings. *Journal of Modern Optics* **61**, 43–48. doi:10.1080/09500340.2013.834084 (2014).
- [10] B. Rodenburg, M. Mirhosseini, M. Malik, O. S. Magaña Loaiza, M. Yanakas, L. Maher, N. K. Steinhoff, G. A. Tyler, and R. W. Boyd. Simulating thick atmospheric turbulence in the lab with application to orbital angular momentum communication. *New Journal of Physics* **16**, 033020. doi:10.1088/1367-2630/16/3/033020 (2014).
- [11] B. Rodenburg, M. Mirhosseini, O. S. Magaña Loaiza, and R. W. Boyd. Experimental generation of an optical field with arbitrary spatial coherence properties. *Journal of the Optical Society of America B* **31**, A51. doi:10.1364/JOSAB.31.000A51 (2014).
- [12] O. S. Magaña Loaiza, M. Mirhosseini, B. Rodenburg, and R. W. Boyd. Amplification of Angular Rotations Using Weak Measurements. *Physical Review Letters* **112**, 200401. doi:10.1103/PhysRevLett.112.200401 (2014).
- [13] M. Mirhosseini, O. S. Magaña Loaiza, M. N. O’Sullivan, B. Rodenburg, M. Malik, D. J. Gauthier, and R. W. Boyd. High-dimensional quantum cryptography with twisted light. arXiv:1402.7113 (2014).

Acknowledgments

English poet John Donne stated, “No man is an island.” This is true in life, and the road leading to this thesis has been no exception to this maxim. I am indebted to Prof. Robert W. Boyd for giving me the opportunity to work with him during my time in graduate school. I have learned so much about how to do good research and what it means to be a scientist under his mentorship. I’d also like to thank Prof. James R. Fienup, Prof. John Howell, and Prof. Carlos Stroud, for agreeing to serve on my committee and for providing valuable insight and discussions that helped hone and improve the quality of this work.

I’d also like to thank the fellow members of Prof. Boyd’s research group for creating such an excellent environment to work and grow, as well as for the many friendships that have developed from working together. I thank past members Dr. Aaron Schweinsberg, Dr. Petros Zerom, Dr. Heedeuk Shin, Prof. Zhimin Shi, Dr. Alex Radunsky, Dr. Mehul Malik, Prof. George Gehring, and Prof. Anand Jha. I especially want to thank Colin Malcolm O’Sullivan for taking me under his wing when I joined the group. Thank you for your wisdom from which I learned so much, and for your eternal patience with me

as I followed you around constantly questioning you and trying to help in the lab even when I lacked the experience to be of much use. And to Dr. Joe Vornehm, who had the misfortune to share an office with me and didn't have the heart to ever turn me away from the many hours of discussions that we had that distracted from his own work. To Dr. Andreas Liapis, one of the few people I've met whose love of film may be as great as my own, thanks for the many interesting discussions on science and culture. I also would like to thank the current members Mahmud Siddiqui, Boshen Gao, Robert Cross, and Mohammad Hashemi, and a special thanks to Mohammad Mirhosseini and Omar Magaña-Loaiza, with whom I've had the privilege of working for the last few years on numerous projects, we made one hell of a team.

Many of the projects I worked on were in close collaboration with others. I'd like to acknowledge Prof. Miles Padgett and his group, especially Dr. Martin Lavery, as well as Prof. Howell and his group, especially Dr. Ben Dixon and Dr. Gregory Howland. I'd also like to thank Dr. Glenn Tyler and Dr. Nicholas Steinhoff of the Optical Sciences Company. Thanks to Prof. Clifford Chan, Prof. Alexander V. Sergienko, Prof. Jeffrey H. Shapiro, Prof. Joeseeph Eberly, and Prof. Stephen M. Barnett.

I'd also like to acknowledge all those here at the Institute of Optics that make this such a wonderful institution. Thanks to all the faculty who taught me so much, and to the many friends that I've made, and to the hard working staff who I've worked with including Gina Kern, Lissa Cotter, Lori Russel, Maria Schnitzler, Gayle Thompson,

Betsy Benedict, Per Adamson, Noelene Votens, Kari Brick, and everyone else who works to keep things running so smoothly.

I am grateful to my family, especially my parents, Ed and Lynda Rodenburg; my brother Matthew Rodenburg and his family; my Grandparents, Jean and Gene Rodenburg and Doris and Joe Breglia; and my aunt and uncle, Karen and John Priebe, who for years put up with my constant questioning of everything. Thanks for not only putting up with me, but encouraging and supporting me all these years. Thanks to my parents-in-law, David and Paula Sowl, my brother-in-law Sam Sowl, and sister-in-law Chelae Williams and her family for accepting me into your family and treating me as your own.

Lastly I thank my wife, Liz, to whom this thesis is dedicated. You are the love of my life, you give meaning to all that I do, you are my strength when life is hard and my joy when it is easy. This has been a long journey and we finally made it. Thank you.

Abstract

Shannon's theory of communication created a set of tools for studying complex systems in an abstract and powerful way, providing the core foundations for the field of information theory. This thesis uses these ideas to provide a framework for studying the transverse degree of freedom of an optical field, appropriate for both classical and quantum states of light. This degree of freedom is in principle an unbounded space, providing a complex resource for encoding a large amount of information. This work focuses on studying the physical limits to the information of this space, both in terms of fundamental theoretical limitations as well as practical limitations due to experimental implementation and error.

This thesis will pay particular interest to the design and implementation of a quantum key distribution system encoded using a particular set of transverse modes for encoding known as orbital angular momentum states, which represent normal modes of a typical free-space optical system. This specific technological implementation provides a motivation that acts to unify many of the themes in this work including quantum state preparation, state detection or discrimination, and state evolution

or propagation. Additionally, such a setup gives a specific physical meaning to the abstract tools we will be utilizing as the information that we will be quantifying can be thought of as a measure of the possible complexity or information content of a single photon.

Chapter 1 provides a brief introduction to information theory and the basic concepts and tools that are used throughout this work, as well as a basic introduction to quantum key distribution. Chapter 2 theoretically explores the fundamental limits of the information capacity of a channel due to diffraction, as well as computes the communication modes of a channel using a normal mode approach to propagation. Chapter 3 concerns the experimental implementation of a free-space quantum key distribution system including quantum state preparation and detection, as well as demonstration of a working system. Finally, in chapter 4 we consider the effects of a noisy channel on our analysis, especially decoherence due to the presence of atmospheric turbulence.

Contributors and Funding Sources

This work was supervised by a dissertation committee consisting of Professors Robert W. Boyd (advisor), James R. Fienup, and Carlos Stroud of the Institute of Optics (Edmund A. Hajim School of Engineering and Applied Sciences), as well as by Professor John Howell of the Department of Physics (School of Arts and Sciences). Prof. Boyd also holds an appointment at the University of Ottawa, Ottawa, Canada.

Chapter 1 contains no original research and simply provides necessary background material used for this thesis. Chapter 2 consists of review information with the relevant citations contained within the text, as well as original material and numerical analysis that I have done for the purpose of this thesis. Many of the general ideas discussed are known and properly cited, however their exact use and the results given within the context of the information theoretical framework developed in this thesis are new.

Chapter 3 consists of work done both in our group, as well as work done in collaboration with the group of Professor Miles Padgett from the University of Glasgow. Section 3.1 contains work that comes from two separate papers [1, 2]. Reference [1] describes a method of rapidly generating spatial modes of light and was a project that

was led by Mohammad Mirhosseini and involved the efforts of Omar S. Magaña-Loaiza, Changchen Chen, Mehul Malik, Prof. Boyd and myself. Reference [2] describes a procedure that I developed to generate any arbitrary spatially partially coherent beam and involved Mohammad Mirhosseini, Omar S. Magaña-Loaiza, and Prof. Boyd. Section 3.2 describes an optical orbital angular momentum mode sorting device developed by our collaborators in the Padgett group which was lent to us and used in a number of our experiments. Section 3.3 describes the implementation of a quantum key distribution system as described in [3]. This work was led by Mohammad Mirhosseini and involved the efforts of Omar S. Magaña-Loaiza, Malcolm N. O’Sullivan, Mehul Malik, Prof. Daniel J. Gauthier of Duke University, Robert W. Boyd, and myself.

Chapter 4 involved studying the effects of atmospheric turbulence on spatial modes within the context of communication and is based on five papers [4–8]. I was the main researcher in charge of this project which involved both theoretical and experimental studies. This effort involved Mohammad Mirhosseini and Mehul Malik who were involved in many of the projects and authored Ref. [7] and [6] respectively. In addition experimental support was also provided by Malcolm N. O’Sullivan, Jonathan Leach, Omar S. Magaña-Loaiza, Michael Yanakas, and Laura Maher from the the Boyd group, as well as Martin P. J. Lavery, David J. Robertson, and Prof. Padgett who were collaborators from the Padgett group in Glasgow. Professor Stephen M. Barnett from the University of Strathclyde was involved with the theoretical study in Ref. [4]. Finally, Nicholas K. Steinhoff and Glenn A. Tyler from the Optical Sciences Company

provided the design for the system and some of the numerical simulations for the work done in [8].

My graduate study was supported by Defense Advanced Research Projects Agency's information in a photon project (DARPA InPho).

Table of Contents

Biographical Sketch	iii
List of Graduate Publications	iv
Acknowledgments	vi
Abstract	ix
Contributors and Funding Sources	xi
List of Tables	xvii
List of Figures	xviii
1 Introduction	1
1.1 Shannon Information Theory	2
1.2 Quantum Cryptography	10
1.2.1 Communication with quantum states	11

1.2.2	Quantum key distribution	14
2	Theory of spatial mode communication	18
2.1	Diffraction limited communication	19
2.2	Communication modes	20
2.3	Channel capacity with communication mode encoding	22
2.4	Communication modes of a free-space channel	26
2.5	One dimensional apertures (square geometry)	28
2.5.1	Gaussian apodized apertures	30
2.5.2	Hard rectangular apertures	41
2.6	Cylindrical apertures	49
2.6.1	Gaussian apodized apertures	53
2.6.2	Hard circular apertures	58
2.7	Orbital angular momentum of light	65
2.7.1	Rotational eigenmodes	66
2.7.2	Angular momentum of an optical field	68
3	Implementing spatial mode communication	73
3.1	Spatial mode generation	74
3.1.1	Phase only spatial light modulation	78
3.1.2	Binary spatial light modulation	82

3.1.3	Rapid generation of spatial modes	86
3.1.4	Generation of modes with arbitrary spatial coherence	90
3.2	Spatial mode detection and discrimination	100
3.2.1	Projection measurements of spatial modes	101
3.2.2	Mode sorting of spatial modes	102
3.3	OAM QKD	107
4	Communication with a noisy channel	114
4.1	Atmospheric turbulence	114
4.2	Thin-phase turbulence	118
4.2.1	OAM encoding with thin-phase turbulence	120
4.2.2	Plane-wave encoding with thin-phase turbulence	128
4.3	Thick turbulence	132
4.3.1	Simulating thick turbulence	133
4.3.2	OAM encoding with thick-phase turbulence	140
5	Conclusions and Future Work	145
	References	149

List of Tables

1.1	Encoding in the BB84 scheme	15
1.2	Intercept-resend errors in the BB84 scheme	16

List of Figures

1.1	Schematic of Shannon’s general communication system	3
1.2	Mutual Information	8
2.1	Communication with diffraction limited spots.	20
2.2	Hermite-Gaussian functions	33
2.3	Hermite-Gaussian 2D wavefunctions	35
2.4	Single photon channel capacity using Hermite-Gaussian communication modes	38
2.5	Configuration space for the Hermite-Gaussian communication modes	39
2.6	Classical channel capacity using Hermite-Gaussian communication modes	40
2.7	Transmission efficiencies of the prolate spheroidal communication modes	44
2.8	Abbe’s model of diffraction	45
2.9	Channel capacity using prolate spheroidal communication modes . . .	47
2.10	Prolate spheroidal wavefunctions	48

2.11	Laguerre-Gaussian wavefunctions	57
2.12	Circular prolate spheroidal wavefunctions	62
2.13	Configuration space for the circular prolate spheroidal communication modes	63
2.14	Transmission efficiencies of the circular prolate spheroidal communication modes	64
2.15	Orbital angular momentum states	66
3.1	Detour phase of a shifted diffraction grating	76
3.2	Spatial mode generation setup	77
3.3	Phase only diffraction grating	79
3.4	Spatial light modulation using phase only holograms	82
3.5	Binary diffraction grating	83
3.6	Spatial light modulation using binary holograms	85
3.7	Setup for rapidly generating spatial modes	87
3.8	Images and interferograms of rapidly generated spatial modes	88
3.9	Setup for temporally resolving rapidly generated spatial modes	89
3.10	Time trace of the power in a set of rapidly switched spatial modes	89
3.11	Interference of coherent plane waves	94
3.12	Interference of plane waves with spatially varying coherence	98

3.13	Fringe visibility plot of partially coherent generated field	99
3.14	Setup for the projection measurement of spatial modes	101
3.15	Scaling inefficiency using traditional projection measurements	103
3.16	Ideal sorting of optical modes	104
3.17	Image of an optical log-polar transformation device used for mode sorting	105
3.18	Setup for a free-space, spatially encoded quantum key distribution system	108
3.19	Mutually unbiased bases of the spatial modes used for a spatially encoded QKD system	109
3.20	Measured conditional probabilities of detection in our QKD system .	111
3.21	Error-bounds for unconditional security	112
4.1	Thin phase turbulence model	120
4.2	Experimental setup for simulating a channel with thin-phase turbulence	123
4.3	Measurement of OAM spectrum by spatial binning	124
4.4	OAM scattering due to thin-phase turbulence	125
4.5	OAM input mode invariance of thin-phase turbulence	126
4.6	Decrease in channel capacity of an OAM channel due to turbulence .	127
4.7	Setup for simulating the effects of thin-phase turbulence on plane-wave encoding	130

4.8	Plane-wave mode scattering due to thin-phase turbulence	131
4.9	Decrease in channel capacity due to turbulence using plane-wave encoding	132
4.10	Procedure to find paramters of two phase screen that emulate thick turbulence	136
4.11	Comparison of Strehl ratio statistics of a thick turbulent path and its equivalent two-screen path	137
4.12	Fresnel propagation	139
4.13	Experimental setup for simulating a one kilometer channel with contin- uous turbulence	141
4.14	Crosstalk of OAM communication in a one kilometer channel due to turbulence	142
4.15	Decrease in channel capacity of a one kilometer OAM channel due to turbulence	144

Chapter 1

Introduction

As conscious living beings we all have our own subjective experiences that we live with. One of the amazing features of the human race is the ability to abstract these feelings and experiences and represent these thoughts and ideas. The appearance of language within our species has sharpened and extended this ability tremendously, as well as has given us the ability to transmit meaning to others. This ability to communicate with other people is one of the fundamental elements of what makes us human.

The tools we use to transmit information have grown and evolved through history enabling ever more complex communication. The creation of spoken language encoded ideas or meanings into distinct sounds. The invention of writing put the information into a form that gave the ideas a permanence that allowed ideas to spread further and be remembered longer. The modern era gave birth to electronic means of encoding and transmitting information that now allows the flow of ideas to occur virtually instantly and between nearly any two points on the earth.

This chapter will introduce the basics of information theory from the perspective of communication. These tools will provide the basic context for describing the transverse degree of freedom of light within the framework of communication or information. This provides a universal framework for thinking about such topics as spatial mode modulation, optical beam propagation, and measurement theory that will be explored in later chapters. In addition, section 1.2 will give a brief introduction to the field of quantum communication and cryptography which provides a specific technological implementation that integrates many of the topics that will be discussed throughout this thesis and thus provides a motivation for many of the ideas that will be presented.

1.1 Shannon Information Theory

The complexity of modern communication has given rise to a number of fields that try to model and thus better understand this phenomena. One of the major areas that has arisen in this context is the field of information theory. Information theory tries to analyze information qua information, and is seen as having been formally established in the seminal paper by Claude Shannon, “A mathematical theory of communication” [9]. Shannon gave a generalized picture of communication which is shown schematically in Fig. 1.1 and consists of three stages; a sender and receiver (traditionally named Alice and Bob), and a physical medium or channel over which the intended information is transmitted between Alice and Bob.

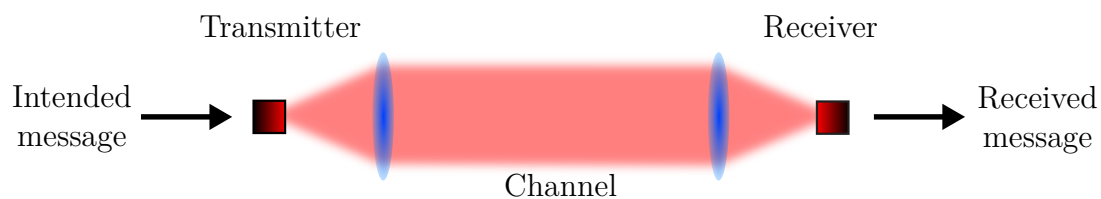


Figure 1.1: Schematic of Shannon's general communication system

Alice must encode the intended information onto some physical medium that can be transmitted to Bob. This stage is the fundamental stage of abstracting or symbolically representing meaning. Language is a natural example of this. In speech a specific idea is represented by a specific sound or grouping of sounds, while in written language the representation of the idea is in the form of visual characters or symbols. In general, ideas are represented in some physical form that can be transmitted and ultimately experienced or sensed by another person. Each physical symbol is chosen from a set of distinct possible symbols with pre-agreed upon meanings.

So in the general communication scheme of Fig. 1.1, Alice translates the intended message into a series of abstract symbols. Each symbol is encoded onto the state of the physical medium in one of a number of different possible configurations. The list of possible configurations or symbols $x \in \mathbb{X}$ is called the alphabet, in analogy with written communication. The information $I(X)$ of a random symbol X with N equally likely possible values $x \in \mathbb{X}$ is defined to be

$$I(X) = \log_b(N). \quad (1.1)$$

The logarithmic measure of information is chosen because the number of distinct possible messages generally grows exponentially with resources. For example if a message contains n independent random symbols X , each chosen from an alphabet of size N , then the total number of possible combinations of sequences is N^n , and the amount of information contained in this sequence is

$$I(X^n) = \log_b(N^n) = n \log_b(N) = nI(X). \quad (1.2)$$

It should be noted that information as defined by Eq. (1.1) is only defined to within a constant, which is equivalent to the freedom to choose the base b of the logarithm which defines the units of information. If the natural logarithm is chosen then information is given by nats, and if base two is chosen then the information is in bits.

Although Eq. (1.1) specifies the information for a message with equally likely outcomes, this is not always the case. A more general method of quantifying the information of an unknown process or message is to consider a set of possibilities $x \in \mathbb{X}$ that are not equally likely. In this case each outcome will have an associated probability

$$p(x) \equiv p(X = x), \quad (1.3)$$

that represents the relative likelihood that the event X will be represented by the particular possibility x . The more probable an event x is to occur, the less weight or information is conveyed when x occurs. For instance if $p(x) = 1$, then there is no

difference in knowledge before and after the event occurs and thus $I(x) = 0$. Whereas, if $p(x) \approx 0$, then if x occurs this is very surprising, i.e. a lot of information is gained and thus $I(x)$ should be large. The information gained from measuring $x \in \mathbb{X}$ is therefore given by

$$I(x) \equiv I(X = x) = \log\left(\frac{1}{p(x)}\right) = -\log(p(x)). \quad (1.4)$$

The average information per event X is given by

$$H(X) = E[I(x)] = \sum_x p(x)I(x) = -\sum_x p(x) \log(p(x)), \quad (1.5)$$

where E is the expected value operator. $H(X)$ is known as the Shannon information or entropy by analogy between Eq. (1.5) and the thermodynamic formula for entropy S given by

$$S = k_B H_B = -k_B \sum_x p(x) \log(p(x)), \quad (1.6)$$

where k_B is Boltzman's constant, $p(x)$ represents probabilities of a system existing in microstate x , and H_B is the function used in Boltzman's H-theorem. Note that if all outcomes of an event X are equally likely, i.e. if the probabilities are given by

$$p(x) = 1/N \quad \forall x \in \mathbb{X}, \quad (1.7)$$

then the information is

$$I(x) = -\log(1/N) = \log(N), \quad (1.8)$$

and we recover the expression given by Eq. (1.1).

The Shannon information given by Eq. (1.5) can describe equally well the amount of information that Alice can encode in a message as well as the amount of information that Bob learns upon receiving that message. If we say that the channel transmits from $\mathbb{A} \rightarrow \mathbb{B}$, i.e. Alice sends some symbol $A = a \in \mathbb{A}$ and Bob measures some possible state $B = b \in \mathbb{B}$, then the expectation value of the amount of information that Bob obtains upon measurement of his received symbol is given by $H(B)$, where the probabilities $p(x)$ in Eq. (1.5) are replaced by the probability of Bob detecting mode $b \in \mathbb{B}$ given by $p(b)$. If the channel is ideal, than Bob receives the exact encoded message Alice transmitted and thus Bob has the same amount of information as was sent and $H(B) = H(A)$. However for a general channel there will be errors and some of the information necessary to describe Bob's detection will be caused by these errors. Assuming that Alice sent a , the amount of the information that Bob gains from his measurement $B = b$ that are due to these errors alone can be quantified by considering the entropy of B conditioned on $A = a$ given by

$$H(B|A = a) = -\sum_b p(b|a) \log(p(b|a)). \quad (1.9)$$

The average or expected error is given by the conditional entropy $H(B|A)$ given by

$$H(B|A) = E[H(B|A = a)] = - \sum_{a,b} p(a)p(b|a) \log(p(b|a)). \quad (1.10)$$

The average amount of information that Alice transmits to Bob in a noisy or imperfect channel is thus given by the mutual information which is simply the information Bob measures minus the information that is not due to Alice quantified by the conditional entropy, i.e.

$$I(A; B) \equiv H(B) - H(B|A). \quad (1.11)$$

The relationships between the Shannon entropies, the conditional entropy, and the mutual information is shown schematically in Fig. 1.2.

Generally one does not know the probabilities $p(b)$ a priori, as this depends both on the encoding scheme as well as the channel itself. Therefore it is often convenient to use the identity

$$p(b) = \sum_a p(b|a)p(a), \quad (1.12)$$

to make the dependence on $p(a)$ and $p(b|a)$ explicit. This way information due to the encoding and to the channel are separated as $p(a)$ is based on the encoding used and the conditional probabilities $p(b|a)$ are a property of the channel which can be

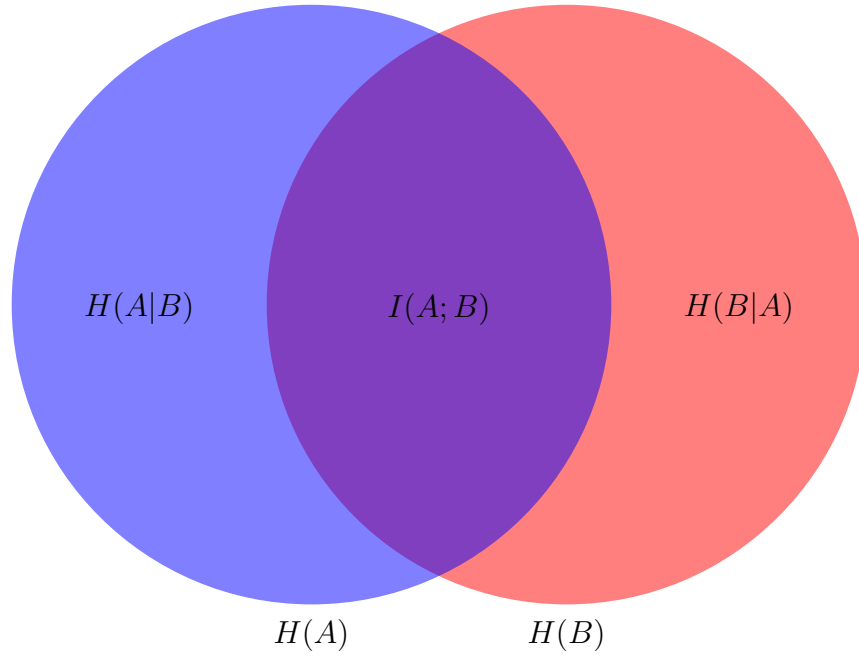


Figure 1.2: The marginal entropies representing the information that Alice encodes $H(A)$ and Bob measures $H(B)$ is represented by the blue and red circles respectively. The areas that do not overlap are the conditional entropies and the overlapping region represents the mutual information $I(A; B)$.

experimentally tested. Using this identity Eq. 1.11 can be written as

$$\begin{aligned}
 I(A; B) &= - \sum_b p(b) \log(p(b)) + \sum_{a,b} p(b|a)p(a) \log(p(b|a)) \\
 &= - \sum_{a,b} p(b|a)p(a) \log \left(\sum_{a'} p(b|a')p(a') \right) + \sum_{a,b} p(b|a)p(a) \log(p(b|a)) \quad (1.13) \\
 &= \sum_{a,b} p(b|a)p(a) \log \left(\frac{p(b|a)}{\sum_{a'} p(b|a')p(a')} \right),
 \end{aligned}$$

where the last line is given in terms of quantities that are directly available to the experimenter.

The final stage of communication shown in Fig. 1.1 is decoding of the received message by Bob. However, a noisy channel (i.e. a channel with a non-zero value of $H(B|A)$) means that Bob's message will contain errors, and the average amount of information contained in the received message that correlates with the message Alice sent is $I(A; B)$. Alternatively, if Alice and Bob know in advance that the channel is imperfect, then Alice can encode redundant information in the sent message in a predetermined way which Bob can then use to correct for possible errors in his received message. In what is now known as Shannon's noisy-channel coding theorem [10], Shannon showed that in principle an intended message could be recovered using error correction with negligible probability of error. However, this is true only if the average amount of information that is extracted per symbol is less than the channel capacity C given by mutual information maximized over all input weightings $p(a)$, i.e.

$$C = \sup_{p(a)} I(A; B). \quad (1.14)$$

The maximum information rate transmitted into the channel is simply the symbol rate times $I(A; B)$. In order to maximize communication there are three primary methods available. The first method is to maximize the rate at which symbols are generated and sent. The second method is to maximize the information of each symbol, represented by either $H(A)$ or $H(B)$, which is done primarily by using the largest alphabet possible. Finally one wants to find a means of communication that minimizes

the errors of transmission $H(B|A)$, which may come from the channel or imperfect transmitters or receivers.

Much of this work focuses on communication with optical fields that exploit the large configuration space afforded by the transverse spatial degree of freedom of the field to maximize the symbol alphabet and the limitations of such a scheme.

1.2 Quantum Cryptography

Maximization of the information capacity of a channel is not the only parameter that is generally cared about in communication. If the channel is a public channel, or there is a fear of an eavesdropper listening in on the channel, then it may be desirable to find a way for Alice and Bob to communicate in a secure fashion. One standard method used is to encrypt the message with a cryptographic key. This is an algorithm that takes the message plus a random key to generate a new message that (ideally) contains only random information if one does not know how to decrypt the message (such as by knowing the key). Standard methods generally rely on computational complexity for encryption, but an exciting alternative is quantum cryptographic methods such as quantum key distribution (QKD), which relies on using quantum resources to securely distribute a random key for use in encrypting an intended message [11].

1.2.1 Communication with quantum states

Section 1.1 gave an introduction to some of the theoretical foundations of information and communication. Expanding this theory to include tools that require quantum resources leads to the fields of quantum communication and quantum information. One of the fundamental features of a quantum system that becomes one of the basic tools in quantum information is the phenomena of superposition. Consider a system that can be measured in one of two mutually exclusive states which we can write in the standard Dirac notation as $|0\rangle$ or $|1\rangle$. If this were simply a classical system then we would have each symbol or bit $x = 0$ or 1 encoded using the states $|0\rangle$ or $|1\rangle$. However as a quantum system the most general possible state $|\psi\rangle$ of this system is represented as the (normalized) linear combination

$$|\psi\rangle = a|0\rangle + b|1\rangle, \quad (1.15)$$

where $a, b \in \mathbb{C}$, and

$$|a|^2 + |b|^2 = 1. \quad (1.16)$$

The state in Eq. (1.15) is a general representation of what is called a quantum bit or qbit with the states $|0\rangle$ and $|1\rangle$ acting as a basis for this representation.

If Alice prepares a qbit in the state given by Eq. (1.15) and Bob checks to see if the state was in the $|0\rangle$ or $|1\rangle$ state, he will get a definite answer of one or the other

with probabilities given by

$$p(x = 0) = |a|^2, \text{ and } p(x = 1) = |b|^2. \quad (1.17)$$

Thus at most Bob only gets one bit of information per measurement. This type of measurement is known as projection measurement. In general a projection measurement is described by a Hermitian operator \hat{M} which can be expanded in terms of its spectral decomposition

$$\hat{M} = \sum_n^N \lambda_n \hat{P}_n = \sum_n^N \lambda_n |\phi_n\rangle\langle\phi_n|, \quad (1.18)$$

where $\hat{P}_n = |\phi_n\rangle\langle\phi_n|$ are projectors of the N orthogonal eigenstates $|\phi_n\rangle$ spanning the N -dimensional space, and λ_n are corresponding eigenvalues of \hat{M} . A projection style measurement of \hat{M} will result in one of the N outcomes λ_n with the probability of measuring the n th state given by

$$p_n = \langle\psi|\hat{P}_n|\psi\rangle = |\langle\psi|\phi_n\rangle|^2. \quad (1.19)$$

Therefore the case of Bob testing if the state is $|0\rangle$ or $|1\rangle$ corresponds to projectors

$$\hat{P}_0 = |0\rangle\langle 0| \text{ and } \hat{P}_1 = |1\rangle\langle 1|. \quad (1.20)$$

A special feature of measurements of quantum systems is the ability to choose a different measurement scheme \hat{M}' for the same system with projectors over states $|\phi'_n\rangle$ that are superpositions of the eigenstates $|\phi_n\rangle$ of \hat{M} . \hat{M} and \hat{M}' are said to represent incompatible observables and will introduce uncertainty into Bob's measurement, i.e. the entropy of Bob's measurement conditioned on Alice's preparation will not be zero. For instance if Alice prepares the system in the state $|0\rangle$ and Bob measures the state using the projectors given by Eq. (1.20), he will decide the symbol was zero with 100% certainty. However if instead Bob makes a measurement by projecting over the states

$$|\phi_{\pm}\rangle = \frac{1}{2} (|0\rangle \pm |1\rangle), \quad (1.21)$$

he will find the state in either $|\phi_+\rangle$ or $|\phi_-\rangle$ each with 50% probability. Therefore, even in the absence of noise the conditional entropy is one bit and the mutual information between Alice and Bob is exactly zero. After the measurement either the particle itself will have been destroyed, such as when a photon is detected, or the quantum state will have been collapsed into the detected state and any subsequent measurement will yield the same result and so there is nothing more Bob can do to recover the lost information.

1.2.2 Quantum key distribution

One of the first papers on QKD was given by Bennett and Brassard in 1984 and is aptly known as the BB84 protocol [12]. In a BB84 scheme Alice sends a random key to Bob using at least two distinct sets of modes from incompatible observables \hat{M} and \hat{M}' for encoding. For each symbol that is transmitted, Alice randomly chooses which alphabet or basis of states to choose her symbol from, and Bob randomly chooses which basis to measure in. An important constraint on these modes is the requirement that both sets of modes span the same Hilbert (sub)space and each basis of states must represent a mutually unbiased basis (MUB) with respect to any other basis used in the scheme. This means that if a state in one basis is measured by projecting in another, then the probability of detection is equal among all states and thus the mutual information between the prepared state and measured state is identically zero. This can alternately be written as

$$|\langle a | b \rangle|^2 = 1/N, \quad (1.22)$$

where $|a\rangle$ and $|b\rangle$ are any two states from different MUBs and N is the dimensionality of the Hilbert space. Security comes from the fact that any eavesdropper (conventionally referred to as Eve) who may have access to the transmitted state will be ignorant of which basis each state was prepared and as a result, will introduce errors into the

stream of symbols due to this ignorance and the inherent quantum uncertainty in measuring such general unknown states.

	<i>H/V</i> basis		<i>D/A</i> basis	
Symbol	0	1	0	1
State	$ H\rangle$	$ V\rangle$	$ D\rangle$	$ A\rangle$

Table 1.1: Encoding of binary symbols in the original BB84 scheme of Ref. [12] demonstrating the use of two incompatible polarization bases.

The original example in Ref. [12] used the polarization of photons to encode the key. Each symbol consisted of a single linearly polarized photon whose orientation determines whether the state is a binary zero or one. In the first basis the photon polarization is either horizontally or vertically oriented i.e.

$$|0\rangle_1 = |H\rangle \text{ and } |1\rangle_1 = |V\rangle. \quad (1.23)$$

A second basis was chosen such that the polarization is linear and orientated along the diagonal and anti-diagonal directions, which can be represented in terms of the original basis as

$$|0\rangle_2 = |D\rangle = \frac{1}{\sqrt{2}}(|H\rangle + |V\rangle) \text{ and } |1\rangle_2 = |A\rangle = \frac{1}{\sqrt{2}}(|H\rangle - |V\rangle) \quad (1.24)$$

respectively. Alice randomly sends in either the *H/V* or *D/A* basis and Bob chooses which basis to make a measurement in. After sending a sufficiently long message Alice

and Bob will sift the key by announcing which basis was used for each symbol and keep only the part of the message in which both choose the same basis.

Alice and Bob then announce part of their key to test for errors to check for the presence of Eve, as her presence will necessarily introduce errors. For instance if Eve measures and then resends in a randomly chosen basis, she will measure in the wrong basis half of the time and thus Bob, measuring in the correct basis, will get an incorrect bit half of these times. For instance if Alice prepares the symbol $x = 0$ in the H/V basis she will send state $|H\rangle$. There is a 50% chance Eve will choose the correct H/V basis in which case she will measure and send the same state to Bob introducing no errors. However, if Eve chooses to measure in the D/A basis then she will measure and resend either $|D\rangle$ or $|A\rangle$ to Bob. In both of these cases a measurement by Bob in the correct H/V measurement will be completely random with a measurement of $|H\rangle$ and $|V\rangle$ both occurring with a probability of 50%. A list of possible combinations is given in Table 1.2. If Eve is using an intercept-resend strategy she will induce an error rate of at least 25%. Therefore if Alice and Bob measure an error rate of less than 25%, then they can be certain there was no eavesdropper making such an attack.

Alice/Bob's Basis	Eve's Basis	Frequency	Error	Contribution to total error
H/V	H/V	1/4	0%	0%
H/V	D/A	1/4	50%	25%
D/A	H/V	1/4	50%	25%
D/A	D/A	1/4	0%	0%

Table 1.2: Introduction of errors into the sifted key in a BB84 QKD scheme due to an eavesdropper (Eve) intercepting and measuring each symbol in a random basis and then resending the measured symbol to Bob.

The error rate caused by Eve in an intercept-resend strategy can be generalized to using more than two MUBs and using a state space dimensionality greater than two. If the number of MUBs used is N , then Eve will choose the wrong basis with probability $(N - 1)/N$. If the dimensionality of the Hilbert space is d , and Eve measures in the incorrect basis, Bob will get an error with probability $(d - 1)/d$. Therefore the intercept-resend strategy will in general create an error with probability $(N - 1)(d - 1)/Nd$. Thus the security of the protocol can be improved by increasing the state space or the number of MUBs and it can be shown that this holds true even for more sophisticated eavesdropping strategies [13, 14]. Although security is improved by increasing either N or d , increasing the number of MUBs has the disadvantage of not only increasing the probability that Eve will choose the wrong basis, but also that Bob will choose incorrectly as well, thus decreasing the sifted key rate by a factor of N . For this reason our work focuses entirely on an increase in the number of symbols used for encoding, rather than on finding a large number of MUBs.

Chapter 2

Theory of spatial mode communication

As was demonstrated in chapter 1, using large alphabets or state spaces to encode information in a communication channel can allow for significant increases to channel communication rates as well as improvements in security in QKD. A particularly attractive physical resource that allows for many distinct states is the transverse or spatial degree of freedom of light, as the number of modes needed to describe an arbitrary field in a plane are unbounded. Optical means of communication are a natural and common means of communication, although exploiting spatial modes of light have only recently begun to be explored in this context. This interest includes both increasing transmission rates in classical channels [15] as well as for use in QKD systems [3, 14, 16, 17]

2.1 Diffraction limited communication

As previously seen, the benefit of using a resource for communication depends largely on the number of distinct possible states N for that resource. Although the spatial degree of freedom of an optical field appears unbounded, in practice N will always be limited. The primary physical mechanism limiting N will be diffraction and loss due to the sender and receiver having finite apertures. N can be estimated by imagining Alice communicates to Bob by focusing a beam to a spot in Bob's receiver as shown in Fig. 2.1. Two spots will be barely resolvable if they are separated by the Rayleigh criterion given by

$$\delta x \propto \lambda z / D_T, \quad (2.1)$$

where λ is the wavelength, z is the separation between apertures and D_T is the transmitter diameter. The area of each spot therefore takes up roughly

$$(\delta x)^2 \propto (\lambda z)^2 / A_T, \quad (2.2)$$

where A_T is the area of the transmitting aperture.

The total number of spots distinguishable in the receiver aperture is therefore equal to the number of spots that fit within an area of the receiver A_R which gives

$$N \approx A_R / (\delta x)^2 \approx \frac{A_R A_T}{(\lambda z)^2} = D_F, \quad (2.3)$$

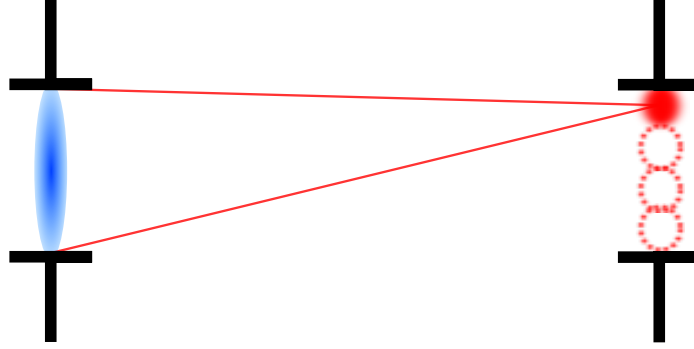


Figure 2.1: Communication scheme where various symbols are encoded by the location of distinct spots focused within the receiver's aperture. The number of distinct spots is given by the Fresnel number product D_F of the sender and receiver.

where D_F is known as the Fresnel number product of the sender and receiver. Therefore the amount of information that can be transmitted by a diffraction limited communication channel is expected to be approximately

$$I(A; B) \approx \log(D_F). \quad (2.4)$$

2.2 Communication modes

The more rigorous method of counting the number of available modes is to consider the Green's function operator \hat{G} that maps functions in Alice's aperture \mathcal{A} to Bob's aperture \mathcal{B} , i.e.

$$\hat{G}: \mathcal{A} \rightarrow \mathcal{B}. \quad (2.5)$$

The Green's function operator \hat{G} includes loss from both apertures as well as the propagation in the channel, and is therefore generally not a unitary or information

preserving map. For all physically realistic situations \hat{G} will be represented as a Hilbert-Schmidt operator, meaning an operator that is a linear operator with a norm of finite measure and therefore by Mercer's theorem [18] there will be a normal mode decomposition of \hat{G} . Thus we can write the propagator as

$$\hat{G} = \sum_n g_n |b_n\rangle\langle a_n|, \quad (2.6)$$

where $|a_n\rangle \in \mathcal{A}$ and $|b_n\rangle \in \mathcal{B}$ are orthonormal sets of modes within their respective apertures. Equation (2.6) can be rewritten as the set of eigenequations

$$\hat{G}^\dagger \hat{G} |a_n\rangle = |g_n|^2 |a_n\rangle \quad \hat{G} \hat{G}^\dagger |b_n\rangle = |g_n|^2 |b_n\rangle. \quad (2.7)$$

The modes in Eqs. (2.6) – (2.7) are known as the communication modes [19], and Eq. (2.6) can be interpreted as a one-to-one map of the set of modes $|a_n\rangle$ onto the set $|b_n\rangle$ with coupling constant g_n (i.e. power efficiency $\eta_n = |g_n|^2$). Such a decomposition discretizes the problem and allows us to apply the discrete tools developed in section 1.1 that allow us to quantify a physical process in terms of information theoretical concepts. In addition, the communication modes abstract the problem of propagation from all further analysis, allowing a full characterization of the problem in terms of a single special set of modes. Therefore a careful examination of the problem of diffraction using this perspective is both desirable and advantageous.

2.3 Channel capacity with communication mode encoding

Since Eqn. (2.6) specifies a one-to-one map of modes, this means we can write the conditional probability of Bob detecting mode $|b_n\rangle$ given that Alice sends mode $|a_m\rangle$ as

$$p(b_n|a_m) = \delta_{m,n}p_s(\eta_n), \quad (2.8)$$

where $p_s(\eta_n)$ is the probability that Bob measures a signal. For communication using single photons (such as in QKD) then η_n is the probability of Bob receiving a photon or not and thus for ideal detection

$$p_s^{\text{QKD}}(\eta_n) = \eta_n. \quad (2.9)$$

For classical communication communication, Bob will still receive a signal, even in the presence of loss. If the original signal was some power P_0 , then Bob will receive a signal with power ηP_0 . If the noise equivalent power (NEP) is significantly less than ηP_0 , then Bob will register the correct symbol with very high probability. Therefore, a simple model for p_s is to treat it as a threshold or step function, i.e.

$$p_s^{\text{classical}}(\eta_n) = \begin{cases} 1 & \text{if } \eta_n > \eta_{\min} \\ 0 & \text{otherwise} \end{cases}. \quad (2.10)$$

The value of η_{\min} must be chosen high enough that errors are not introduced from noise, but low enough that the capacity of the channel isn't artificially restricted. The ideal value will depend on optimising these effects which depend on the exact nature of the noise of the system. This is a major area of study within the fields of signal processing and estimation theory, the details of which is beyond the scope of this thesis.

Using the conditional probability defined in Eq. (2.8), the marginal probability of Bob measuring mode $|b_n\rangle$ therefore takes on the simple form

$$p(b_n) = \sum_m p(b_n|a_m)p(a_m) = \sum_m \delta_{m,n}p_s(\eta_n)p(a_m) = p_s(\eta_n)p(a_n). \quad (2.11)$$

Using these two equations allows us to write the mutual information in a form that only depends on the values of $p(a_n)$ and $p_s(\eta_n)$,

$$\begin{aligned} I(A; B) &= \sum_{m,n} p(a_m)p(b_n|a_m) \log \left(\frac{p(b_n|a_m)}{p(b_n)} \right) \\ &= \sum_{m,n} p(a_m)\delta_{m,n}p_s(\eta_n) \log \left(\frac{\delta_{m,n}p_s(\eta_n)}{p_s(\eta_n)p(a_n)} \right) \\ &= \sum_n p(a_n)p_s(\eta_n) \log \left(\frac{1}{p(a_n)} \right) \\ &= - \sum_n p(a_n)p_s(\eta_n) \log (p(a_n)). \end{aligned} \quad (2.12)$$

An expression for the channel capacity can be found by finding the supremum of Eq. (2.12) subject to the constraint

$$\sum_n p(a_n) = 1. \quad (2.13)$$

Using the method of Lagrange multipliers this requires extremizing the function

$$\begin{aligned} L &= I(A; B) + \lambda \left(\sum_n p(a_n) - 1 \right) \\ &= - \sum_n p(a_n) p_s(\eta_n) \log(p(a_n)) + \lambda \left(\sum_n p(a_n) - 1 \right), \end{aligned} \quad (2.14)$$

where λ is a constant chosen to satisfy the constraint in Eq. (2.13). The function L in Eq. (2.14) will be maximized at points of stationarity with respect to the probabilities $p(a_n)$, i.e.

$$\frac{\partial L}{\partial p(a_n)} = 0 = -p_s(\eta_n) \log(p(a_n)) - p_s(\eta_n) + \lambda. \quad (2.15)$$

Solving this equation for $p(a_n)$ gives

$$p(a_n) = \exp \left(\frac{\lambda}{p_s(\eta_n)} - 1 \right). \quad (2.16)$$

Since this equation yields non-negative values for $p(a_n)$, and the sum of probabilities is equal to one, we can see that Eq. (2.16) gives the correct range of values

$$0 \geq p(a_n) \geq 1 \quad \forall n. \quad (2.17)$$

For the quantum case where we use the signal probability $p_s^{\text{QKD}}(\eta_n) = \eta_n$ from Eq. (2.9) the channel capacity is

$$C^{\text{QKD}} = - \sum_n p^{\text{QKD}}(a_n) \eta_n \log(p^{\text{QKD}}(a_n)) \quad (2.18)$$

with

$$p^{\text{QKD}}(a_n) = \exp\left(\frac{\lambda}{\eta_n} - 1\right). \quad (2.19)$$

For the classical case we assume there are N total states with efficiencies greater than the threshold η_{\min} given by Eq. (2.10), i.e.

$$p_s^{\text{classical}}(\eta_n) = \begin{cases} 1 & \text{if } n \leq N \\ 0 & \text{otherwise} \end{cases}. \quad (2.20)$$

In this case

$$p^{\text{classical}}(a_n) = \begin{cases} \exp(\lambda - 1) & \text{if } n \leq N \\ 0 & \text{otherwise} \end{cases}, \quad (2.21)$$

which solving for the constraint specified in Eq. (2.13) gives

$$p^{\text{classical}}(a_n) = \begin{cases} 1/N & \text{if } n \leq N \\ 0 & \text{otherwise} \end{cases}. \quad (2.22)$$

Therefore by Eq. (2.12) the channel capacity of a classical channel is given as

$$C^{\text{classical}} = \sum_{n=1}^N \frac{1}{N} \log(N) = \log(N). \quad (2.23)$$

2.4 Communication modes of a free-space channel

An important metric that will be shown to correspond roughly to the total number of modes is the Hilbert-Schmidt inner product of \hat{G} defined as

$$\|\hat{G}\|^2 \equiv \text{Tr}(\hat{G}^\dagger \hat{G}) = \sum_n |g_n|^2 = \sum_n \eta_n^2. \quad (2.24)$$

Assuming propagation over a distance z within a free-space optical channel assumed to be within the paraxial regime, then the Green's function can be written as [20]

$$\langle \mathbf{r} | \hat{G} | \mathbf{r}' \rangle \equiv G(\mathbf{r}, \mathbf{r}') = \frac{P_R(\mathbf{r})P_T(\mathbf{r}')}{i\lambda z} \exp\left(ikz + ik|\mathbf{r} - \mathbf{r}'|^2/2z\right), \quad (2.25)$$

where λ is the wavelength, $k = 2\pi/\lambda$ is the wavenumber, and $P_T(\mathbf{r})$ and $P_R(\mathbf{r})$ are the pupil transmission functions for Alice and Bob. For such a propagator

$$\|\hat{G}\|^2 = \iint |G(\mathbf{r}, \mathbf{r}')|^2 d\mathbf{r}' d\mathbf{r} = A_R A_T / (\lambda z)^2 = D_F \quad (2.26)$$

where

$$A = \int |P(\mathbf{r})|^2 d\mathbf{r} \quad (2.27)$$

is the area of the aperture. Therefore by combining the above expressions with Eq. (2.24), we see that the sum of the mode coupling efficiencies equals the Fresnel

number product D_F , i.e.

$$\sum_n |g_n|^2 = D_F. \quad (2.28)$$

In order to gain any more information about the communication modes or their coupling strengths g_n , we need to solve the eigenequations in Eq. (2.7). The spatial representation of these eigenequations is

$$\begin{aligned} \iint \langle \mathbf{r}_T | \hat{G}^\dagger \hat{G} | \mathbf{r}'_T \rangle \Psi_n(\mathbf{r}'_T) d\mathbf{r}'_T &= \iint K(\mathbf{r}_T, \mathbf{r}'_T) \Psi_n(\mathbf{r}'_T) d\mathbf{r}'_T = |g_n|^2 \Psi_n(\mathbf{r}_T) \\ \iint \langle \mathbf{r}_R | \hat{G} \hat{G}^\dagger | \mathbf{r}'_R \rangle \Phi_n(\mathbf{r}'_R) d\mathbf{r}'_R &= \iint K'(\mathbf{r}_R, \mathbf{r}'_R) \Phi_n(\mathbf{r}'_R) d\mathbf{r}'_R = |g_n|^2 \Phi_n(\mathbf{r}_R), \end{aligned} \quad (2.29)$$

where

$$\Psi_n(\mathbf{r}) \equiv \langle \mathbf{r} | a_n \rangle \quad \text{and} \quad \Phi_n(\mathbf{r}) \equiv \langle \mathbf{r} | b_n \rangle \quad (2.30)$$

are the spatial representations of the communication modes in Alice and Bob's apertures respectively. The integral kernels K and K' of Eq. (2.29) can be found using Eq. (2.25). This is given by

$$\begin{aligned} K(\mathbf{r}_T, \mathbf{r}'_T) &= \langle \mathbf{r}_T | \hat{G}^\dagger \hat{G} | \mathbf{r}'_T \rangle \\ &= \iint \langle \mathbf{r}_T | \hat{G}^\dagger | \mathbf{r}_R \rangle \langle \mathbf{r}_R | \hat{G} | \mathbf{r}'_T \rangle d\mathbf{r}_R \\ &= \frac{P_T^*(\mathbf{r}_T) P_T(\mathbf{r}'_T)}{(\lambda z)^2} \iint |P_R(\mathbf{r}_R)|^2 e^{-i\frac{k}{2z}|\mathbf{r}_T - \mathbf{r}_R|^2} e^{i\frac{k}{2z}|\mathbf{r}'_T - \mathbf{r}_R|^2} d\mathbf{r}_R, \end{aligned} \quad (2.31)$$

and similarly

$$K'(\mathbf{r}_R, \mathbf{r}'_R) = \frac{P_R(\mathbf{r}_R) P_R^*(\mathbf{r}'_R)}{(\lambda z)^2} \iint |P_T(\mathbf{r}_T)|^2 e^{i\frac{k}{2z}|\mathbf{r}_R - \mathbf{r}_T|^2} e^{-i\frac{k}{2z}|\mathbf{r}'_R - \mathbf{r}_T|^2} d\mathbf{r}_T. \quad (2.32)$$

Note that if the channel is symmetric, i.e. if

$$P_T(\mathbf{r}) = P_R(\mathbf{r}), \quad (2.33)$$

then $K' = K^*$ and thus the eigenequations in Eq. (2.29) are complex conjugates of each other. In this situation the eigenstates are simply related as

$$\Phi_n(\mathbf{r}) = \Psi_n^*(\mathbf{r}). \quad (2.34)$$

The solutions to Eq. (2.29) depend on the form of the pupil functions P_T and P_R . Two typical cases are given in sec. 2.5 – 2.6. Section 2.5 looks at the case of rectangular apertures, which gives solutions in separable Cartesian coordinates. Section 2.6 gives solutions for the more typical round apertures which leads to a natural decomposition in cylindrical coordinates.

2.5 One dimensional apertures (square geometry)

The first and simplest geometry we consider is one in which the pupil functions are separable in Cartesian coordinates, i.e.

$$P_R(x, y) = P_{R,x}(x) \times P_{R,y}(y) \quad \text{and} \quad P_T(x, y) = P_{T,x}(x) \times P_{T,y}(y). \quad (2.35)$$

In this case Eq. (2.31) can be written as

$$\begin{aligned}
K(\mathbf{r}_T, \mathbf{r}'_T) &= \frac{P_T^*(\mathbf{r}_T)P_T(\mathbf{r}'_T)}{(\lambda z)^2} \iint |P_R(\mathbf{r}_R)|^2 e^{-i\frac{k}{2z}|\mathbf{r}_T-\mathbf{r}_R|^2} e^{i\frac{k}{2z}|\mathbf{r}'_T-\mathbf{r}_R|^2} d\mathbf{r}_R \\
&= \frac{P_{T,x}^*(x_T)P_{T,x}(x'_T)}{\lambda z} \int |P_{R,x}(x_R)|^2 e^{-i\frac{k}{2z}|x_T-x_R|^2} e^{i\frac{k}{2z}|x'_T-x_R|^2} dx_R \\
&\quad \times \frac{P_{T,y}^*(y_T)P_{T,y}(y'_T)}{\lambda z} \int |P_{R,y}(y_R)|^2 e^{-i\frac{k}{2z}|y_T-y_R|^2} e^{i\frac{k}{2z}|y'_T-y_R|^2} dy_R \\
&= K_{1D}(x_T, x'_T) \times K_{1D}(y_T, y'_T).
\end{aligned} \tag{2.36}$$

Therefore we can write the eigenequation for $\Psi(x, y)$ from Eq. (2.29) as

$$\begin{aligned}
&\int K_{1D}(x_T, x'_T)\psi_{m,x}(x'_T) dx'_T \times \int K_{1D}(y_T, y'_T)\psi_{n,y}(y'_T) dy'_T \\
&= \eta_{m,x}\psi_{m,x}(x_T) \times \eta_{n,y}\psi_{n,y}(y_T),
\end{aligned} \tag{2.37}$$

where $\Psi_{m,n}(x, y) = \psi_{m,x}(x) \times \psi_{n,y}(y)$ and $\eta_m = \eta_{m,x} \times \eta_{m,y}$. This means that for a square geometry we only need to solve the one dimensional eigenequations

$$\begin{aligned}
\int K_{1D}(x, x')\psi_{m,x}(x') dx' &= \eta_{m,x}\psi_{m,x}(x) \\
\int K_{1D}(y, y')\psi_{n,y}(y') dy' &= \eta_{n,y}\psi_{n,y}(y).
\end{aligned} \tag{2.38}$$

It is convenient to define the one dimensional version of the norm, $\|\hat{G}\|^2$, given in Eq. (2.26). This can be written as

$$\|\hat{G}_{1D}\|^2 = \iint |G_{1D}(x, x')|^2 dx dx' \equiv \int |K_{1D}(x, x)|^2 dx = \frac{L_R L_T}{\lambda z} = D_{F,1D}, \tag{2.39}$$

where $D_{F,1D}$ is the 1D Fresnel number product and

$$L = \int |P(x)|^2 dx \quad (2.40)$$

is the generalized pupil length, which acts as the 1D analog to the area defined in Eq. (2.27).

2.5.1 Gaussian apodized apertures

In order to solve for the eigenequations in Eq. (2.38), we need to know K_{1D} and thus have a specific form for the apertures. We first consider apertures that are Gaussian apodized as these results are known to have analytic solutions [21]. Such apertures will be specified by the (one dimensional) pupil functions

$$P_T(x) = \exp\left(\frac{-x^2}{2\sigma_T^2}\right) \text{ and } P_R(x) = \exp\left(\frac{-x^2}{2\sigma_R^2}\right), \quad (2.41)$$

which have characteristic lengths based on Eq. (2.40) of

$$L_{R/T} = \int |P_{R/T}(x)|^2 dx = \int e^{-x^2/\sigma_{R/T}^2} dx = \sigma_{R/T}\sqrt{\pi}. \quad (2.42)$$

This system has a (one dimensional) Fresnel number product of

$$D_F = \frac{L_R L_T}{\lambda z} = \frac{\pi \sigma_R \sigma_T}{\lambda z} = \frac{k \sigma_R \sigma_T}{2z}. \quad (2.43)$$

Now we can compute the kernel K_{1D} by plugging the pupil expressions into Eq. (2.36). This gives

$$\begin{aligned}
K_{1D}(x, x') &= \frac{P_{T,x}^*(x)P_{T,x}(x')}{\lambda z} \int |P_{R,x}(x_R)|^2 e^{-i\frac{k}{2z}(x-x_R)^2} e^{i\frac{k}{2z}(x'-x_R)^2} dx_R \\
&= \frac{e^{-(x^2+x'^2)/2\sigma_T^2}}{\lambda z} e^{i\frac{k}{2z}(x'^2-x^2)} \int e^{-x_R^2/\sigma_R^2} e^{i\frac{k}{z}(x-x')x_R} dx_R \\
&= \frac{e^{-(x^2+x'^2)/2\sigma_T^2}}{\lambda z} e^{i\frac{k}{2z}(x'^2-x^2)} L_R e^{-k^2\sigma_R^2(x-x')^2/4z^2} \\
&= \frac{e^{-(x^2+x'^2)/2\sigma_T^2}}{\lambda z} e^{i\frac{k}{2z}(x'^2-x^2)} L_R e^{-2D_F^2(x-x')^2/2\sigma_T^2}.
\end{aligned} \tag{2.44}$$

Our eigenequation now becomes

$$\begin{aligned}
\eta_m \psi_m(x) &= \int K(x, x') \psi_m(x') \\
&= \frac{L_R}{\lambda z} \int e^{-(x^2+x'^2)/2\sigma_T^2} e^{i\frac{k}{2z}(x'^2-x^2)} e^{-2D_F^2(x-x')^2/2\sigma_T^2} \psi_m(x') dx'.
\end{aligned} \tag{2.45}$$

If we make the substitution

$$\psi(x) = \psi'(x) \exp\left(-i\frac{k}{2z}x^2\right), \tag{2.46}$$

then this becomes the real-valued eigenequation

$$\begin{aligned}
\eta_m \psi'_m(x) &= e^{i\frac{k}{2z}x^2} \int K_{1D}(x, x') \psi_m(x') \\
&= \frac{L_R}{\lambda z} \int e^{-(x^2+x'^2)/2\sigma_T^2} e^{-2D_F^2(x-x')^2/2\sigma_T^2} \psi'_m(x') dx' \\
&= \frac{L_R}{\lambda z} \int e^{-(1+2D_F^2)(x^2+x'^2)/2\sigma_T^2} e^{4D_F^2xx'/2\sigma_T^2} \psi'_m(x') dx'.
\end{aligned} \tag{2.47}$$

Using a substitution of variables we can write the exponential function as

$$\begin{aligned} \exp\left(\frac{-(1+2D_F^2)(x^2+x'^2)+4D_F^2xx'}{2\sigma_T^2}\right) &= \exp\left(\frac{-(1+t^2)(y^2+z^2)+4tyz}{2(1-t^2)}\right) \\ &= \sqrt{\pi(1-t^2)} \sum_n \text{HG}_n(y) \text{HG}_n(z) t^n, \end{aligned} \quad (2.48)$$

where we have used Mehler's formula [22] to express the exponential function in terms of a bilinear expansion using the complete and orthogonal Hermite-Gaussian functions.

These functions are given by

$$\text{HG}_n(z) = \frac{1}{\sqrt{2^n n!} \sqrt{\pi}} e^{-z^2/2} H_n(z), \quad (2.49)$$

where $H_n(z)$ are the Hermite polynomials which can be written as

$$H_n(z) = (-1)^n e^{x^2} \frac{d^n}{dx^n} e^{-x^2}. \quad (2.50)$$

The first few Hermite-Gaussian functions are plotted in Fig. 2.2. The value of n corresponds to the degree of the Hermite polynomial $H_n(z)$ that makes up $\text{HG}_n(z)$. As a result of this the HG_n mode will have $n-1$ nodes and thus a larger mode number can be seen as corresponding to higher spatial frequencies of the mode. In addition the width (or variance) of the function itself will also grow with n as can be seen in the figure.

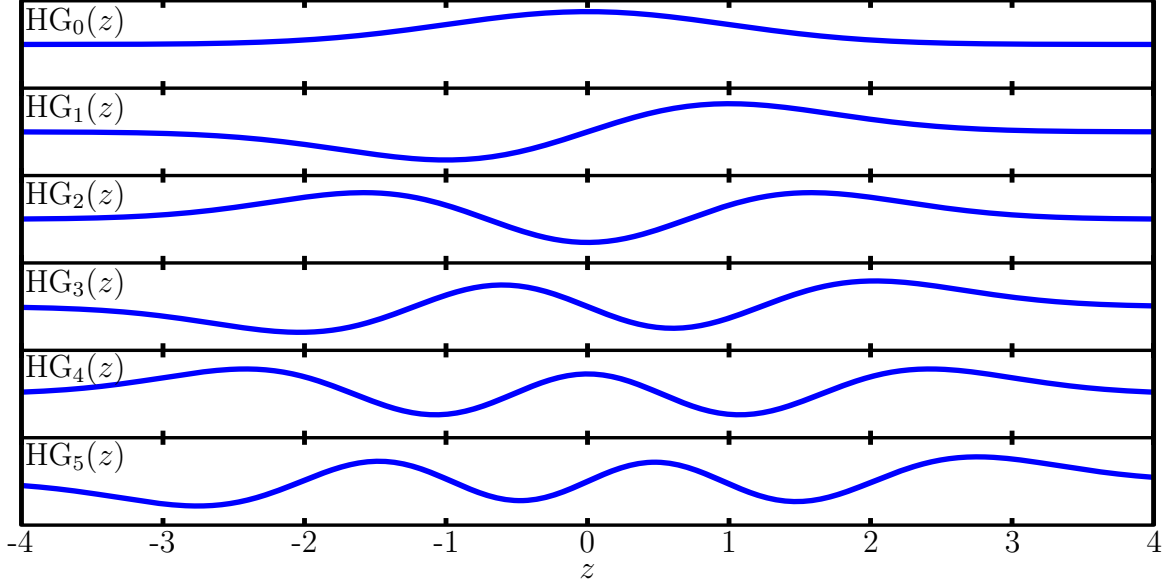


Figure 2.2: Plots of the six lowest order Hermite-Gaussian functions $HG_n(z)$ given by the expression in Eq. (2.49).

The substitution in Eq. (2.48) is true if we have

$$y = \sqrt{\frac{1-t^2}{1+t^2}} \frac{\sqrt{1+2D_F^2}}{\sigma_T} x, \quad z = \sqrt{\frac{1-t^2}{1+t^2}} \frac{\sqrt{1+2D_F^2}}{\sigma_T} x', \quad (2.51)$$

$$\text{and } \frac{t}{1+t^2} = \frac{D_F^2}{1+2D_F^2}.$$

Solving for t gives

$$t = \frac{1+2D_F^2 - \sqrt{1+4D_F^2}}{2D_F^2} \quad (2.52)$$

and

$$y = \frac{(1+4D_F^2)^{1/4}}{\sigma_T} x, \quad z = \frac{(1+4D_F^2)^{1/4}}{\sigma_T} x'. \quad (2.53)$$

With this substitution our eigenequation becomes

$$\begin{aligned}
\eta_m \psi'_m(y) &= \frac{L_R}{\lambda z} \int e^{-(1+2D_F^2)(x^2+x'^2)/2\sigma_T^2} e^{4D_F^2 xx'/2\sigma_T^2} \psi'_m(x') dx' \\
&= \frac{D_F}{\sqrt{1+2D_F^2}} \sqrt{1+t^2} \sum_n t^n \text{HG}_n(y) \int \text{HG}_n(z) \psi'_m(z) dz \\
&= \sqrt{t} \sum_n t^n \text{HG}_n(y) \int \text{HG}_n(z) \psi'_m(z) dz \\
&= \sqrt{t} t^m \psi'_m(y),
\end{aligned} \tag{2.54}$$

where the integration is performed by assuming that $\psi'_m(z) \propto \text{HG}_m(z)$. We have therefore found the communication modes which are given by the normalized functions

$$\psi_m(x) = \sqrt{\frac{(1+4D_F^2)^{1/4}}{\sigma_T}} \text{HG}_m \left(\frac{(1+4D_F^2)^{1/4}}{\sigma_T} x \right) e^{-i\frac{k}{2z}x^2} \tag{2.55}$$

in Alice's aperture, and similarly by

$$\phi_m(x) = \sqrt{\frac{(1+4D_F^2)^{1/4}}{\sigma_R}} \text{HG}_m \left(\frac{(1+4D_F^2)^{1/4}}{\sigma_R} x \right) e^{i\frac{k}{2z}x^2} \tag{2.56}$$

at Bob's aperture. These modes have a power coupling efficiency given by the eigenvalues

$$\eta_m = \sqrt{t} t^m = \left(\frac{1+2D_F^2 - \sqrt{1+4D_F^2}}{2D_F^2} \right)^{\frac{1}{2}+m}. \tag{2.57}$$

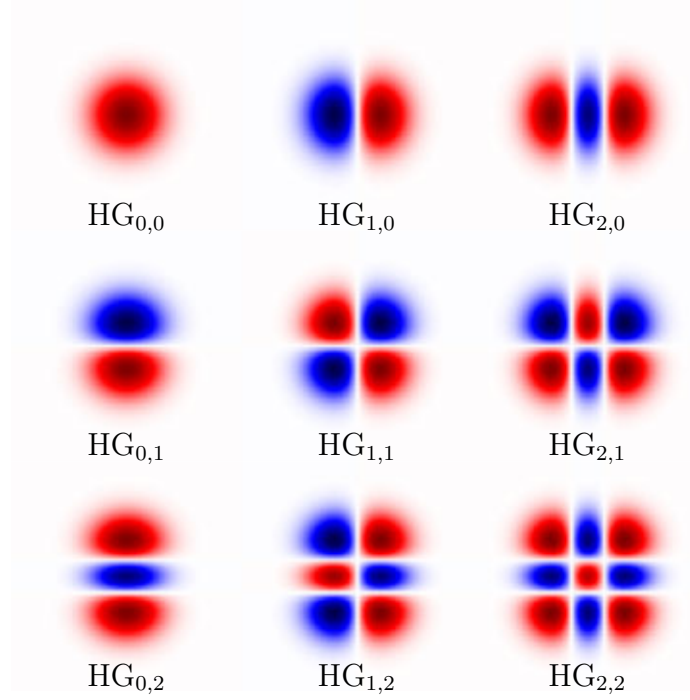


Figure 2.3: Plots of the nine lowest order 2D Hermite-Gaussian wavefunctions $\text{HG}_{m,n}(x, y)$ given by the expression in Eq. (2.61). The magnitude of the amplitude is represented by the color brightness, while phase (e.g. sign) is represented by the color hue with red representing a real and positive value and blue representing a real and negative value.

The full two dimensional solutions are just given as the product of the one dimensional solution, i.e.

$$\Psi_{m,n}(x, y) = \psi_m(x) \times \psi_n(y), \quad \Phi_{m,n}(x, y) = \phi_m(x) \times \phi_n(y), \quad (2.58)$$

$$\text{and } \eta_{m,n} = \eta_m \times \eta_n.$$

In particular, if $\sigma_{R,x} = \sigma_{R,y} = \sigma_R$ and $\sigma_{T,x} = \sigma_{T,y} = \sigma_T$ then the communication modes are given by

$$\begin{aligned} \Psi_{m,n}(x, y) &= \frac{(1 + 4D^2)^{1/4}}{\sigma_T} \exp\left(-i \frac{k}{2z} (x^2 + y^2)\right) \\ &\times \text{HG}_{m,n}\left(\frac{(1 + 4D^2)^{1/4}}{\sigma_T} x, \frac{(1 + 4D^2)^{1/4}}{\sigma_T} y\right) \end{aligned} \quad (2.59)$$

in Alice's aperture, and similarly by

$$\begin{aligned} \Phi_{m,n}(x, y) &= \frac{(1 + 4D^2)^{1/4}}{\sigma_R} \exp\left(i \frac{k}{2z} (x^2 + y^2)\right) \\ &\times \text{HG}_{m,n}\left(\frac{(1 + 4D^2)^{1/4}}{\sigma_R} x, \frac{(1 + 4D^2)^{1/4}}{\sigma_R} y\right) \end{aligned} \quad (2.60)$$

at Bob's aperture, where we have defined the two dimensional Hermite-Gaussian functions

$$\text{HG}_{m,n}(x, y) \equiv \text{HG}_m(x) \times \text{HG}_n(y). \quad (2.61)$$

These modes have a power coupling efficiency given by the eigenvalues

$$\eta_{m,n} = \eta_m \times \eta_n = t^{1+m+n} = \left(\frac{1 + 2D_{F,2D} - \sqrt{1 + 4D_{F,2D}}}{2D_{F,2D}}\right)^{1+m+n}, \quad (2.62)$$

where

$$D_{F,2D} = D_{F,x} \times D_{F,y} = D_F^2 \quad (2.63)$$

is the usual (two dimensional) Fresnel number product.

We can use the expression for the power efficiencies $\eta_{m,n}$ given by Eq. (2.62) to compute the informational capacity of the channel. For communication using single photons the capacity as given by Eq. (2.18) is

$$\begin{aligned}
C^{\text{QKD}} &= - \sum_{m,n} p^{\text{QKD}}(a_n) \eta_{m,n} \log(p^{\text{QKD}}(a_n)) \\
&= - \sum_{m,n} \exp\left(\frac{\lambda}{\eta_{m,n}} - 1\right) \eta_{m,n} \log\left(\exp\left(\frac{\lambda}{\eta_{m,n}} - 1\right)\right) \\
&= - \sum_{m,n} \exp\left(\frac{\lambda}{t^{1+m+n}} - 1\right) t^{1+m+n} \log\left(\exp\left(\frac{\lambda}{t^{1+m+n}} - 1\right)\right),
\end{aligned} \tag{2.64}$$

where λ is the Lagrange multiplier that must be chosen such that the probabilities are properly normalized.

There is no simple analytic formula for λ in Eq. (2.64), so one must resort to using numerical methods such as by minimizing the error function

$$\epsilon(\lambda) \equiv \left(1 - \sum_{m,n} p_{m,n}(\lambda)\right)^2 = \left(1 - \sum_{m,n} \exp\left(\frac{\lambda}{t^{1+m+n}} - 1\right)\right)^2. \tag{2.65}$$

The results of numerically computing the channel capacity from Eq. (2.18) for a range of values for the Fresnel number product $N_{F,2D}$ are plotted in Fig. 2.4. As is shown in the figure the capacity can be expressed as

$$C^{\text{QKD}} \approx \frac{1}{2} \log(D_{F,2D}). \tag{2.66}$$

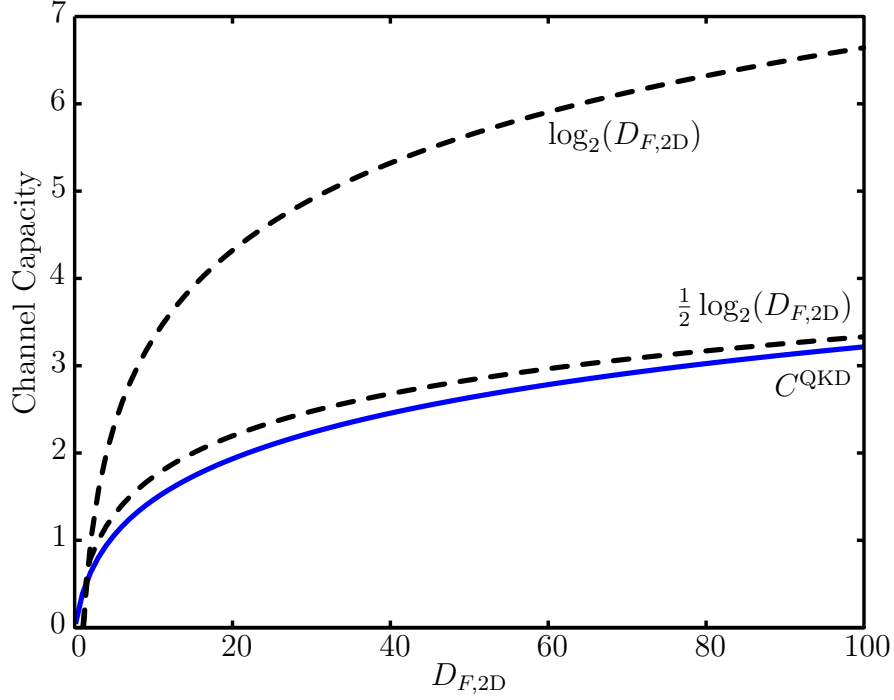


Figure 2.4: Plot of the single photon channel capacity for a free-space channel with apodized apertures encoded using the Hermite-Gaussian communication modes of the channel as given by Eq. (2.64). Also plotted (dashed lines) for comparison are the plots for $\log(D_{F,2D})$ and $\frac{1}{2} \log(D_{F,2D})$.

The classical channel capacity given by Eq. (2.23) is simply $\log N$, where N is the number of modes with efficiencies greater than η_{\min} . This means we are only considering modes $\text{HG}_{m,n}$ such that

$$\eta_{m,n} = t^{1+m+n} > \eta_{\min}. \quad (2.67)$$

The maximum value of N_{\max} such that $m + n < N_{\max}$ is given by

$$\eta_{\min} = t^{1+N_{\max}} \rightarrow N_{\max} = \frac{\log(\eta_{\min})}{\log(t)} - 1. \quad (2.68)$$

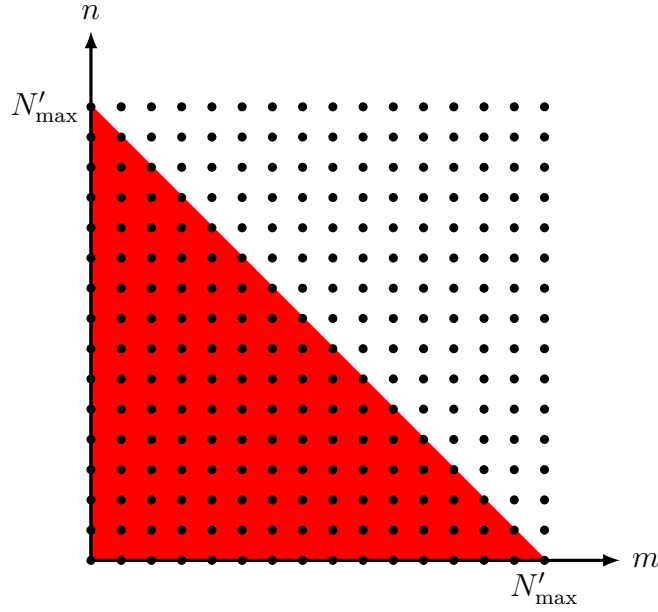


Figure 2.5: A configuration space diagram of Hermite-Gaussian communication modes $\text{HG}_{m,n}$. The red area indicates those states for which $m + n \leq N'_{\max}$.

The total number of modes N is given by counting all the modes $\text{HG}_{m,n}$ such that $m + n < N_{\max}$ which is shown diagrammatically as the modes in the red region in Fig. 2.5. This is equivalent to

$$\begin{aligned}
 N &= \sum_{m+n < N_{\max}} 1 \\
 &= \sum_{m=0}^{N'_{\max}} \left(\sum_{n=0}^{N'_{\max}-m} 1 \right) \\
 &= \sum_{m=0}^{N'_{\max}} (N'_{\max} - m + 1) \\
 &= \frac{1}{2}(N'_{\max} + 2)(N'_{\max} + 1),
 \end{aligned} \tag{2.69}$$

where $N'_{\max} = \lfloor N_{\max} \rfloor$ is the largest interger less than N_{\max} . Therefore the channel capacity is

$$\begin{aligned} C^{\text{classical}} &= \log \left(\frac{1}{2} (N'_{\max} + 2)(N'_{\max} + 1) \right) \\ &\approx \log \left(\frac{1}{2} \left(\frac{\log(\eta_{\min})}{\log(t)} + 1 \right) \frac{\log(\eta_{\min})}{\log(t)} \right). \end{aligned} \quad (2.70)$$

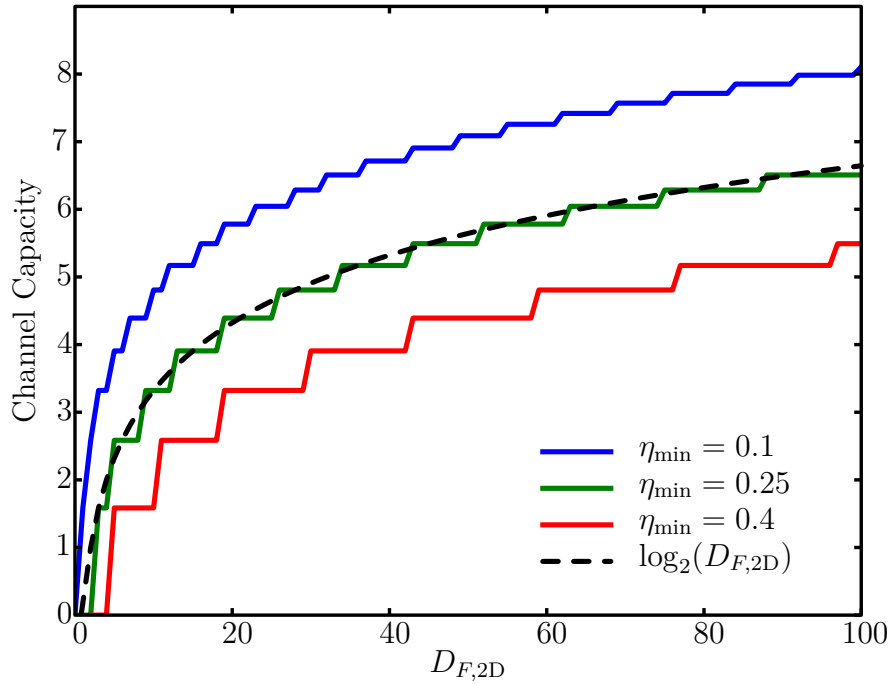


Figure 2.6: Plots of the classical channel capacity for a free-space channel with apodized apertures encoded using the Hermite-Gaussian communication modes of the channel for various threshold values η_{\min} . Also plotted (dashed lines) for comparison is the plot for $\log_2(D_{F,2D})$.

The classical channel capacity was computed and the results are plotted in Fig. 2.6.

The capacity was plotted for a range of values for η_{\min} from 0.1 to 0.4. In addition a dashed curve representing $\log_2(D_{F,2D})$ is also shown. As can be seen a threshold value

of $\eta_{\min} = 0.25$ gives a capacity that is close to $\log(D_{F,2D})$, while smaller values of η_{\min} give larger capacities and vice versa.

2.5.2 Hard rectangular apertures

Although the Gaussian apodized pupils given in Eq. (2.41) allowed us to analytically solve the one dimensional eigenequations of Eq. (2.38), a more realistic situation is to have hard apertures. For hard apertures with Cartesian or rectangular symmetry the (one dimensional) pupil functions are given by

$$P_T(x) = \text{rect}\left(\frac{x}{L_T}\right) \quad \text{and} \quad P_R(x) = \text{rect}\left(\frac{x}{L_R}\right), \quad (2.71)$$

where $\text{rect}(x)$ is the rectangle function defined as

$$\text{rect}(x) = \begin{cases} 1 & \text{for } |x| < \frac{1}{2} \\ 0 & \text{otherwise} \end{cases}. \quad (2.72)$$

We can see immediately that L_T and L_R are the characteristic lengths based on Eq. (2.40) as

$$\int |P(x)|^2 dx = \int P(x) dx = \int \text{rect}\left(\frac{x}{L}\right) dx = L. \quad (2.73)$$

This system also has the simple (one dimensional) Fresnel number product as given in Eq. (2.39) of

$$D_F = \frac{L_R L_T}{\lambda z}. \quad (2.74)$$

Now again we must compute the kernel K_{1D} by plugging the pupil expressions into Eq. (2.36). Doing this gives

$$\begin{aligned}
K_{1D}(x, x') &= \frac{P_T(x)P_T(x')}{\lambda z} \int |P_R(x_R)|^2 e^{-i\frac{k}{2z}(x-x_R)^2} e^{i\frac{k}{2z}(x'-x_R)^2} dx_R \\
&= \frac{\text{rect}\left(\frac{x}{L_T}\right)\text{rect}\left(\frac{x'}{L_T}\right)}{\lambda z} e^{i\frac{k}{2z}(x'^2-x^2)} \int \text{rect}\left(\frac{x_R}{L_R}\right) e^{i\frac{k}{z}(x-x')x_R} dx_R \\
&= \frac{\text{rect}\left(\frac{x}{L_T}\right)\text{rect}\left(\frac{x'}{L_T}\right)}{\lambda z} e^{i\frac{k}{2z}(x'^2-x^2)} L_R \text{sinc}\left(\frac{L_R}{\lambda z}(x-x')\right) \\
&= \frac{\text{rect}\left(\frac{x}{L_T}\right)\text{rect}\left(\frac{x'}{L_T}\right)}{\lambda z} e^{i\frac{k}{2z}(x'^2-x^2)} L_R \text{sinc}\left(D_F \frac{x-x'}{L_T}\right),
\end{aligned} \tag{2.75}$$

where the function $\text{sinc}(x)$ is defined to be

$$\text{sinc}(x) \equiv \frac{\sin(\pi x)}{\pi x}. \tag{2.76}$$

As we did before, we make the substitution

$$\psi(x) = \psi'(x) \exp\left(-i\frac{k}{2z}x^2\right), \tag{2.77}$$

which gives us the real-valued eigenequation

$$\begin{aligned}
\eta_m \psi'_m(x) &= e^{i\frac{k}{2z}x^2} \int K_{1D}(x, x') \psi_m(x') \\
&= \frac{D_F}{L_T} \text{rect}\left(\frac{x}{L_T}\right) \int \text{rect}\left(\frac{x'}{L_T}\right) \text{sinc}\left(D_F \frac{x-x'}{L_T}\right) \psi'_m(x') dx'.
\end{aligned} \tag{2.78}$$

The solutions to Eq. (2.78) are known as the prolate spheroidal wavefunctions (PSWs) [23]. Writing Eq. (2.78) in standard form [24] gives

$$2R_{0,m}^2(c, 1)S_{0,m}(c, t) = \int_{-1}^1 \operatorname{sinc}\left(\frac{c(t-s)}{\pi}\right) S_{0,m}(c, s) ds, \quad (2.79)$$

which is equivalent to Eq. (2.78) with the substitutions

$$s = \frac{2x'}{L_T}, \quad t = \frac{2x}{L_T}, \quad c = \frac{\pi D_F}{2}, \quad (2.80)$$

$$R_{0,m}^2(c, 1) = \frac{\eta_m}{D_F}, \quad \text{and} \quad \psi'_m(t) = S_{0,m}(c, t).$$

The functions $S_{m,n}(c, t)$ and $R_{m,n}(c, t)$ are known as the angular prolate spheroidal and radial prolate spheroidal functions respectively. These functions are solutions of the differential eigenequation [24]

$$(t^2 - 1)\frac{d^2u}{dt^2} + 2t\frac{du}{dt} + \left(c^2t^2 - \frac{m^2}{t^2 - 1}\right)u = \lambda_{m,n}u, \quad (2.81)$$

where

$$u_{m,n}(c, t) = \begin{cases} S_{m,n}(c, t) & \text{for } |t| \leq 1 \\ R_{m,n}(c, t) & \text{for } |t| \geq 1 \end{cases}. \quad (2.82)$$

Our eigenvalues, which are related to the radial prolate spheroidal functions, are given by

$$\eta_m = D_F R_{0,m}^2(c, 1) = D_F R_{0,m}^2\left(\frac{\pi D_F}{2}, 1\right). \quad (2.83)$$

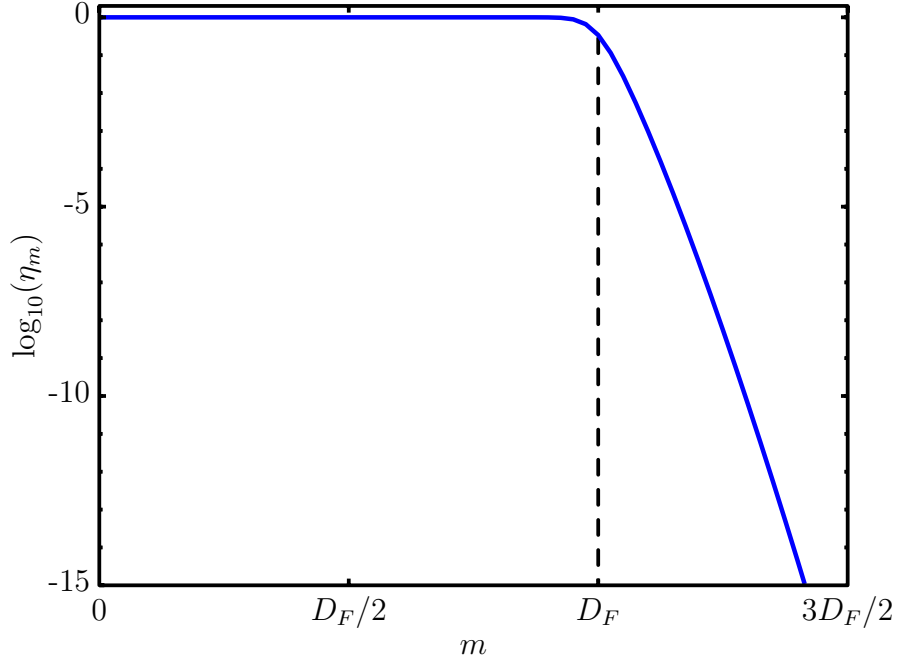


Figure 2.7: Plot of the transmission efficiencies η_m for a free-space channel with hard apertures encoded using the prolate spheroidal communication modes of the channel. The efficiencies display a sharp cutoff for $m > D_F$.

A plot of η_m is given in Fig. 2.7. Generally, η_m falls off very rapidly for $m \geq D_F$.

Therefore, for systems with $D_F > 1$, the eigenvalues are well approximated by the step functions

$$\eta_m = \begin{cases} 1 & \text{for } m < D_F \\ 0 & \text{otherwise} \end{cases}. \quad (2.84)$$

For $D_F \leq 1$ we only have approximately one mode which is transmitted with an efficiency

$$\eta \approx D_F. \quad (2.85)$$

It is a general feature of systems with hard apertures to have an abrupt cutoff in the transmission of spatial modes as one goes to larger spatial frequencies [25]. This can

be simply understood using Abbe's model of diffraction in which optical propagation between pupils is understood in terms of geometrical optical rays [20]. Each ray leaves the aperture at a different angle with larger angles being associated with larger spatial frequencies. The light that can be collected after the second pupil is simply the sum of all spatial frequencies that are within the solid angle of the pupil. Since the aperture has a hard edge, there is a hard cutoff in the angle of the rays that make it into the aperture. This is represented diagrammatically in Fig. 2.8.

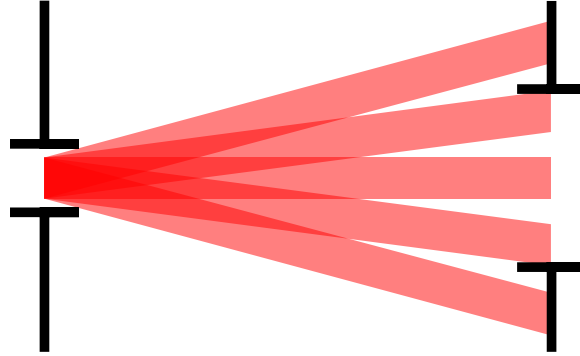


Figure 2.8: Schematic representing Abbe's model of diffraction in which a field at a pupil can be represented by a set of geometrical rays representing the different spatial frequency components of that field within the first aperture. The second aperture blocks the rays representing the high order spatial frequencies while leaving untouched the moderate and low order frequencies.

The sharp cutoff in the spectrum of η_m , as well as the fact that $\sum \eta = D_F$, means that we essentially have D_F good modes to communicate with nearly lossless transmission. For a classical channel this gives a capacity of

$$C^{\text{classical}} = \log(D_F). \quad (2.86)$$

We expect this also to be the case for communication with single photons. Again we use the expression in Eq. (2.18) for communication using single photons given as

$$\begin{aligned} C^{\text{QKD}} &= - \sum_m p^{\text{QKD}}(a_m) \eta_m \log(p^{\text{QKD}}(a_m)) \\ &= - \sum_m \exp\left(\frac{\lambda}{\eta_m} - 1\right) \eta_m \log\left(\exp\left(\frac{\lambda}{\eta_m} - 1\right)\right), \end{aligned} \quad (2.87)$$

and solve for the value of λ that properly normalizes the probabilities. The results are plotted in Fig. 2.9 along with $\log(D_F)$ (as the dashed line). As can clearly be seen, the two are nearly identical and thus to a very good approximation we can claim that

$$C^{\text{QKD}} = \log(D_F). \quad (2.88)$$

We have also updated the eigenfunctions to Eq. (2.78) which are given by

$$\psi_m(x) = S_{o,m} \left(\frac{\pi D_F}{2}, \frac{2x}{L_T} \right) \exp\left(-i \frac{k}{2z} x^2\right) \quad (2.89)$$

at Alice. Repeating the procedure to find the modes at Bob gives us the kernel K'_{1D} in the eigenequation for ϕ_m that is identical to the complex conjugate of K_{1D} if we make the substitution

$$L_T \rightarrow L_R. \quad (2.90)$$

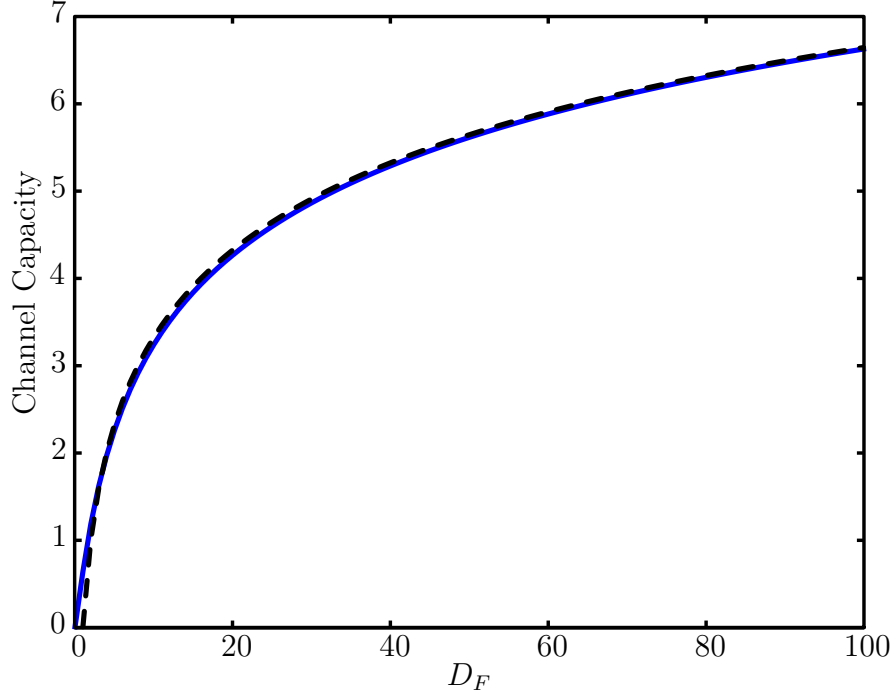


Figure 2.9: Plot of the single photon channel capacity for a free-space channel with hard apertures encoded using the prolate spheroidal communication modes of the channel (Eq. (2.87)). Also plotted (dashed lines) for comparison is the plot for $\log(D_F)$.

Therefore the communication modes at Bob are simply

$$\phi_m(x) = S_{o,m} \left(\frac{\pi D_F}{2}, \frac{2x}{L} \right) \exp \left(i \frac{k}{2z} x^2 \right). \quad (2.91)$$

The functions $S_{o,m}(\pi D_F/2, 2x/L)$ are real and continuous and have exactly m zeros within the aperture (i.e. for $x \in (-L/2, L/2)$) [24]. These eigenfunctions are very similar to the eigenmodes that were derived in section 2.5.1 (Eqs. (2.55) – (2.56)), and for mode numbers $m \ll D_F$, the two sets of modes are nearly indistinguishable [26]. Plots of the communication modes for a system with a (one dimensional) Fresnel number product of $D_F = 5$ are shown in Fig. 2.10 for the modes with non-negligible

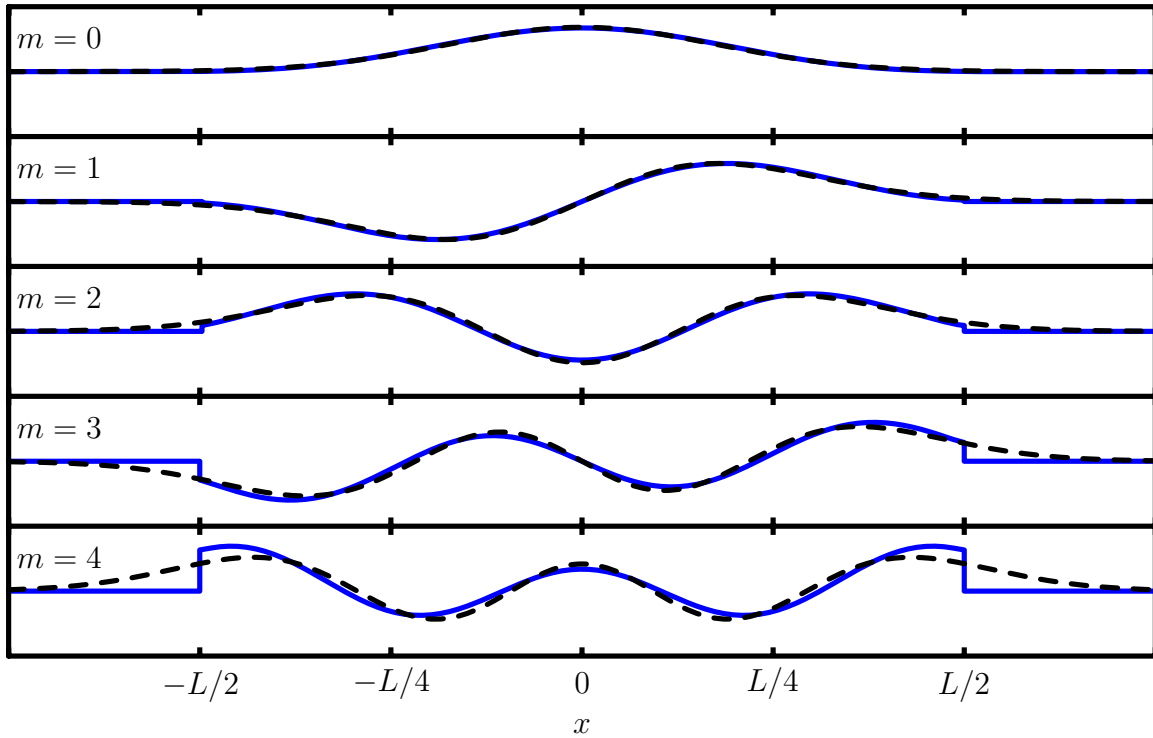


Figure 2.10: Plots of the prolate spheroidal wavefunctions that act as the communication modes for a system with hard apertures and a Fresnel number product of $D_F = 5$. In addition the Hermite-Gaussian communication modes of an analogous channel with Gaussian apodized apertures are plotted (dashed lines) in order to show the close similarities between the two sets of modes.

transmission efficiencies η_m . In addition the Hermite-Gaussian modes for a system with identical Fresnel number product and aperture size $L = \sigma\sqrt{\pi}$ are superimposed as the dashed line demonstrating the similarities between the two sets of modes.

2.6 Cylindrical apertures

The second type of geometry we consider is one in which the pupil functions are cylindrically symmetric, i.e.

$$P_T(\mathbf{r}) = P_T(r) \quad \text{and} \quad P_R(\mathbf{r}) = P_R(r), \quad (2.92)$$

where $r \equiv |\mathbf{r}|$. The area of such pupils can be given by the one dimensional integral over r as

$$A \equiv \iint |P(r)|^2 d\mathbf{r} = 2\pi \int |P(r)|^2 r dr. \quad (2.93)$$

Such a geometry represents round pupils which is a more typical case relative to the geometry discussed in section 2.5. Assuming such a geometry, Eq. (2.31) can be written as

$$\begin{aligned} K(\mathbf{r}_T, \mathbf{r}'_T) &= \frac{P_T^*(r_T)P_T(r'_T)}{(\lambda z)^2} \iint |P_R(r_R)|^2 e^{-i\frac{k}{2z}|\mathbf{r}_T - \mathbf{r}_R|^2} e^{i\frac{k}{2z}|\mathbf{r}'_T - \mathbf{r}_R|^2} d\mathbf{r}_R \\ &= \frac{P_T^*(r_T)P_T(r'_T)}{(\lambda z)^2} \exp\left(\frac{ik}{2z}(r_T'^2 - r_T^2)\right) \iint |P_R(r_R)|^2 \\ &\quad \times \exp\left[i\frac{kr_R}{z}\left(r_T \cos(\phi_R - \phi_T) - r'_T \cos(\phi_R - \phi'_T)\right)\right] d\mathbf{r}_R. \end{aligned} \quad (2.94)$$

We can expand the exponential terms in the integral in terms of Bessel functions using the identity

$$e^{iz \cos(\phi)} = \sum_{n=-\infty}^{\infty} i^n e^{in\phi} J_n(z), \quad (2.95)$$

where the functions $J_n(z)$ are the Bessel functions which can be defined by the generating sequence [27]

$$e^{\frac{1}{2}(t-1/t)z} = \sum_{n=-\infty}^{\infty} t^n J_n(z). \quad (2.96)$$

Equation (2.95) is known as the Jacobi-Anger expansion and is derived by the substitution $t = i \exp(i\phi)$ in Eq. (2.96). Therefore our kernel becomes

$$\begin{aligned} K(\mathbf{r}_T, \mathbf{r}'_T) &= \frac{P_T^*(r_T)P_T(r'_T)}{(\lambda z)^2} e^{\frac{ik}{2z}(r_T'^2 - r_T^2)} (-1)^n i^{m+n} \int |P_R(r_R)|^2 r_R dr_R \\ &\quad \times \sum_{m,n} e^{in\phi'_T} e^{-im\phi_T} J_m\left(\frac{kr_R r_T}{z}\right) J_n\left(\frac{kr_R r'_T}{z}\right) \int_0^{2\pi} e^{i(m-n)\phi_R} d\phi_R \\ &= \frac{P_T^*(r_T)P_T(r'_T)}{(\lambda z)^2} e^{\frac{ik}{2z}(r_T'^2 - r_T^2)} \sum_m e^{im(\phi'_T - \phi_T)} \\ &\quad \times 2\pi \int |P_R(r_R)|^2 J_m\left(\frac{kr_R r_T}{z}\right) J_m\left(\frac{kr_R r'_T}{z}\right) r_R dr_R. \end{aligned} \quad (2.97)$$

Now if we make the substitution

$$\Psi_{\ell,p}(r, \phi) = \psi_{\ell,p}(r) e^{-i\frac{k}{2z}r^2} e^{i\ell\phi}, \quad (2.98)$$

where we have used the ansatz that all of the azimuthal dependence is due to $e^{i\ell\phi}$, where ℓ is an integer, then our eigenequation (Eq. (2.29)) becomes

$$\begin{aligned}
\eta_{\ell,p}\psi_{\ell,p}(r) &= \iint e^{-\frac{ik}{2z}(r'^2-r^2)} e^{i\ell\phi} e^{-i\ell\phi'} K(\mathbf{r}, \mathbf{r}') \psi_{\ell,p}(r') \, d\mathbf{r}' \\
&= \frac{P_T^*(r)P_T(r')}{(\lambda z)^2} \sum_m \int e^{i(\ell-m)\phi} e^{-i(\ell-m)\phi'} \, d\phi' \int \psi_{\ell,p}(r') r' \, dr' \\
&\quad \times 2\pi \int |P_R(r_R)|^2 J_m\left(\frac{kr_R r'}{z}\right) J_m\left(\frac{kr_R r'}{z}\right) r_R \, dr_R \\
&= \left(\frac{k}{z}\right)^2 P_T^*(r) \int |P_R(r_R)|^2 J_\ell\left(\frac{kr_R r'}{z}\right) r_R \, dr_R \\
&\quad \times \int P_T(r') \psi_{\ell,p}(r') J_\ell\left(\frac{kr_R r'}{z}\right) r' \, dr'.
\end{aligned} \tag{2.99}$$

We can simplify Eq. (2.99) if we assume that the pupil functions P_T and P_R are simply scaled versions with the same functional form. Therefore, we assume we can write our pupil functions as

$$P_T(\rho L_T) = P_R(\rho L_R) = P(\rho), \tag{2.100}$$

where L_T and L_R are characteristic lengths for the transmitter and receiver pupils respectively, and ρ is a dimensionless radial coordinate. Now if we rewrite Eq. (2.99) with the coordinate change

$$\rho = r/L_T, \quad \rho' = r'/L_T, \quad \text{and} \quad \rho_R = r_R/L_R, \tag{2.101}$$

then we get

$$\begin{aligned} \eta_{\ell,p}\psi_{\ell,p}(\rho) = \\ c^2 P^*(\rho) \int |P(\rho_R)|^2 J_\ell(c\rho_R\rho) \rho_R d\rho_R \int P(\rho')\psi_{\ell,p}(\rho') J_\ell(c\rho_R\rho') \rho' d\rho', \end{aligned} \quad (2.102)$$

where

$$c = kL_T L_R / z. \quad (2.103)$$

Eigenfunctions of the above equation are also eigenfunctions of the simpler equation

$$\lambda_{\ell,p}\psi_{\ell,p}(\rho) = P^*(\rho) \int P(\rho')\psi_{\ell,p}(\rho') J_\ell(c\rho'\rho) \rho' d\rho'. \quad (2.104)$$

This can be shown by applying the integral operator

$$\hat{\mathcal{O}} = P^*(\bar{\rho}) \int P(\rho) J(c\rho\bar{\rho}) \rho d\rho \quad (2.105)$$

to Eq. (2.104), i.e.

$$\begin{aligned} \lambda_{\ell,p}\hat{\mathcal{O}}\psi_{\ell,p}(\rho) &= \lambda_{\ell,p}^2\psi_{\ell,p}(\bar{\rho}) \\ &= P^*(\bar{\rho}) \int |P(\rho)|^2 J_\ell(c\rho\bar{\rho}) \rho d\rho \\ &\quad \times \int P(\rho')\psi_{\ell,p}(\rho') J_\ell(c\rho\rho') \rho' d\rho', \end{aligned} \quad (2.106)$$

which is identical to Eq. (2.102) with

$$\lambda_{\ell,p} = \frac{\sqrt{\eta_{\ell,p}}}{c}. \quad (2.107)$$

Therefore we only need to solve Eq. (2.104) to find the communication modes.

2.6.1 Gaussian apodized apertures

In order to go any further in solving Eq. (2.104), we need to specify the form of the apertures. As we did in section 2.5.1, we first consider Gaussian apodized apertures in order to obtain analytic solutions [21] to gain physical insight and intuition to the problem. Such apertures are specified by the radial pupil functions

$$P_T(r) = \exp\left(\frac{-r^2}{2\sigma_T^2}\right) \quad \text{and} \quad P_R(r) = \exp\left(\frac{-r^2}{2\sigma_R^2}\right). \quad (2.108)$$

Such apertures have areas based on Eq. (2.93) of

$$A_{R/T} = 2\pi \int |P_{R/T}(r)|^2 r \, dr = 2\pi \int \exp\left(\frac{-r^2}{\sigma_{R/T}^2}\right) r \, dr = \pi\sigma_{R/T}^2, \quad (2.109)$$

and therefore the Fresnel number product of this system is

$$D_F = \frac{A_R A_T}{(\lambda z)^2} = \left(\frac{\pi\sigma_R\sigma_T}{\lambda z}\right)^2 = \left(\frac{k\sigma_R\sigma_T}{2z}\right)^2. \quad (2.110)$$

The Gaussian widths σ_T and σ_R provide natural lengths for the transmitter and pupil receiver, and so we use

$$L_T = \sigma_T \quad \text{and} \quad L_R = \sigma_R \quad (2.111)$$

for our normalized coordinates as defined by Eq. (2.101). In this case our general pupil function is simply

$$P(\rho) = \exp(-\rho^2/2), \quad (2.112)$$

and Eq. (2.104) becomes

$$\begin{aligned} \lambda_{\ell,p} \psi_{\ell,p}(\rho) &= P^*(\rho) \int P(\rho') \psi_{\ell,p}(\rho') J_\ell(c\rho'\rho) \rho' d\rho' \\ &= e^{-\rho^2/2} \int e^{-\rho'^2/2} \psi_{\ell,p}(\rho') J_\ell(c\rho'\rho) \rho' d\rho'. \end{aligned} \quad (2.113)$$

In addition we have that the scaling parameter c is given by

$$c = \frac{k\sigma_T\sigma_R}{z} = 2\sqrt{D_F}. \quad (2.114)$$

Using a substitution of variables we can write

$$\begin{aligned} e^{-\frac{1}{2}(\rho^2+\rho'^2)} J_\ell(c\rho'\rho) &= e^{-\frac{1}{2}(x+y)\left(\frac{1-t}{1+t}\right)} J_\ell\left(\frac{2\sqrt{xyt}}{1+t}\right) \\ &= (1+t)t^{|\ell|/2} \sum_n t^n \phi_n^\ell(x) \phi_n^\ell(y), \end{aligned} \quad (2.115)$$

where we have used the Hill-Hardy theorem [28] to express the function in terms of a bilinear expansion using the complete and orthogonal Laguerre functions. These functions are given by

$$\phi_n^\ell(z) = \sqrt{\frac{n!}{(n+|\ell|)!}} e^{-z/2} z^{|\ell|/2} L_n^{|\ell|}(z), \quad (2.116)$$

where $L_n^{|\ell|}(z)$ are the generalized Laguerre polynomials which can be written as

$$L_n^{|\ell|}(z) = \frac{e^z z^{-|\ell|}}{n!} \frac{d^n}{dz^n} \left(e^{-z} z^{n+|\ell|} \right). \quad (2.117)$$

The substitution in Eq. (2.115) is true if we have

$$\begin{aligned} \rho^2 &= \frac{1-t}{1+t}x, & \rho'^2 &= \frac{1-t}{1+t}y, \\ \text{and } \frac{2\sqrt{xyt}}{1+t} &= c\rho\rho' = 2\sqrt{D_F\rho\rho'}. \end{aligned} \quad (2.118)$$

Solving for t gives

$$t = \frac{1 + 2D_F - \sqrt{1 + 4D_F}}{2D_F} \quad (2.119)$$

and

$$x = \sqrt{1 + 4D_F\rho^2}, \quad y = \sqrt{1 + 4D_F\rho'^2}. \quad (2.120)$$

With this substitution our eigenequation becomes

$$\begin{aligned}
\lambda_{\ell,p}\psi_{\ell,p}(y) &= \int e^{-\frac{1}{2}(x+y)\left(\frac{1-t}{1+t}\right)} J_\ell\left(\frac{2\sqrt{xyt}}{1+t}\right) \psi_{\ell,p}(\rho') \frac{\sqrt{t}}{c(1+t)} dx \\
&= \frac{t^{(|\ell|+1)/2}}{c} \sum_n t^n \phi_n^{|\ell|}(y) \int \phi_n^{|\ell|}(x) \psi_{\ell,p}(x) dx \\
&= \frac{t^{(2p+|\ell|+1)/2}}{c} \phi_p^{|\ell|}(y),
\end{aligned} \tag{2.121}$$

where the integration is performed by assuming that $\psi_{\ell,p}(x) \propto \phi_p^{|\ell|}(x)$. We have therefore found the communication modes which are given by the normalized functions

$$\begin{aligned}
\Psi_{\ell,p}(r, \phi) &= \psi_{\ell,p}(r, \phi) e^{i\ell\phi} e^{-i\frac{k}{2z}r^2} \\
&= \frac{(1+4D_F)^{1/4}}{\sqrt{\pi}\sigma_T} \phi_p^{|\ell|} \left(\frac{\sqrt{1+4D_F}}{\sigma_T} r \right) e^{i\ell\phi} e^{-i\frac{k}{2z}r^2} \\
&= \frac{(1+4D_F)^{1/4}}{\sqrt{\pi}\sigma_T} \text{LG}_p^\ell \left(\frac{(1+4D_F)^{1/4}}{\sigma_T} r, \phi \right) e^{-i\frac{k}{2z}r^2}
\end{aligned} \tag{2.122}$$

at Alice, where LG_p^ℓ are the Laguerre-Gaussian functions defined as

$$\text{LG}_p^\ell(\rho, \phi) = \phi_p^{|\ell|}(\rho^2) e^{i\ell\phi}. \tag{2.123}$$

By symmetry we know that the communication modes at Bob's aperture are given by

$$\Phi_{\ell,p}(r, \phi) = \frac{(1+4D_F)^{1/4}}{\sqrt{\pi}\sigma_R} \text{LG}_p^{\ell*} \left(\frac{(1+4D_F)^{1/4}}{\sigma_R} r, \phi \right) e^{i\frac{k}{2z}r^2}, \tag{2.124}$$

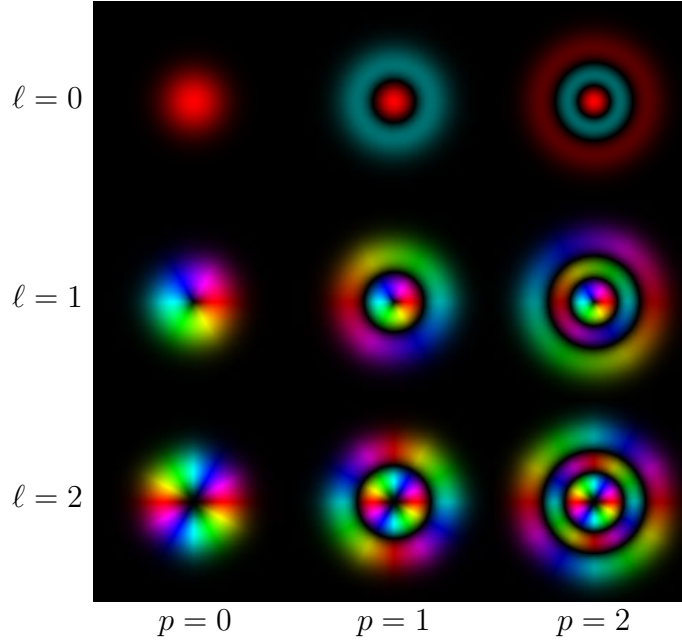


Figure 2.11: Plots of nine of the lowest order Laguerre-Gaussian wavefunctions $\text{LG}_p^\ell(\rho, \phi)$ given by the expression in Eq. (2.123). The complex phase information is represented by the hue of the color in the plots, while the amplitude is represented by the color's brightness.

The LG_p^ℓ communication modes have a power coupling efficiency given by the eigenvalues

$$\eta_{\ell,p} = c^2 \lambda_{\ell,p}^2 = t^{2p+|\ell|+1} = \left(\frac{1 + 2D_F - \sqrt{1 + 4D_F}}{2D_F} \right)^{2p+|\ell|+1}. \quad (2.125)$$

This expression is identical to the expression found in section 2.5.1 for the efficiencies of the Hermite-Gaussian modes of a square Gaussian apodized aperture given in Eq. (2.62) if we replace $2p + |\ell|$ by $m + n$. This is not a coincidence, however as a

square Gaussian function also has cylindrical symmetry, i.e.

$$\exp\left(\frac{-x^2}{2\sigma^2}\right)\exp\left(\frac{-y^2}{2\sigma^2}\right) = \exp\left(\frac{-x^2 - y^2}{2\sigma^2}\right) = \exp\left(\frac{-r^2}{2\sigma^2}\right). \quad (2.126)$$

This additional symmetry is also the reason for the degenerate eigenvalues in either the HG or LG spectrum. In addition, the LG_p^ℓ modes can be expressed as a linear combination of $\text{HG}_{m,n}$ modes (and vice versa) within this degenerate subspace [29] spanned by

$$2p + |\ell| + 1 = m + n + 1 = \text{constant}, \quad (2.127)$$

i.e.

$$\text{LG}_p^\ell(r, \phi) = \sum_{m+n=2p+|\ell|} c_{m,n} \text{HG}_{m,n}(x, y). \quad (2.128)$$

Therefore we know that all the results concerning the channel capacity for a Gaussian apodized channel encoded with LG modes is identical to the results found in section 2.5.1.

2.6.2 Hard circular apertures

As was done in section 2.5, Gaussian apodized apertures allowed for the analytic computation of the communication modes but hard apertures provide a more realistic geometry. For the case of hard apertures, a communication system with cylindrical

symmetry means we have circular apertures with (radial) pupil functionals given by

$$P_T(r) = \text{circ}\left(\frac{r}{R_T}\right) \quad \text{and} \quad P_R(r) = \text{circ}\left(\frac{r}{R_R}\right), \quad (2.129)$$

where $\text{circ}(\rho)$ is the circle function defined as

$$\text{circ}(\rho) = \begin{cases} 1 & \text{for } \rho < 1 \\ 0 & \text{otherwise} \end{cases}. \quad (2.130)$$

These pupils have the obvious areas of

$$A_{R/T} = \pi R_{R/T}^2, \quad (2.131)$$

and therefore such a channel has a Fresnel number product of

$$D_F = \frac{A_R A_T}{(\lambda z)^2} = \left(\frac{\pi R_R R_T}{\lambda z}\right)^2 = \left(\frac{k R_R R_T}{2z}\right)^2. \quad (2.132)$$

The circular widths R_T and R_R provide natural lengths for the transmitter and pupil receiver, and so we use

$$L_T = R_T \quad \text{and} \quad L_R = R_R \quad (2.133)$$

for our normalized coordinates as defined by Eq. (2.101). In this case our general pupil function is simply

$$P(\rho) = \text{circ}(\rho) \quad (2.134)$$

and Eq. (2.104) becomes

$$\begin{aligned} \lambda_{\ell,p} \psi_{\ell,p}(\rho) &= P^*(\rho) \int P(\rho') \psi_{\ell,p}(\rho') J_\ell(c\rho'\rho) \rho' d\rho' \\ &= \text{circ}(\rho) \int_0^1 \psi_{\ell,p}(\rho') J_\ell(c\rho'\rho) \rho' d\rho', \end{aligned} \quad (2.135)$$

where our scaling parameter c is given by

$$c = \frac{kR_T R_R}{z} = 2\sqrt{D_F}. \quad (2.136)$$

The solutions to Eq. (2.135) are known as the circular prolate spheroidal wavefunctions (CPSW), and are the cylindrical analog of the PSWs found in section 2.5.2 [26].

Writing Eq. (2.135) in standard form [30] gives

$$\gamma_{\ell,p} \varphi_{\ell,p}(\rho) = \int_0^1 \sqrt{c\rho\rho'} \varphi_{\ell,p}(\rho') J_\ell(c\rho'\rho) d\rho', \quad (2.137)$$

which is equivalent to Eq. 2.135 with the substitutions

$$\varphi_{\ell,p}(\rho) = \psi_{\ell,p}(\rho) \sqrt{\rho}, \quad \text{and} \quad \gamma_{\ell,p} = \sqrt{c} \lambda_{\ell,p} = \sqrt{\frac{\eta_{\ell,p}}{c}}. \quad (2.138)$$

The functions $\varphi(\rho)$ are known as the generalized prolate spheroidal functions and are also solutions of the differential eigenequation

$$(\rho^2 - 1)\frac{d^2\varphi}{d\rho^2} + 2\rho\frac{d\varphi}{d\rho} + \left(c^2\rho^2 - \frac{1/4 - \ell^2}{\rho^2}\right)\varphi = \chi\varphi, \quad (2.139)$$

which is identical to the differential equation for the prolate spheroidal functions given in Eq. (2.81) except for the $(1/4 - \ell^2)/\rho^2$ term. Finding numerical expressions for $\varphi(\rho)$ is computationally intensive, although there exist approximations that make the problem more tractable [31].

We have therefore found the communication modes which are given by the functions

$$\begin{aligned} \Psi_{\ell,p}(r, \phi) &= \psi_{\ell,p}(r, \phi)e^{i\ell\phi}e^{-i\frac{k}{2z}r^2} \\ &= \frac{\varphi_{\ell,p}(r/R_T, \phi)}{\sqrt{r/R_T}}e^{i\ell\phi}e^{-i\frac{k}{2z}r^2} \\ &= \text{CPSW}_{\ell,p}(r/R_T, \phi)e^{-i\frac{k}{2z}r^2} \end{aligned} \quad (2.140)$$

at Alice and

$$\Phi_{\ell,p}(r, \phi) = \text{CPSW}_{\ell,p}^*(r/R_R, \phi)e^{i\frac{k}{2z}r^2} \quad (2.141)$$

at Bob. We have defined the CPSWs as

$$\text{CPSW}_{\ell,p}(\rho, \phi) \equiv \frac{\varphi_{\ell,p}(\rho, \phi)}{\sqrt{\rho}}e^{i\ell\phi}. \quad (2.142)$$

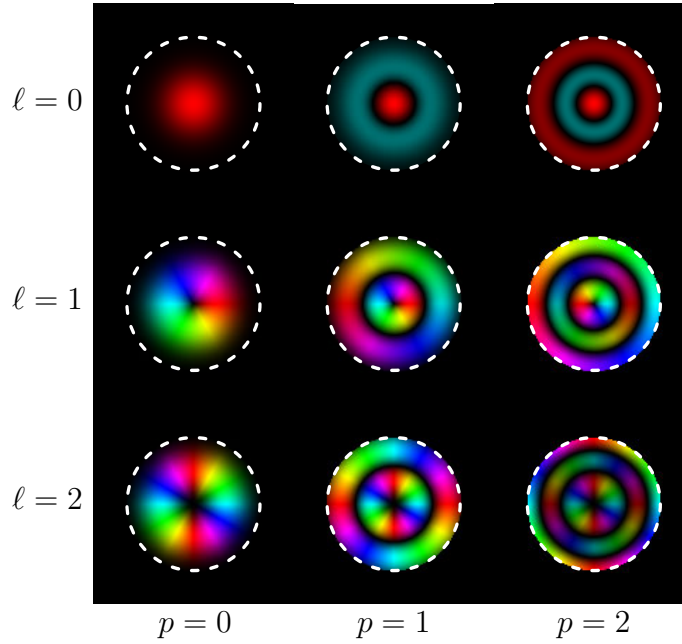


Figure 2.12: Plots of nine of the lowest order CPSWs given by the expression in Eq. (2.142) for a system with hard apertures and a Fresnel number product of $D_F = 25$. The dotted white lines represent the edge of the aperture. The complex phase information is represented by the hue of the color in the plots, while the amplitude is represented by the color's brightness. These modes have the same scaling as the LG modes plotted in Fig. 2.11 in order to show the close similarities between the two sets of modes.

Plots of the communication modes for a system with hard circular apertures and a Fresnel number product of $D_F = 25$ are shown in Fig. 2.12. It was demonstrated in section 2.5.2 that the PSWs communication modes of a system with hard square apertures are very similar to the HG modes of the analogous system with Gaussian apodized apertures. In the same way a comparison of Fig. 2.12 with Fig. 2.11 shows that the CPSWs can be closely approximated by the LG modes of an analogous apodized system.

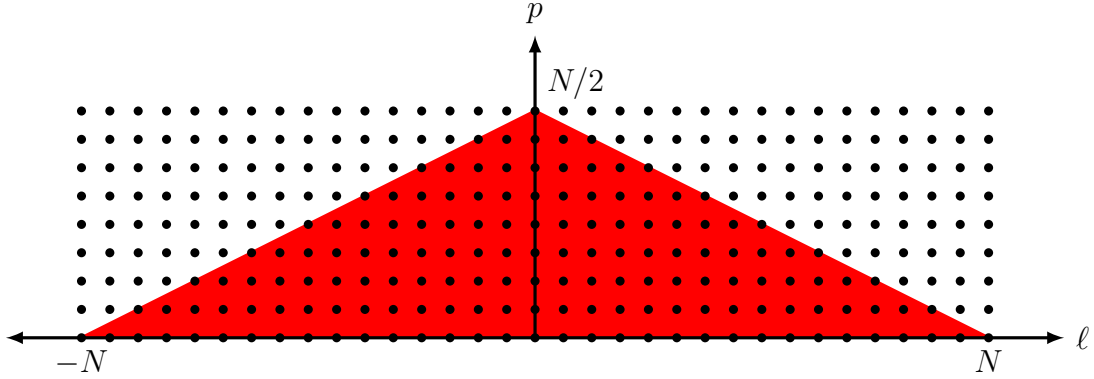


Figure 2.13: A configuration space diagram of CPSW communication modes. The red area indicates those states for which $2p + |\ell| \leq N$.

As was discussed in section 2.5.2, we expect the transmission efficiencies $\eta_{\ell,p}$ to be approximately equal to unity up to some sharp cutoff in the modal indices (ℓ, p) due to Abbe's model of diffraction between apertures. We know from section 2.5.1 that the maximum spatial frequencies of mode (ℓ, p) is related to the quantity $2p + |\ell|$, therefore we expect

$$\eta_{\ell,p} \approx \begin{cases} 1 & \text{for } 2p + |\ell| \leq N \\ 0 & \text{otherwise} \end{cases}, \quad (2.143)$$

where N is some number related to the total number of modes the communication system supports.

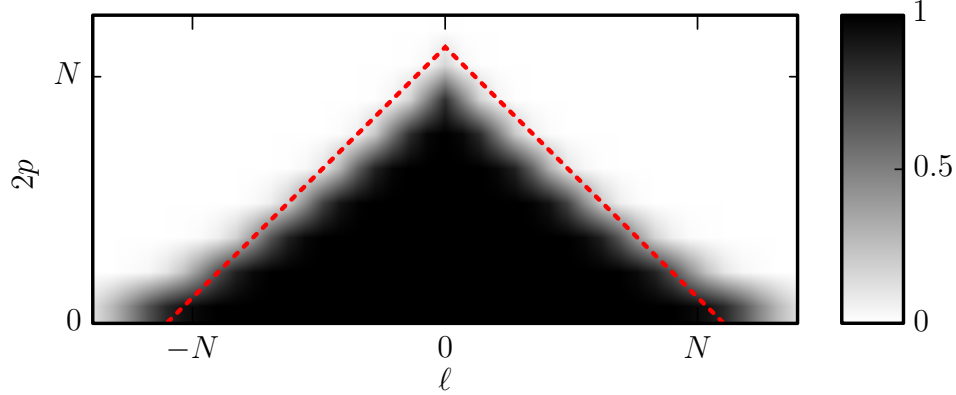


Figure 2.14: Plot of the transmission efficiencies $\eta_{\ell,p}$ for a free-space channel with hard apertures encoded using the circular prolate spheroidal communication modes of the channel. The efficiencies display a sharp cutoff for $2p + |\ell| > N$ which is represented by the dashed line.

The total number of modes such that Eq. (2.143) holds true is approximately D_F and thus

$$\begin{aligned}
 D_F &\approx \sum_{2p+|\ell|\leq N} 1 \\
 &= \sum_{p=0}^{N/2} \left(\sum_{\ell=-(N-2p)}^{N-2p} 1 \right) \\
 &= \sum_{p=0}^{N/2} (2(N-2p) + 1) \\
 &= \frac{1}{2}(N+1)(N+2),
 \end{aligned} \tag{2.144}$$

which is represented diagrammatically as the red region in Fig. 2.13. Inverting this equation gives

$$N = \frac{1}{2} \left(\sqrt{1 + 8D_F} - 3 \right) \approx \sqrt{2D_F}. \tag{2.145}$$

A two dimensional plot of $\eta_{\ell,p}$ is shown in Fig. 2.14 showing the accuracy of Eq. (2.143) (represented by the dashed line) compared with the actual numerically computed values.

2.7 Orbital angular momentum of light

The communication modes derived in section 2.6 are orbital angular momentum (OAM) eigenstates of light as will be demonstrated in this section. This is due to azimuthal dependence of the beam being described by the $e^{i\ell\phi}$ phase term. Such beams are sometimes known as vortex beams with topological charge equal to ℓ due to the fact that the phase is singular at $r = 0$ with a topological winding number of ℓ about the optical axis [32].

As the “vortex” name suggests, there is a rotation of the field that is responsible for the existence of angular momentum in the beam. This can be seen if one considers the wavefronts of the beam. The phase of a vortex beam has the form

$$\text{phase} \sim kz + \ell\phi, \quad (2.146)$$

which for surfaces of constant phase, will rotate about the optical axis with period λ/ℓ . A plot of the wavefronts of the states $\ell \in [-3, 3]$ are shown in Fig. 2.15 which clearly show the rotational nature of the wavefront of these beams.

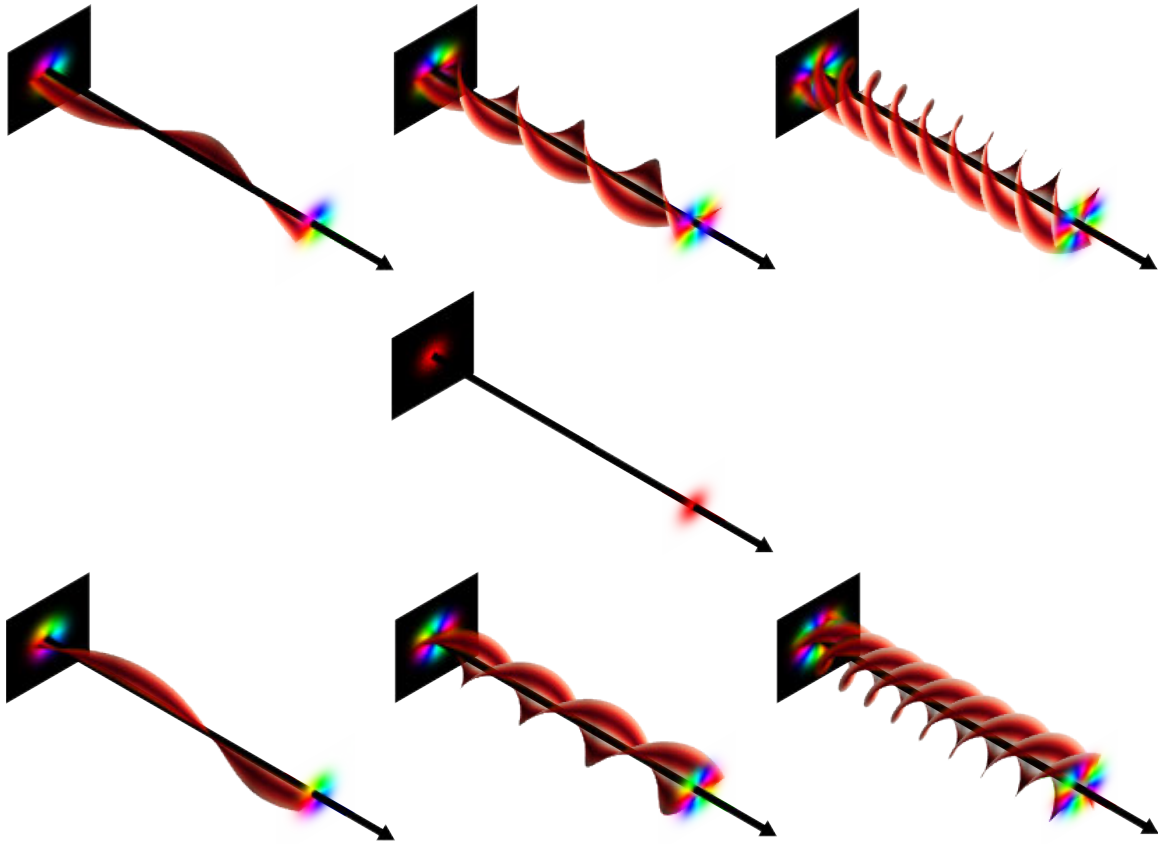


Figure 2.15: Plots of the seven lowest order Orbital angular momentum states of light. The top row shows states with negative topological OAM charge while the bottom row shows plots of states with negative charge. Two dimensional slices are presented at $z = 0$ and $z = \lambda$, while only the surface with phase equal to zero is shown between these two planes. Phase of the beams is represented by the color hue, while amplitude is represented by the color's brightness.

2.7.1 Rotational eigenmodes

In section 2.6 we made the ansatz that the azimuthal dependence of the communication modes of a system with circular apertures was completely described by the term $e^{il\phi}$. This is due to the fact that the system has cylindrical symmetry about the optical z

axis. To prove this, we define a rotation operator $\hat{R}(\Delta\phi)$ such that

$$\hat{R}(\Delta\phi) |f(\phi)\rangle = |f(\phi + \Delta\phi)\rangle. \quad (2.147)$$

By the symmetry of the Green's function of the system, we know that \hat{G} and \hat{R} commute. Therefore if we apply \hat{R} to the eigenequations of Eq. (2.7) that define the communication modes $|a_n\rangle$ and $|b_n\rangle$, we get

$$\begin{aligned} \hat{R}\hat{G}^\dagger\hat{G}|a_n\rangle &= \hat{G}^\dagger\hat{G}\hat{R}|a_n\rangle = |g_n|^2 \hat{R}|a_n\rangle \\ \hat{R}\hat{G}\hat{G}^\dagger|b_n\rangle &= \hat{G}\hat{G}^\dagger\hat{R}|a_n\rangle = |g_n|^2 \hat{R}|b_n\rangle. \end{aligned} \quad (2.148)$$

The states $\hat{R}|a_n\rangle$ and $\hat{R}|b_n\rangle$ are also communication modes with the same eigenvalues $|g_n|^2$. Therefore these states span a degenerate subspace which can be diagonalized by also requiring that the states $|a_n\rangle$ and $|b_n\rangle$ be eigenstates of \hat{R} .

The eigenstates of rotations are given by states of the form

$$\langle \mathbf{r} | \psi_\ell \rangle = f(r) e^{i\ell\phi}. \quad (2.149)$$

We can show that these states are the eigenstates and also find the eigenvalues by applying \hat{R} , e.g.

$$\hat{R}(\Delta\phi) |\psi_\ell\rangle = \int d\mathbf{r} |\mathbf{r}\rangle \langle \mathbf{r} | \hat{R}(\Delta\phi) | \psi_\ell \rangle = \int d\mathbf{r} |\mathbf{r}\rangle f(r) e^{i\ell(\phi+\Delta\phi)} = e^{i\ell\Delta\phi} |\psi_\ell\rangle, \quad (2.150)$$

which gives eigenvalues of $e^{i\ell\Delta\phi}$. The azimuthal angle ϕ is also periodic with period 2π and thus

$$\hat{R}(\Delta\phi = 2\pi) \equiv \hat{\mathbb{I}}, \quad (2.151)$$

where $\hat{\mathbb{I}}$ is the identity operator. We therefore require

$$\hat{R}(\Delta\phi = 2\pi) |\psi_\ell\rangle = e^{i\ell 2\pi} |\psi_\ell\rangle = |\psi_\ell\rangle, \quad (2.152)$$

which is true only for integer values of ℓ .

It is a well established fact in modern physics that for every symmetry governing the dynamics of a system there is a corresponding conserved physical quantity [33]. For cylindrically symmetric systems, we thus have a conserved “charge,” ℓ , which will be shown to be related to eigenstates of orbital angular momentum (OAM). This was first shown for the case of Laguerre-Gaussian beams [34], and was later demonstrated to hold in general (for both classical as well as quantum fields) [35].

2.7.2 Angular momentum of an optical field

For an optical field, the angular momentum flux density \mathbf{j} is given by

$$\mathbf{j} = \mathbf{r} \times \mathbf{p}, \quad (2.153)$$

where \mathbf{p} is the momentum flux density given by

$$\mathbf{p} = c\varepsilon_0 \langle \mathbf{E} \times \mathbf{B} \rangle. \quad (2.154)$$

Consider a monochromatic optical field given by the vector potential (assuming the Lorenz gauge)

$$\mathbf{A} = (a\hat{\mathbf{x}} + b\hat{\mathbf{y}})U(x, y, z)e^{ikz}, \quad (2.155)$$

where $(a\hat{\mathbf{x}} + b\hat{\mathbf{y}})$ specifies the polarization and $U(x, y, z)$ is the spatial mode. Assuming propagation within the paraxial approximation, the momentum flux density for such a field is given by [36]

$$\begin{aligned} \mathbf{p} &= \frac{c\varepsilon_0}{2} \left(i\omega(U\nabla U^* - U^*\nabla U) + 2\omega k|U|^2 \hat{\mathbf{z}} + i\omega(ab^* - a^*b)\nabla|U|^2 \times \hat{\mathbf{z}} \right) \\ &= \frac{c\varepsilon_0}{2} \left(\omega(iU\nabla U^* + c.c.) + 2\omega k|U|^2 \hat{\mathbf{z}} + \omega\sigma\nabla|U|^2 \times \hat{\mathbf{z}} \right), \end{aligned} \quad (2.156)$$

where $\sigma = i(ab^* - a^*b)$ is the spin-projection along $\hat{\mathbf{z}}$ ($\sigma = \pm 1$ for circularly polarized and $\sigma = 0$ for linearly polarized light).

If we assume that $U(x, y, z)$ is of the form

$$U(x, y, z) = u(\rho, z)e^{il\phi}, \quad (2.157)$$

where $\rho = \sqrt{x^2 + y^2}$, then Eq. (2.156) becomes

$$\mathbf{p} = \frac{c\varepsilon_0\omega}{2} \left(\left(iu(\hat{\boldsymbol{\rho}}\frac{\partial}{\partial\rho} + \hat{\mathbf{z}}\frac{\partial}{\partial z})u^* + c.c. \right) + 2k|u|^2\hat{\mathbf{z}} + \left(2\ell\frac{|u|^2}{\rho} - \sigma\frac{\partial|u|^2}{\partial\rho} \right) \hat{\boldsymbol{\phi}} \right). \quad (2.158)$$

Now the angular momentum flux density along the optical axis \mathbf{z} is

$$j_z = \mathbf{j} \cdot \hat{\mathbf{z}} = (\mathbf{r} \times \mathbf{p}) \cdot \hat{\mathbf{z}} = \boldsymbol{\rho} \times (p_\phi \hat{\boldsymbol{\phi}}) = c\varepsilon_0\omega |u|^2 \ell - \rho \frac{c\varepsilon_0\omega}{2} \frac{\partial |u|^2}{\partial \rho} \sigma, \quad (2.159)$$

while the energy flux density (e.g. time averaged Poynting vector) becomes

$$S_z = \mathbf{p} \cdot \hat{\mathbf{z}} = \frac{c^2\varepsilon_0\omega}{2} \left(\left(iu\frac{\partial}{\partial z}u^* + c.c. \right) + 2k|u|^2 \right) \approx c^2\varepsilon_0\omega k|u|^2 = c\varepsilon_0\omega^2|u|^2, \quad (2.160)$$

where we have used the paraxial approximation

$$k|u|^2 \gg \left| u\frac{\partial u^*}{\partial z} \right|. \quad (2.161)$$

The total angular momentum in any z plane normalized to the energy of the beam is given by the ratio of the angular momentum flux J_z and the energy flux Φ_z ,

$$\begin{aligned}
\frac{J_z}{\Phi_z} &= \frac{\iint \mathbf{j} \cdot \hat{\mathbf{z}} \rho \, d\rho \, d\phi}{\iint \mathbf{S} \cdot \hat{\mathbf{z}} \rho \, d\rho \, d\phi} \\
&= \frac{c\varepsilon_0\omega \iint d\rho \, d\phi \left(\rho\ell - \sigma\frac{\rho^2}{2}\frac{\partial}{\partial\rho}\right) |u|^2}{c\varepsilon_0\omega^2 \iint |u|^2 \rho \, d\rho \, d\phi} \\
&= \frac{(\ell + \sigma) \iint |u|^2 \rho \, d\rho \, d\phi}{\omega \iint |u|^2 \rho \, d\rho \, d\phi} \\
&= \frac{\ell + \sigma}{\omega}.
\end{aligned} \tag{2.162}$$

If a single photon is prepared in the state given by Eq. (2.155), then by the Planck-Einstein relation the energy of the photon will be $\hbar\omega$. If we write the angular momentum per unit energy $\hbar\omega$, we get

$$\frac{J_z}{\Phi_z} = \frac{\hbar(\ell + \sigma)}{\hbar\omega}. \tag{2.163}$$

Therefore the angular momentum per photon is given by

$$J_z = L + S = \hbar\ell + \hbar\sigma, \tag{2.164}$$

where $L = \hbar\ell$ is the OAM and $S = \hbar\sigma$ is the spin angular momentum.

Most systems in practice use cylindrical apertures, and therefore the communication modes of most systems will be eigenstates of OAM, i.e. will be states of definite value of L . For this reason, as well as technical details related to methods of mode

discrimination that will be discussed in section 3.2, much of the research that will be presented in the remainder of this thesis is concerned specifically with communication using beams within the one dimensional azimuthal spatial subspace of the transverse degree of freedom of an optical beam.

Chapter 3

Implementing spatial mode communication

In chapter 2 the fundamental limits due to diffraction of free-space optical communication systems were analyzed. This was done assuming ideal mode generation and measurement by Alice and Bob. However these tasks are not trivial. The generation and discrimination of modes must be accurate to minimize errors and fast if one cares about the overall communication rates.

This chapter concerns the details of an experimental implementation intended to demonstrate the possibility of a free-space, high-dimensional quantum key distribution system encoded using spatial modes of light. Section 3.1 describes methods of spatial light modulation using computer generated holograms for generation of arbitrary spatial fields of light, as well as technological methods that allow for rapid generation of modes. Section 3.2 details the basic problems of state discrimination as well as the

technological methods utilized for modal discrimination. Section 3.3 demonstrates the integration of the mode generation and discrimination in an integrated QKD system.

3.1 Spatial mode generation

One of the key technological tools used for controlling the traverse field of an optical beam is the spatial light modulator (SLM). An SLM can be described by a complex transmission function of an optical beam $T(x, y)$ that is a function of position on the device itself. A beam described by some complex field $U_I(x, y)$ incident on an SLM will then be given by

$$U(x, y) = T(x, y) \times U_I(x, y) \quad (3.1)$$

after interacting with the SLM (either after reflection from or transmission through the SLM). The properties of $T(x, y)$ are controllable experimentally, typically via individually addressable pixels whose properties can be controlled electronically via computer control.

If an SLM could generate an arbitrary complex value at each point it would be trivial to generate arbitrary spatial modes. Generation of any mode could be accomplished by shining a plane wave on the SLM and setting the SLM's transmission to be given by

$$T(x, y) = \frac{A(x, y)}{U_I} e^{i\phi(x, y)}, \quad (3.2)$$

where A and ϕ are the desired amplitude and phase of the generated spatial mode. Although historically there have been methods of generating such complex valued transmission functions [37], most SLMs do not generally have the ability to generate any transmission function, but instead are much more limited. Typically SLMs are either phase or amplitude only devices, and thus require more sophisticated modulation techniques for generating arbitrary beams.

Instead of trying to modulate the complex value of the desired optical beam directly, one can instead use the SLM to generate a computer generated hologram (CGH). If the CGH is periodic then the device will act as a diffraction device creating multiple orders in which the beam will scatter into. This is represented in the left panel of Fig. 3.1. If $T(x, y)$ is spatially periodic then we can write T as the Fourier expansion

$$T(x, y) = \sum_m T_m e^{im(\mathbf{G}\cdot\mathbf{r})}, \quad (3.3)$$

where

$$\mathbf{G} = (2\pi/\Lambda)(\cos(\theta)\hat{\mathbf{x}} + \sin(\theta)\hat{\mathbf{y}}) \quad (3.4)$$

is the grating wavevector representing a periodicity along the θ direction with period Λ , and T_m is the amplitude of the beam that is diffracted into the m th diffraction order given by

$$T_m = \frac{\iint_{\Lambda} T(x, y) e^{-im(\mathbf{G}\cdot\mathbf{r})} \, d\mathbf{r}}{\iint_{\Lambda} d\mathbf{r}} = \frac{1}{A} \iint_{\Lambda} T(x, y) e^{-im(\mathbf{G}\cdot\mathbf{r})} \, d\mathbf{r}, \quad (3.5)$$

where $A = \iint_{\Lambda} d\mathbf{r}$ is the area of a single period of the grating.

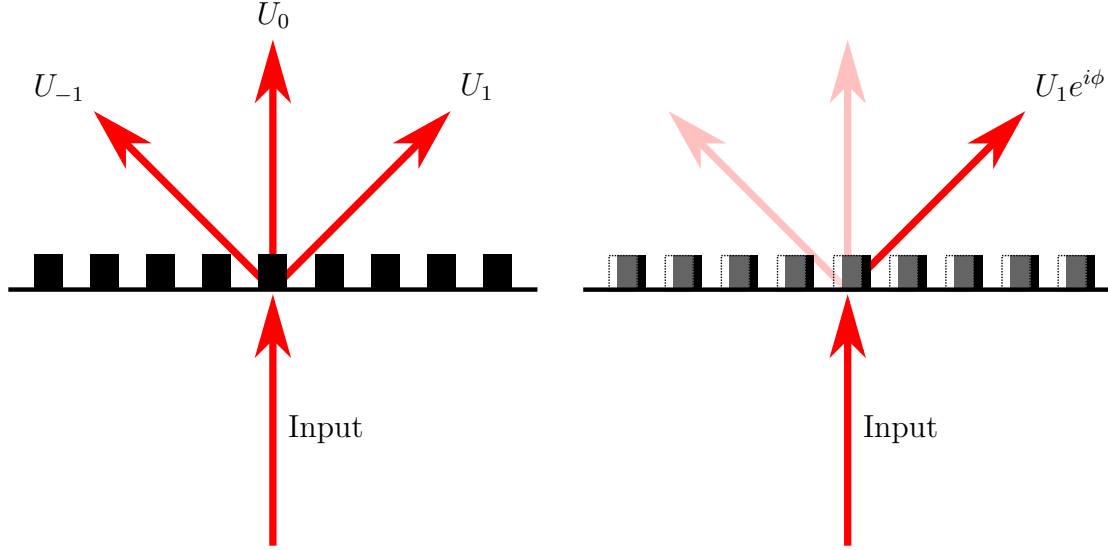


Figure 3.1: Left: a periodic structure acts as a diffraction grating that splits the beam up into multiple diffraction orders. Right: a phase change is induced in the diffracted order as a result of the detour phase caused by shifting the grating.

No matter what the physical origin of $T(x, y)$ that creates the diffraction grating, any phase can be induced in a diffracted beam by a simple shift in the grating's location along \mathbf{G} . This can be seen by applying the transformation $\mathbf{r} \rightarrow \mathbf{r} + \Delta\mathbf{r}$ to Eq. (3.3), i.e.

$$T(x, y) = \sum_m T_m e^{im(\mathbf{G} \cdot (\mathbf{r} + \Delta\mathbf{r}))} = \sum_m T_m e^{im(2\pi\delta)} e^{im(\mathbf{G} \cdot \mathbf{r})} = \sum_m T'_m e^{im(\mathbf{G} \cdot \mathbf{r})}, \quad (3.6)$$

where

$$2\pi\delta = \mathbf{G} \cdot \Delta\mathbf{r}, \quad (3.7)$$

and δ represents the shift relative to Λ of the grating. One generally has full control over the ability to shift the grating, and therefore the desired mode in the diffracted order can take on any phase. This type of phase modulation is known as a detour phase, due to the fact that the phase can be understood as being caused by a change in the optical path lengths as one shifts the grating which induces a detour in the beam path leading to the accumulation of additional phase [38].

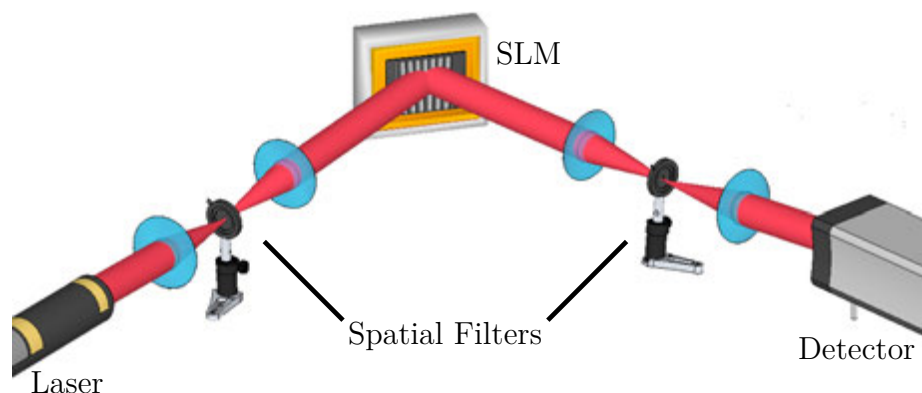


Figure 3.2: Basic setup for generating spatial modes with a modulated diffraction grating CGH on a SLM. A laser beam is spatially filtered before the SLM to create a simple collimated beam for U_I . Filtering is also required after the SLM to select a single modulated diffraction order.

If one then adds a modulation onto this periodic pattern, it is possible to have phase and amplitude control in the diffracted order. The basic setup for such a scheme is shown in Fig. 3.2. A laser is spatially filtered and shown onto an SLM. A CGH grating is encoded on the SLM device which create multiple diffraction orders which are filtered out in a Fourier plane after the device with a second spatial filter. In this schematic a detector is placed at the final output plane, allowing measurement of the intensity pattern of the generated field. If the beam at the SLM is a unit-amplitude

plane wave, then the output field in the first diffracted order is given by

$$U(x, y) = T_1(x, y)e^{i2\pi\delta(x, y)}, \quad (3.8)$$

where we have explicitly kept the detour phase term (which is now a function of position), and $T_1(x, y)$ is the local amplitude given by

$$T_1(x, y) = \frac{1}{A} \iint_{\Lambda(x, y)} T(x', y') e^{-i\mathbf{G}\cdot\mathbf{r}'} d\mathbf{r}' \quad (3.9)$$

The modulation of the grating must not contain spatial frequencies greater than \mathbf{G} or there will be mixing between the different diffraction orders.

3.1.1 Phase only spatial light modulation

The first type of SLM we consider is one in which only the phase is modulated. Such a device will have a transmission function

$$T(x, y) = e^{i\Psi(x, y)}, \quad (3.10)$$

where $\Psi(x, y)$ is the phase value at (x, y) . Suppose we want to create a beam

$$U(x, y) = A(x, y)e^{i\phi(x, y)}, \quad (3.11)$$

where A is the mode amplitude and ϕ is the desired phase. The simplest type of modulation is to assume a periodic function $\Phi(\phi)$ that encodes the desired phase information, and a modulation function $f(A)$ that modulates Φ as a function of the mode amplitude. In this case the SLM phase is given by

$$\Psi = f(A)\Phi(\phi). \quad (3.12)$$

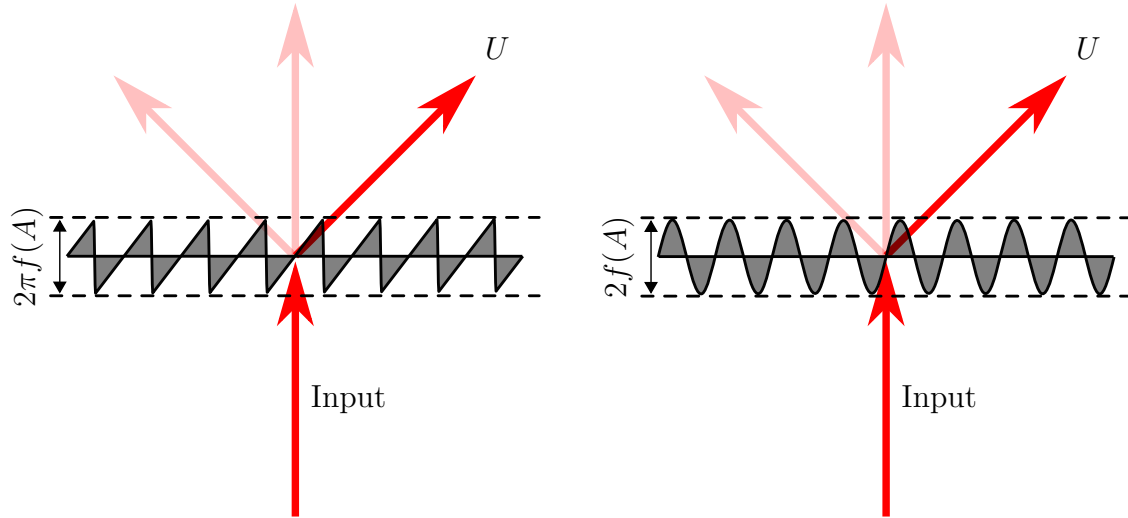


Figure 3.3: Two CGH encoding schemes for phase only SLMs. Left: schematic of a blazed grating encoding. Right: schematic of a sinusoidal grating.

The simplest form of Φ is simply a blazed grating [39], which is shown schematically in the left panel of Fig. 3.3. Such a grating has a phase function defined as

$$\Phi = (\mathbf{G} \cdot \mathbf{r} + \phi) \bmod 2\pi - \pi, \quad (3.13)$$

where $\Phi \in [-\pi, \pi]$ is defined symmetrically about zero to ensure amplitude modulation does not create additional phase modulation [40]. In this case the expansion into the m th order given by Eq. (3.5) becomes [41]

$$T_m = \frac{1}{A} \iint_{\Lambda} T(x, y) e^{-im(\mathbf{G} \cdot \mathbf{r})} d\mathbf{r} = \int_{-\pi}^{\pi} e^{if(A)\Phi} e^{-im\Phi} d\Phi = \text{sinc}(m - f(A)). \quad (3.14)$$

Therefore $f(A)$ is computed from the inverse of

$$T_1(A) = \text{sinc}(1 - f(A)) = A. \quad (3.15)$$

A second form of Φ is a sinusoidal grating [41], which is shown schematically in the right panel of Fig. 3.3. The phase function of a sinusoidal grating is defined as

$$\Phi = \sin(\mathbf{G} \cdot \mathbf{r} + \phi). \quad (3.16)$$

We can expand T in terms of Bessel functions using the Jacobi-Anger expansion

$$e^{if(A)\sin(\Phi)} = \sum_{m=-\infty}^{\infty} e^{im\Phi} J_m(f(A)), \quad (3.17)$$

which is derived by the substitution $t = \exp(i\Phi)$ and $z = f(A)$ into the generating sequence defining the Bessel functions [27]

$$e^{\frac{1}{2}(t-1/t)z} = \sum_{m=-\infty}^{\infty} t^m J_m(z). \quad (3.18)$$

Therefore the amplitude into the m th order is

$$T_m(A) = J_m(f(A)), \quad (3.19)$$

and $f(A)$ is found by the finding the inverse of

$$T_1(A) = J_1(f(A)) = A. \quad (3.20)$$

It should be noted that the maximum value of A which allows $J_1^{-1}(A)$ to be single valued is $A \approx 0.58$, corresponding to the first maximum of $J_1(x)$ at $x \approx 1.8$. Therefore $A \in [0, 0.58]$ and $f(A) \in [0, 1.8]$, which gives a phase range of $\Phi \in [-1.8, 1.8]$. This is in contrast to the blazed grating encoding that gives a phase range of $\Phi \in [-\pi, \pi]$ and a maximum amplitude of $A_{\max} = 1$.

Sample holograms using phase only modulation are shown in Fig. 3.4. Sample modes are shown for a LG_0^2 Laguerre-Gaussian mode, as well as a pure $\ell = 2$ vortex beam. Holograms encoded using both a blazed grating and sinusoidal grating are shown for each mode. A notable feature in these holograms is a forked pattern in the

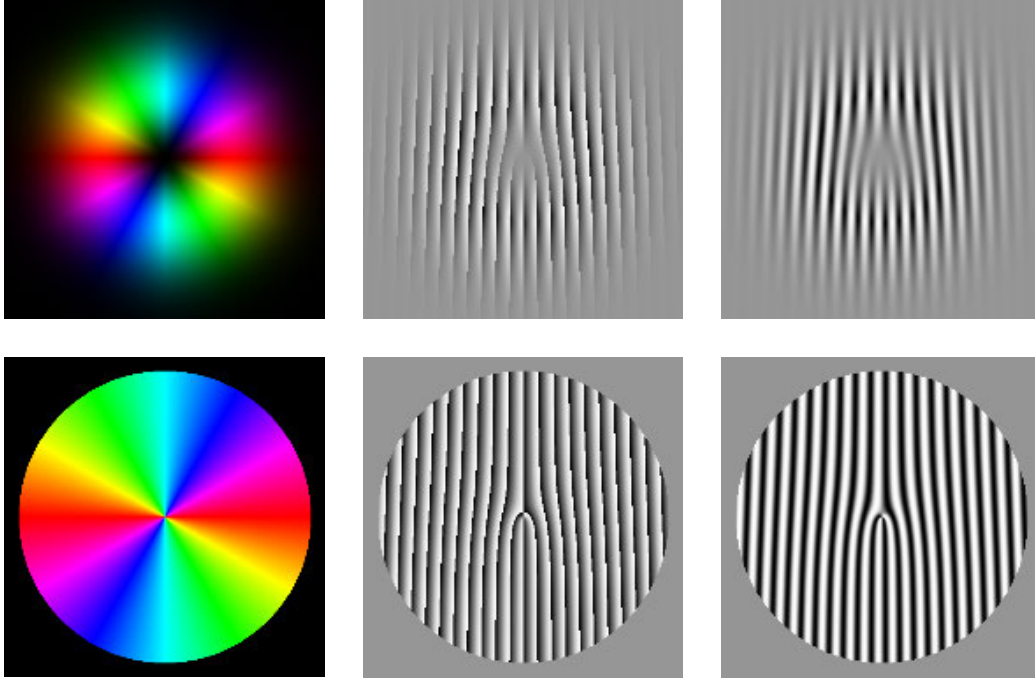


Figure 3.4: Phase only holograms necessary to create a LG_0^2 mode (top) and a pure $\ell = 2$ vortex beam (bottom). Left: complex plots of the desired mode $U(x, y)$. Middle: hologram generated using a blazed grating. Right: hologram generated using a sinusoidal grating.

center of the hologram. This is due to the topological charge of the OAM in these beams, i.e. if one draws a closed loop around the fork and counts the number of periods, one will find it adds up to exactly ℓ .

3.1.2 Binary spatial light modulation

The second type of grating we consider is a binary grating. The grating shown in Fig. 3.1 was a binary grating. A close up of this type of encoding showing a single period is given in Fig. 3.5. There are two regions with distinct values for the SLM transmission T . The background or zero region denoted by a transmission t_0 and a

binary square pulse of width $q\Lambda$ given by a transmission of t_1 . Therefore within a single grating period, $x \in [-\Lambda/2, \Lambda/2]$, the transmission is given by

$$T(x) = t_0 \left(1 - \text{rect} \left(\frac{x}{q\Lambda} \right) \right) + t_1 \text{rect} \left(\frac{x}{q\Lambda} \right). \quad (3.21)$$

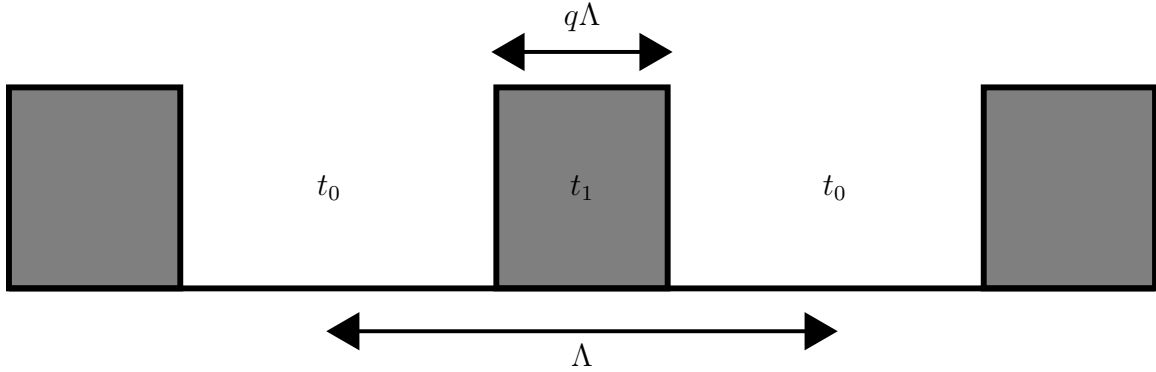


Figure 3.5: Plot of a binary diffraction grating with period Λ and square pulses of width $q\Lambda$. The transmission function of the pulses is given by t_1 , while the background is t_0 .

The transmission amplitude of the m th diffraction order from a binary equation as given by Eq. (3.5) is

$$\begin{aligned} T_m &= \frac{t_1 - t_0}{\Lambda} \int \text{rect} \left(\frac{x}{q\Lambda} \right) e^{-im2\pi x/\Lambda} dx + \frac{t_0}{\Lambda} \int \text{rect} \left(\frac{x}{\Lambda} \right) e^{-im2\pi x/\Lambda} dx \\ &= (t_1 - t_0) q \text{sinc}(mq) + t_0 \text{sinc}(m). \end{aligned} \quad (3.22)$$

Therefore the first diffraction order is given by

$$T_1 = (t_1 - t_0) q \text{sinc}(q) = \frac{t_1 - t_0}{\pi} \sin(\pi q). \quad (3.23)$$

The phase of $(t_1 - t_0)$ creates a global phase factor that we can ignore and thus the field U in the first diffracted order can be written as

$$U = U_{\text{in}} \frac{|t_1 - t_0| \sin(\pi q)}{\pi} e^{i2\pi\delta}, \quad (3.24)$$

where δ is the shift in the grating responsible for the detour phase and $\delta = 0$ is chosen to cancel the phase of $t_1 - t_0$.

We can allow q and δ to vary with position \mathbf{r} , and the previous results still hold as long as $\delta(\mathbf{r}) \in [-1/2, 1/2]$ and $q(\mathbf{r})$ vary slower than the grating period Λ . Therefore we can create any field

$$U = A(\mathbf{r})e^{i\phi(\mathbf{r})}, \quad (3.25)$$

using the formula

$$q(\mathbf{r}) = \frac{1}{\pi} \arcsin \left(\frac{\pi A(\mathbf{r})}{|t_1 - t_0| U_{\text{in}}} \right), \quad \delta(\mathbf{r}) = \frac{\phi(\mathbf{r})}{2\pi}. \quad (3.26)$$

Thus, a shift in the location of the binary pulses changes the overall phases into the diffracted order, while changing the widths or duty cycles of the pulses changes the diffracted efficiency. These two methods are known as pulse position and pulse width modulation respectively [42, 43]. It should be noted that the maximum amplitude is given by

$$A_{\text{max}} = \frac{|t_1 - t_0|}{\pi} U_{\text{in}}, \quad (3.27)$$

which can always be compensated for by an increase of the amplitude of the input beam U_{in} .

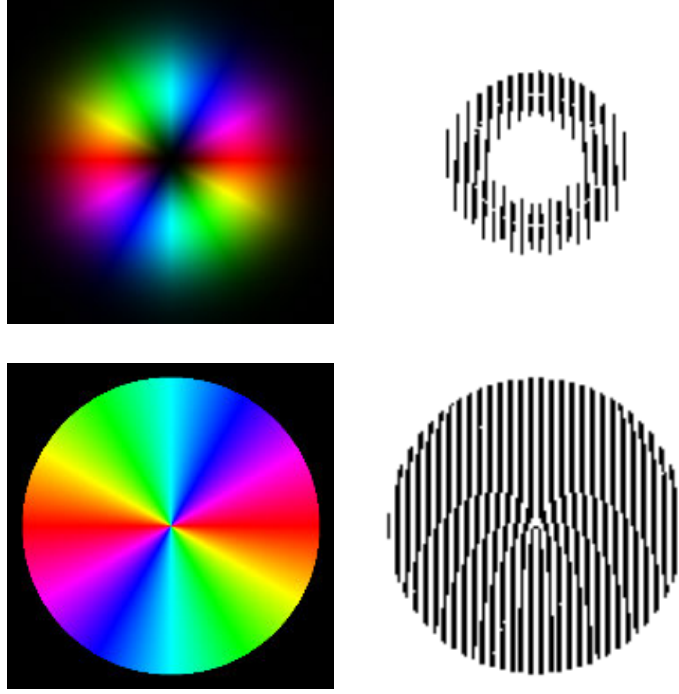


Figure 3.6: Binary holograms necessary to create a LG_0^2 mode (top) and a pure $\ell = 2$ vortex beam (bottom).

This full procedure can be represented in the following fashion. First one chooses the field $U = A(\mathbf{r})e^{i\phi(\mathbf{r})}$ that one wishes to create. Then $q(\mathbf{r})$ and $\delta(\mathbf{r})$ are computed from Eq. (3.26) and a periodic sinusoidal function is computed to give

$$\cos(\mathbf{G} \cdot \mathbf{r} + 2\pi\delta(\mathbf{r})). \quad (3.28)$$

To convert this into a binary hologram, this function is thresholded by $\cos(\pi q(\mathbf{r}))$ to create a binary pulse train with local pulse width $q(\mathbf{r})$. This can be written in the

compact form

$$f(\mathbf{r}) = H \left[\cos(\mathbf{G} \cdot \mathbf{r} + 2\pi\delta(\mathbf{r})) - \cos(\pi q(\mathbf{r})) \right], \quad (3.29)$$

where $H(z)$ is the Heaviside step function defined as

$$H(z) \equiv \begin{cases} 0 & \text{if } z < 0 \\ 1 & \text{if } z \geq 0 \end{cases}. \quad (3.30)$$

Plots of two binary CGHs generated using this technique are shown in Fig. 3.6 for a Laguerre-Gaussian and a pure vortex beam. Again we see a forked pattern just as we did in Fig. 3.4 indicating the presence of the topological charge of the OAM.

3.1.3 Rapid generation of spatial modes

Most SLMs are relatively slow and operate at frequencies of at most around a few tens of Hertz. One exception is the digital micromirror device (DMD) which can operate at up to a few tens of kilohertz. The DMD is a type of micro-electronic mechanical system, commonly known as a MEMS, that can function as a binary amplitude only SLM [44]. The device consists of a two dimensional pixelated array of micromirrors each mounted on an individually addressed MEMS that can be in one of two positions. In order to use the device as a SLM, the device is aligned such that the light is reflected and collected by the optics after the DMD if the micromirrors are in the on position, but scattered out of the system if the mirrors are in the off position. Thus the transmissions of the pulse and background are $t_1 = 1$ and $t_0 = 0$ respectively.

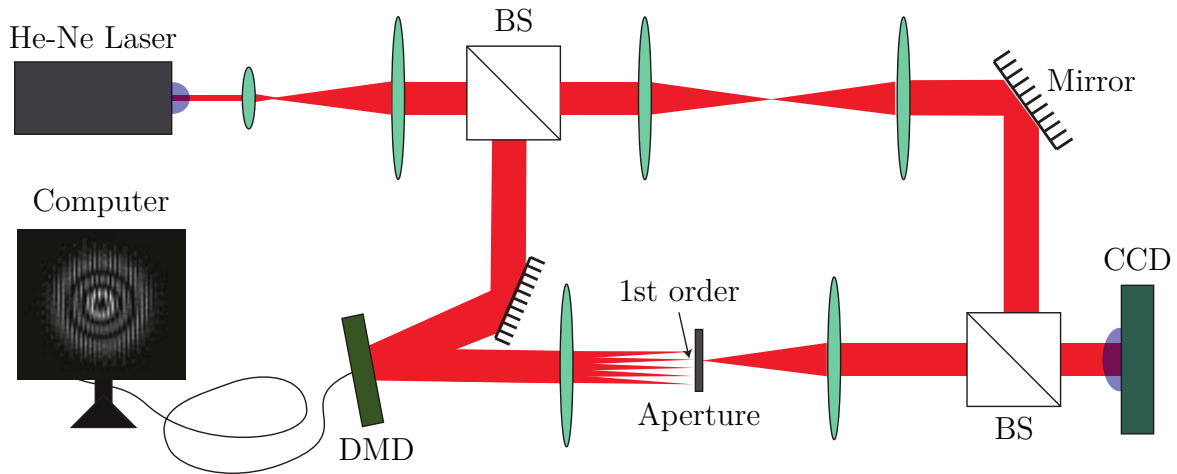


Figure 3.7: Schematic of setup to measure the quality of modes generated by a binary amplitude CGH on a DMD.

We demonstrated that DMDs are able to rapidly generate high quality spatial modes experimentally [1]. This was done in two steps, the first of which is to show that the binary CGHs on the DMD can generate quality spatial modes. The second step was to demonstrate fast switching is possible between coherent modes. The device used in our experiments was a Texas Instrument DLP3000. This device has a display resolution of 608×684 pixels, a micromirror size of $7.5 \mu\text{m}$, and the pixels can be switched at rates up to 4 KHz (i.e. the maximum refresh rate of the DLP3000).

In order to test the quality of the modal generation, the beams were imaged to verify the quality of the amplitude modulation. In addition images were taken of interferograms of the modes interfered with a collimated beam to observe the quality of the phase structure of the generated modes. A schematic of the experimental setup for this test is shown in Fig. 3.7. A laser beam is spatially filtered and collimated and split by a beam splitter into two beams. One of the two beams is modulated to

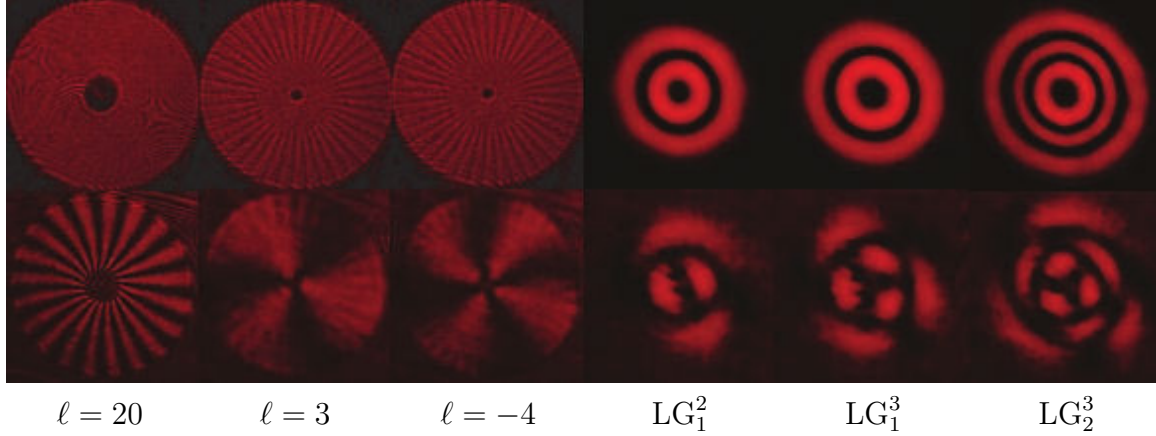


Figure 3.8: Intensity images (top) and interferograms (bottom) of a set of generated modes. The left three columns are vortex beams with OAM charge ℓ and the right three columns are LG_p^ℓ modes.

create a spatial mode as described in section 3.1.2. This beam is then recombined with the second beam at a CCD to generate the interferograms. The procedure to directly image the generated mode was identical as for the interferogram except with the reference arm blocked.

The images and interferograms of the generated modes are shown in Fig. 3.8. Included are three LG and 3 pure vortex beams. The images of the LG modes emphasize the quality of the amplitude modulation. The vortex beams are beams that include only phase modulation, and even with the relatively low resolution of our device shows quality modulation up to a topological charge of $\ell = 20$.

The second part of the experiment was to demonstrate that the generation and switching between modes could be done rapidly. This was done by cycling through the generation of three vortex modes with charge $\ell = \pm 5$ and $\ell = 0$ at the full 4 KHz rate of the DMD device and measuring the power in each mode as a function of

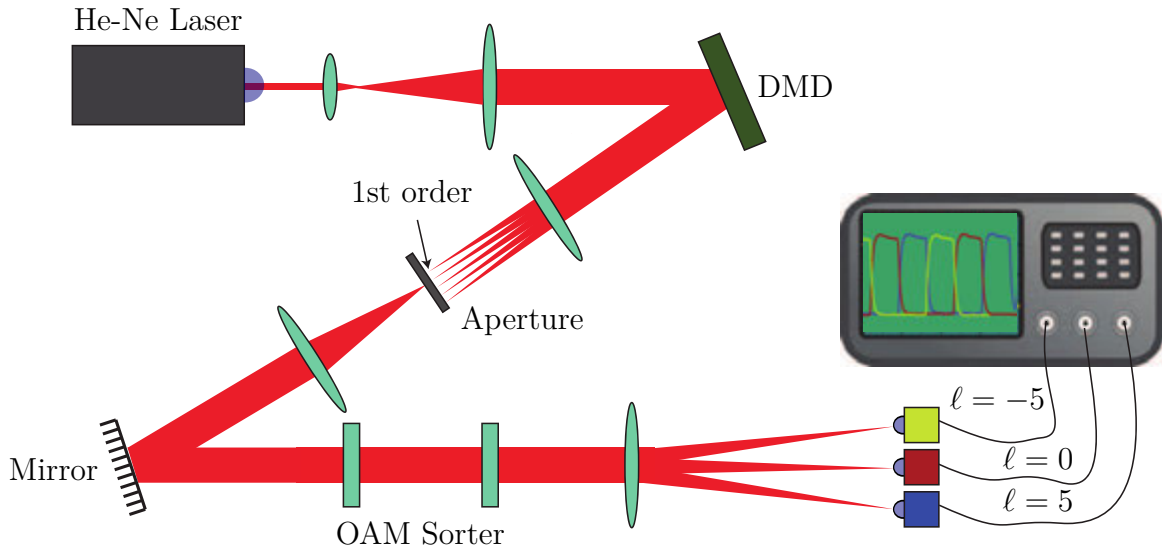


Figure 3.9: Schematic of the setup used to temporally resolve the power in three distinct OAM modes which are switched at 4 KHz. The modes used had OAM charge $\ell = -5$, $\ell = 5$, and $\ell = 0$.

time. A schematic of the setup used is shown in Fig. 3.9. The generated modes were separated into three output spots using the OAM mode sorter that will be described in section 3.2. At the location of each OAM output was placed a PIN photodiode connected to an oscilloscope.

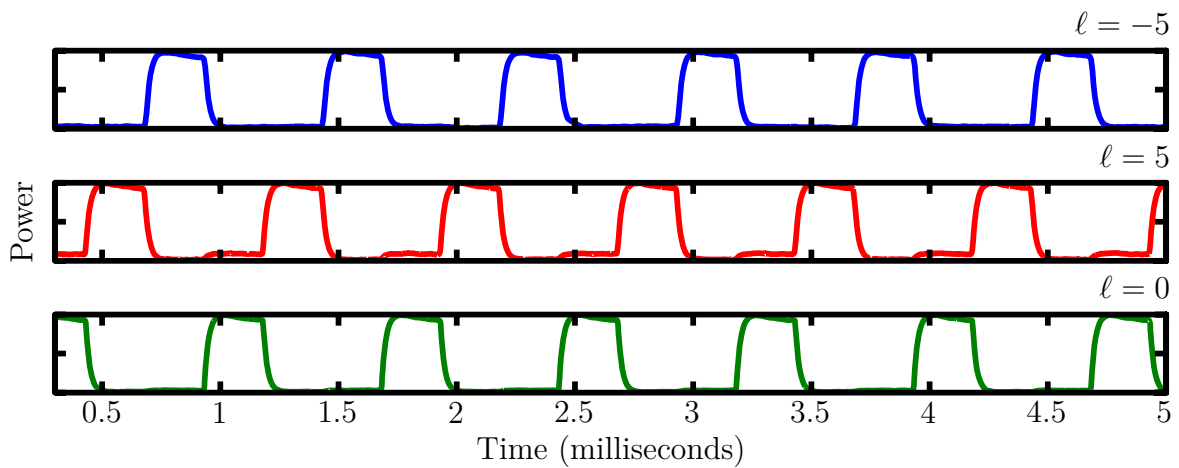


Figure 3.10: Oscilloscope time traces of three distinct OAM modes switched at 4 KHz.

The results of this experiment are shown in Fig. 3.10. Plotted are the three output channels showing the power in each spatial mode as a function of time. The switching can be seen to be both fast and stable. These results present a clear demonstration of the ability to generate and rapidly switch between spatial modes using this method.

3.1.4 Generation of modes with arbitrary spatial coherence

We showed that rapid switching of coherent modes demonstrated in section 3.1.3 can also be used to generate any arbitrary quasi-monochromatic partially coherent field that can be specified by a cross-spectral density function $W(\mathbf{r}_1, \mathbf{r}_2)$, i.e. for fields fully specified by their two point spatial correlations [2]. This is done by first computing the coherent mode decomposition of $W(\mathbf{r}_1, \mathbf{r}_2)$, which is an incoherent mixture of orthogonal coherent modes. For each of these coherent modes a CGH is computed and rapidly generated with a DMD. If the DMD switches between coherent modes on a timescale slower than the coherence time of the source laser, but long relative to the detection time of the CCD then the resultant field will create the coherent mode decomposition of the desired field.

Coherent mode decomposition

The transverse wavefront of a deterministic and coherent scalar beam is described by a complex field, $U(\mathbf{r})$. For a stochastic beam, $U(\mathbf{r})$ is a random variable and it becomes necessary to represent the field in a more sophisticated way. The standard

way of doing this is with the cross-spectral density function. At a single frequency the cross-spectral density function is defined as

$$W(\mathbf{r}_1, \mathbf{r}_2) = \langle U^*(\mathbf{r}_1)U(\mathbf{r}_2) \rangle, \quad (3.31)$$

and represents the average intensity

$$\langle I(\mathbf{r}) \rangle \equiv W(\mathbf{r}, \mathbf{r}), \quad (3.32)$$

as well as the correlations (up to second order) of such a partially coherent field [45].

$W(\mathbf{r}_1, \mathbf{r}_2)$ can be decomposed into an incoherent sum of orthogonal spatial modes $\psi_n(\mathbf{r})$, written as

$$W(\mathbf{r}_1, \mathbf{r}_2) = \sum_n \lambda_n \psi_n^*(\mathbf{r}_1) \psi_n(\mathbf{r}_2), \quad (3.33)$$

where λ_n are real and nonnegative, and

$$p_n = \frac{\lambda_n}{\sum_n \lambda_n} \quad (3.34)$$

is the relative weight of the field in mode $\psi_n(\mathbf{r})$ [46]. The modes $\psi_n(\mathbf{r})$ can be computed as the eigenfunctions with corresponding eigenvalues λ_n from the Fredholm integral equation

$$\int W(\mathbf{r}_1, \mathbf{r}_2) \psi_n(\mathbf{r}_1) d^2\mathbf{r}_1 = \lambda_n \psi_n(\mathbf{r}_2). \quad (3.35)$$

This representation is often referred to as a coherent mode decomposition of $W(\mathbf{r}_1, \mathbf{r}_2)$. Mathematically Eq. (3.33) is a sum over an infinite number of modes, but in practice n is bounded by the maximum spatial frequency content of $W(\mathbf{r}_1, \mathbf{r}_2)$, i.e. there is some maximum

$$n_{max} = N \quad (3.36)$$

such that

$$p_n \approx 0, \quad \text{for } n > N. \quad (3.37)$$

For example, Gaussian Schell-model beams are a common example of a partially coherent beam. Such a beam is defined by having a Gaussian intensity

$$I(\mathbf{r}) = \exp(-r^2/2\sigma_I^2), \quad (3.38)$$

as well as a Gaussian degree of coherence

$$\mu(\mathbf{r}_1, \mathbf{r}_2) = \exp(-|\mathbf{r}_1 - \mathbf{r}_2|^2/2\sigma_\mu^2), \quad (3.39)$$

which gives a cross-spectral density function

$$W(\mathbf{r}_1, \mathbf{r}_2) = \sqrt{I(\mathbf{r}_1)I(\mathbf{r}_2)}\mu(\mathbf{r}_1, \mathbf{r}_2). \quad (3.40)$$

A coherent mode decomposition of such a Gaussian Schell-model beam shows that the number of coherent modes necessary to describe Eq. (3.40) is given by the number of independent coherent regions within the beam which is quantified by [47]

$$N \approx (\sigma_\mu / \sigma_I)^2. \quad (3.41)$$

Physically Eq. (3.33) can be realized if one can create a beam that alternates between the coherent modes $\psi_n(\mathbf{r})$ in time with relative frequency weighted by p_n . For measurement to yield the intended field, the switching time τ_s must be much faster than any detector integration time τ_{det} in order to create the intended averaging over the inputs. In addition, for the mixture to be an incoherent mixture, the various modes must not have any correlations in time. Thus the switching time must be slower than the coherence time τ_{coh} of the source. Together these form the condition

$$\tau_{\text{det}} > \tau_s > \tau_{\text{coh}}. \quad (3.42)$$

If Eq. (3.42) is met, then one has a physically realized implementation of $W(\mathbf{r}_1, \mathbf{r}_2)$.

Experiment

A schematic of the experimental setup used to demonstrate the generation of arbitrary $W(\mathbf{r}_1, \mathbf{r}_2)$ is shown in Fig. 3.2. A HeNe laser is spatially filtered using a 4f system to provide an initial coherent plane wave incident on the DMD. The various coherent

modes, ψ_n , are created in rapid succession using the methods described in the previous sections and are imaged onto a CCD. The CCD operates at 60 Hz, thus the detector integration time is

$$\tau_{\text{det}} = 1/60 \text{ Hz} \approx 17 \text{ ms.} \quad (3.43)$$

The DLP3000 DMD used in this experiment has a switching rate of 4 KHz, thus

$$\tau_s = 1/4 \text{ kHz} = 250 \text{ } \mu\text{s} \ll \tau_{\text{det}}, \quad (3.44)$$

which fulfills the first inequality in Eq. (3.42). The bandwidth of the HeNe is 1.5 GHz which gives

$$\tau_{\text{coh}} = 1/1.5 \text{ GHz} \approx 0.7 \text{ ns} \ll \tau_s \quad (3.45)$$

which meets the second part of the inequality in Eq. (3.42).

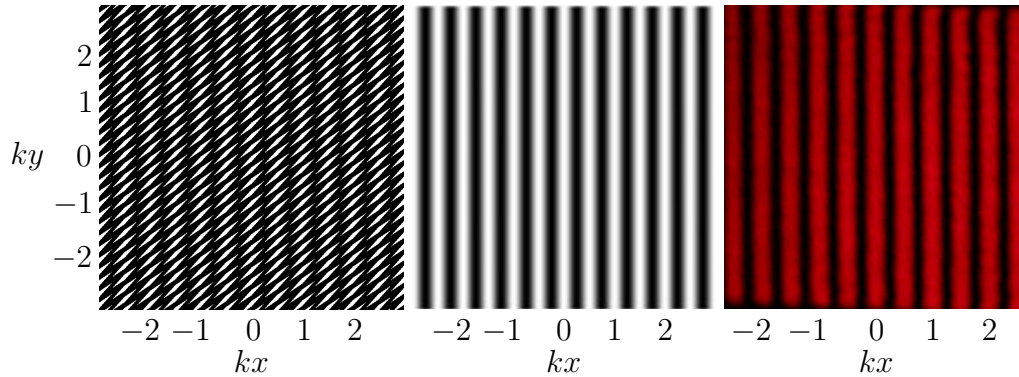


Figure 3.11: Interference fringes formed from the coherent superposition of two plane waves. Left figure shows the CGH used to generate the desired mode. Middle figure represents the target image while the right figure is an experimental image of the generated mode.

As a demonstration of the ability to generate a single coherent state, the field

$$U(\mathbf{r}) \propto e^{ikx} + e^{-ikx} \quad (3.46)$$

was generated. This represents a coherent superposition of two plane wave states, which form a sinusoidal interference pattern as shown in Fig 3.11.

For this experiment the mode was generated using a grating with wavevector

$$\mathbf{G} = \frac{2\pi}{25 \text{ px}}(\hat{\mathbf{x}} + \hat{\mathbf{y}}), \quad (3.47)$$

which represents a period of

$$T = 25\sqrt{2} \text{ pixels} \approx 275 \text{ } \mu\text{m} \quad (3.48)$$

oriented at $\theta = 45^\circ$. This value of \mathbf{G} was chosen to be large enough to allow enough separation in the Fourier plane to allow for filtering of the 1st diffracted order with an iris. In addition a nonzero value was chosen for both the x and y components of \mathbf{G} in order to minimize the noise by ensuring that the diffracted order did not overlap with any specular reflection due to the DMD's imperfect pixel fill-fraction. The underlying grating can be seen in the left image in Fig. 3.11 which have the appearance of the small diagonally oriented slivers. The plane wave transverse wavenumber was chosen

to be

$$k = \frac{2\pi}{100 \text{ px}} \approx \frac{2\pi}{780 \text{ }\mu\text{m}}. \quad (3.49)$$

Now the spatial wavenumber k meets the condition

$$k \ll |\mathbf{G}| \quad (3.50)$$

and thus is slowly varying enough to allow us to use the procedure in section 3.1.2 to construct the CGH to create this state. Since we are perfectly interfering 2 plane waves, the intensity varies as

$$I \propto \cos^2(kx). \quad (3.51)$$

Therefore the grating parameters q and δ are given by

$$q(\mathbf{r}) = \frac{1}{\pi} \arcsin(\cos(kx)) \quad \text{and} \quad \delta(\mathbf{r}) = 0. \quad (3.52)$$

Next we created a superposition of the plane waves $U_A = e^{ikx}$ and $U_B = e^{-ikx}$ as before, but this time the degree of coherence between the two beams was spatially varied, creating a partially coherent mix of modes. The coherent modes used to represent this is given by

$$\begin{aligned} \psi_1(\mathbf{r}) &\propto (U_A + f(\mathbf{r})U_B) \\ \psi_2(\mathbf{r}) &\propto (f(\mathbf{r})U_A + U_B), \end{aligned} \quad (3.53)$$

where the relative probability weightings are given as

$$p_1 = p_2 = 1/2, \quad (3.54)$$

and where $f(\mathbf{r})$ is related to the fringe visibility $V(\mathbf{r})$ by

$$f(\mathbf{r}) = V(\mathbf{r})/(1 + \sqrt{1 - V(\mathbf{r})^2}) = (1 - \sqrt{1 - V(\mathbf{r})^2})/V(\mathbf{r}). \quad (3.55)$$

The intensity for this beam is

$$I(\mathbf{r}) \propto (1 - f)^2 + 4f \cos^2(kx), \quad (3.56)$$

which is the sum of an incoherent and a coherent term which can be continuously tuned from fully coherent ($f = 1$) to incoherent ($f = 0$).

The visibility function chosen for the experiment is given by

$$V(\mathbf{r}) = |\sin(\kappa r)|, \quad (3.57)$$

where

$$2\pi\kappa = \frac{4k}{3} = \frac{2\pi}{75 \text{ px}} \approx \frac{2\pi}{580 \text{ }\mu\text{m}}. \quad (3.58)$$

Since $f(\mathbf{r})$ was chosen to be real, Eq. (3.57) also represents our spectral degree of coherence at \mathbf{r} . The CGHs necessary to create the modes ψ_1 and ψ_2 (Eq. (3.53)) for

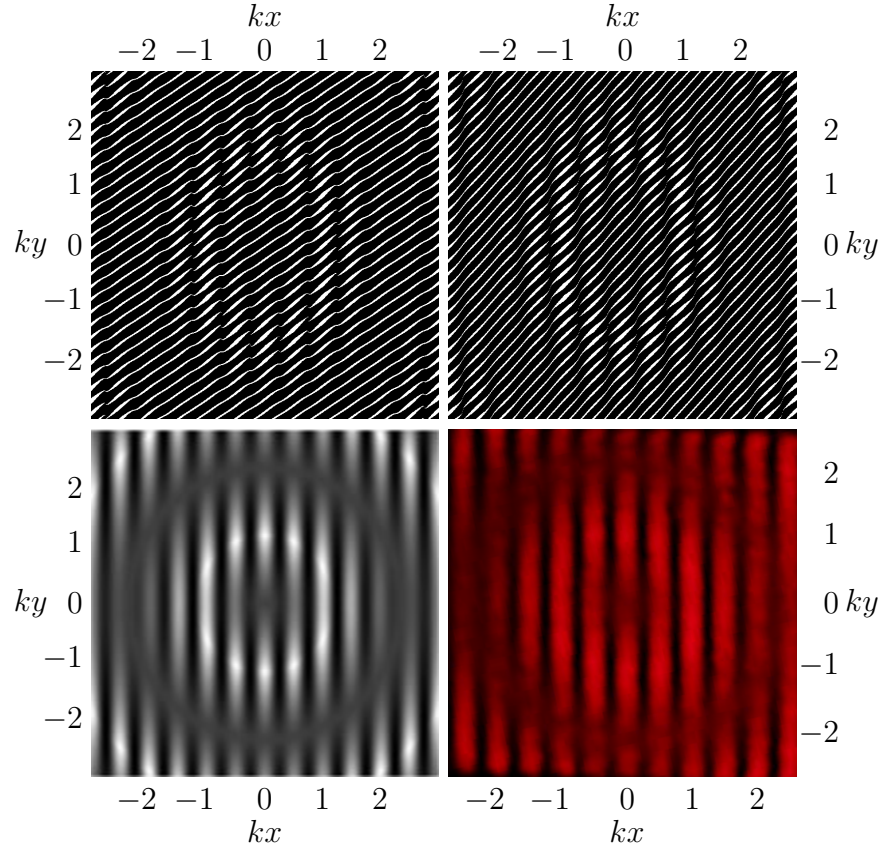


Figure 3.12: Interference fringes formed from superposition of two plane waves that are partially coherent with respect to each other. Top figures show the CGHs used to generate the desired modes given by Eq. 3.55. Bottom left figure represents the target intensity pattern, while the bottom right figure is an experimental image of the generated field.

this spatially varying fringe visibility are shown in the top row of Fig. 3.12. The CGH

parameters are

$$q(\mathbf{r}) = \frac{1}{\pi} \arcsin \left(\frac{\sqrt{4f \cos^2(kx) + (1-f)^2}}{I_{\max}} \right), \quad (3.59)$$

where I_{\max} is the maximum value of $I(\mathbf{r})$ and

$$\begin{aligned}\delta_{1,2}(\mathbf{r}) &= \arg(\Re(\psi_{1,2}) + i\Im(\psi_{1,2})) \\ &= \arg((2 \cos(kx) - (1 - f) \cos(kx)) \\ &\quad \mp i((f - 1) \sin(kx))).\end{aligned}\tag{3.60}$$

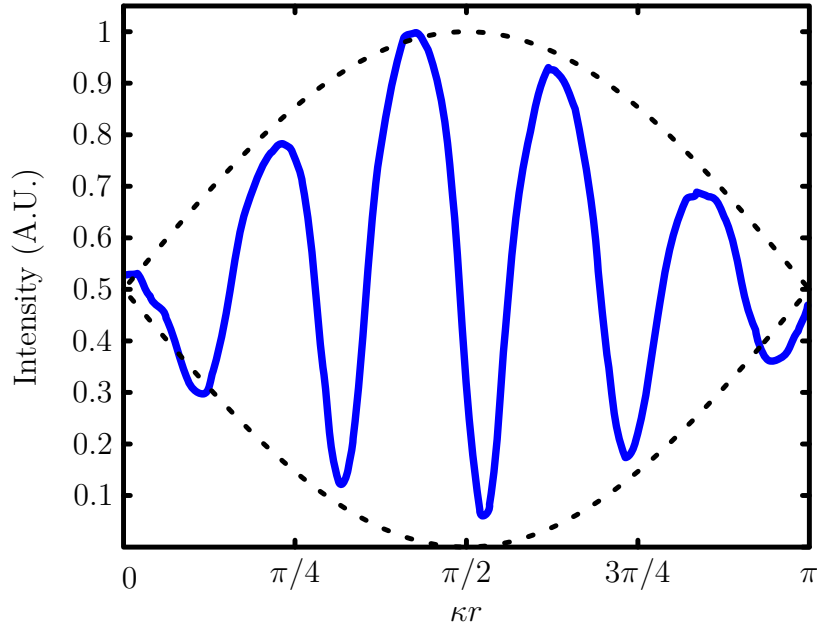


Figure 3.13: Plot of the intensity of the image in Fig. 3.12 along the 1D slice of r for $\theta = 0$, i.e. along the x -axis (solid blue line). Also shown as the black dotted line is the theoretical envelope of the maximum and minimum intensities based on the intended visibility function $V(\mathbf{r})$.

In order to compare the intended visibility given by Eq. (3.57) with the image shown in Fig. 3.12, a one dimensional slice of the intensity is plotted in Fig. 3.13. This slice is a radial slice r along the x axis (i.e. at an orientation of $\theta = 0$), and is plotted over an entire period of $\sin(\kappa r)$ of the visibility. In addition the theoretical envelope

of the visibility equal to

$$\frac{1 \pm V(\mathbf{r})}{2} = \frac{1 \pm |\sin(\kappa r)|}{2} \quad (3.61)$$

is plotted for comparison. As can be seen in both the original coherent and partially coherent cases, the intended and measured patterns are in excellent agreement with one another.

3.2 Spatial mode detection and discrimination

It is necessary to be able to measure and discriminate between spatial modes in order to successfully be able to use these modes, such as in a communication scheme. The most straightforward method for measuring a state is by a projection measurement as describe in chapter 1. The standard scheme used to implement such measurements for spatial modes will be discussed in this section, along with the problems with such an approach as a tool for communication. In addition a measurement technology more appropriate for communication, based on the efficient separation or sorting of OAM modes will be discussed.

3.2.1 Projection measurements of spatial modes

Suppose one has an input state given by U_0 and one wants to know if the state is in mode ψ_n , or similarly one wants to find the overlap of the two modes,

$$|\langle \psi_n | U_0 \rangle|^2 = |a_n|^2. \tag{3.62}$$

Such a measurement is known as a projection measurement. The standard method for projection measurements of spatial modes is based on a Fourier filtering approach which is shown diagrammatically in Fig. 3.14 [48], which is a complex generalization of the traditional matched filtering schemes [20].

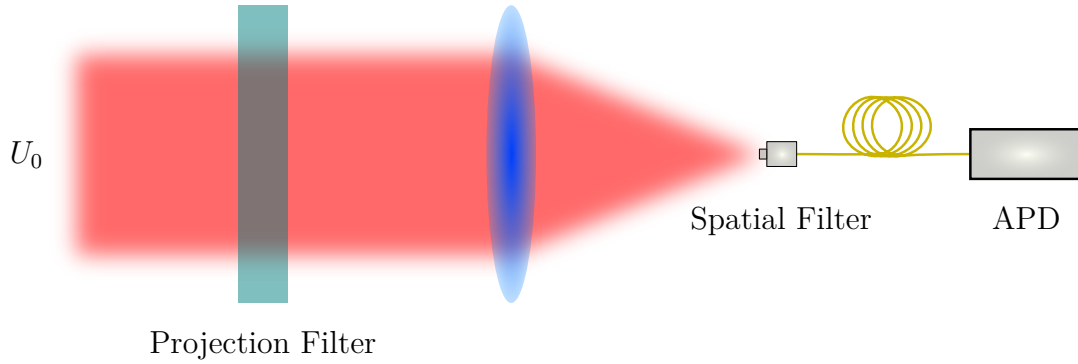


Figure 3.14: Setup for the projection measurement of spatial modes. A beam is transmitted through a filter with complex transmission given by ψ_n^* and then spatially filtered in the Fourier plane of the filter. The probability of detection is proportional to the mode overlap between the input state and projected mode ψ_n .

An input field U_0 is incident on a complex filter with transmission function $T(\mathbf{r})$. A lens takes the filtered field U_0T to the Fourier plane located at the fiber, where the fiber spatially filters the field with filter function $f(\boldsymbol{\rho})$. If we write the field in the

Fourier plane as

$$\tilde{U}(\boldsymbol{\rho}) = \frac{1}{i\lambda f} \mathcal{F} [U_0(\mathbf{r})T(\mathbf{r})] = \frac{1}{i\lambda f} \iint U_0(\mathbf{r})T(\mathbf{r})e^{-i\frac{2\pi}{\lambda f}\mathbf{r}\cdot\boldsymbol{\rho}} d\mathbf{r}. \quad (3.63)$$

The overall efficiency of the coupling η is then given by

$$\eta = \left| \iint \tilde{U}(\boldsymbol{\rho})f(\boldsymbol{\rho}) d\boldsymbol{\rho} \right|^2 \approx \left| \tilde{U}(0) \iint \tilde{f}(\boldsymbol{\rho}) d\boldsymbol{\rho} \right|^2 \propto |\tilde{U}(0)|^2, \quad (3.64)$$

where we assume that the filter function is narrow enough that $\tilde{U}(\boldsymbol{\rho})$ doesn't change appreciably within the filter. Now if we assume that the complex filter is given by

$$T(\mathbf{r}) = \psi_n^*(\mathbf{r}), \quad (3.65)$$

then the efficiency is given by

$$\eta \propto |\tilde{U}(0)|^2 \propto \left| \iint U_0(\mathbf{r})\psi_n^*(\mathbf{r}) d\mathbf{r} \right|^2 = |a_n|^2, \quad (3.66)$$

and thus we have a projection measurement of state ψ_n .

3.2.2 Mode sorting of spatial modes

Projection measurements are good for deciding if an unknown field $|U_0\rangle$ is orthogonal to some particular state $|\psi_n\rangle$, but it does not tell you what particular state $|U_0\rangle$ was

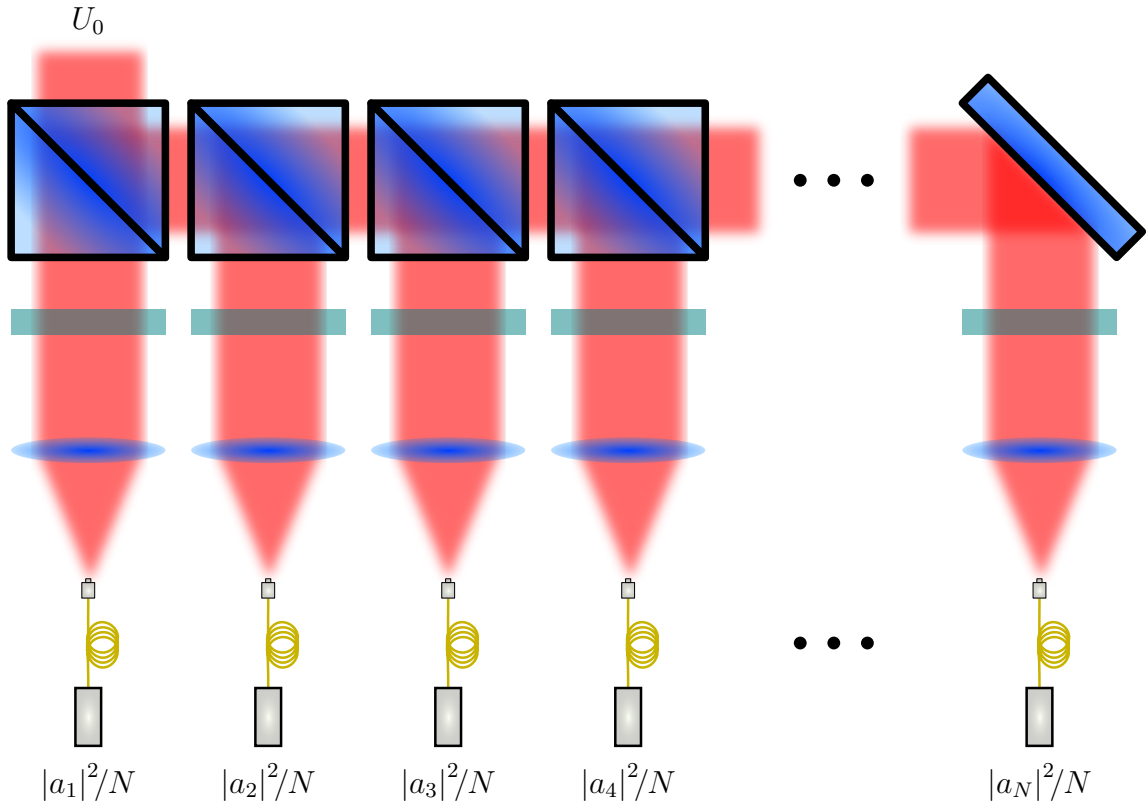


Figure 3.15: A scheme for determining which of N possible states the field was prepared in by splitting the field into N parts and performing N projection measurements in parallel to determine the state.

actually prepared in. If $|U_0\rangle$ was prepared in some state $|\psi_n\rangle$ such that $n \in [1, N]$, then one would have to make N different projection measurements. This can be done sequentially, or in parallel as shown in Fig. 3.15. This is detrimental if one is trying to maximize the information capacity via these modes. In the first case this would result in Alice having to send each symbol N times, resulting in a $1/N$ drop in channel capacity. If Bob tried to split the signal to make N parallel projection measurements, then this would result in an additional factor of N loss which would also substantially diminish the channel capacity by either decreasing the probability of detection for

single photon communication, or by decreasing the signal by a factor of $1/N$ (and thus also decreasing the total signal to noise ratio as well).

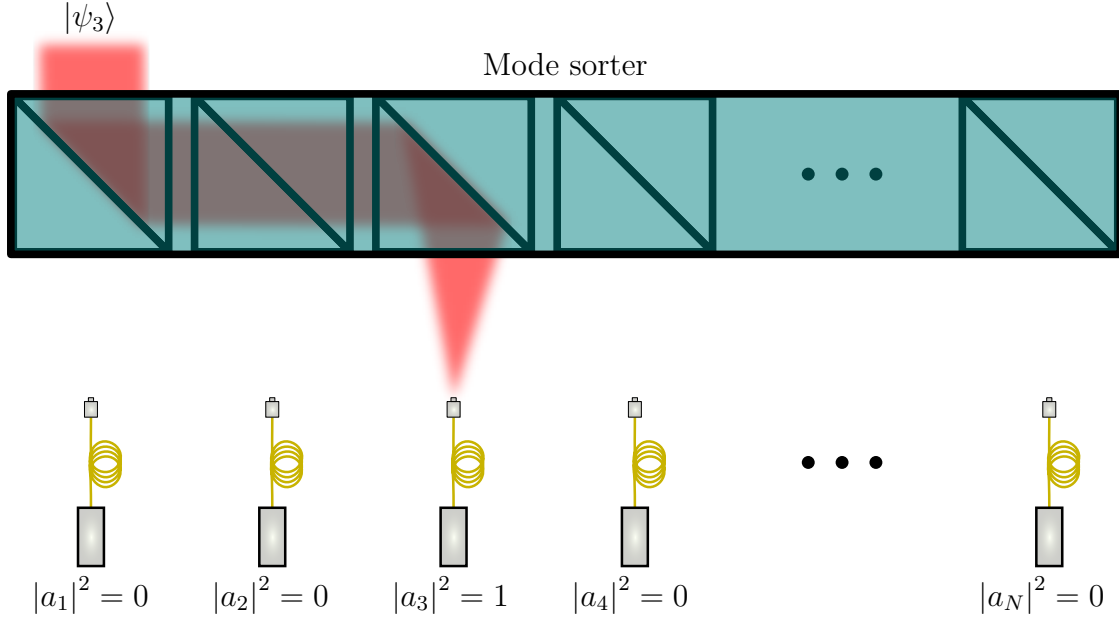


Figure 3.16: Ideal sorter deterministically separating the input mode into the correct port.

An alternative method of measurement is to find a way to split the field into N channels that depends on each mode itself rather than indiscriminately splitting the field. An ideal scheme is shown in Fig. 3.16 where an input mode $|\psi_3\rangle$ is selected by the third port and sorted into the $n = 3$ detector. Ideal sorting can be written as the unitary transformation

$$\hat{T} |U_0\rangle = \sum_n |\phi_n\rangle \langle \psi_n | U_0\rangle, \quad (3.67)$$

where $|\phi_n\rangle$ is a set of modes that do not spatially overlap, i.e. for which

$$\langle \phi_m | \mathbf{r} \rangle \langle \mathbf{r} | \phi_n \rangle = 0, \forall n \neq m. \quad (3.68)$$

It is a known fact that any discrete operator such as \hat{T} can be decomposed into a discrete number of interferometric operations [49], and this has been demonstrated for the case of separating OAM modes [50]. However, such a method requires $N - 1$ cascaded interferometers to sort N modes, which is experimentally difficult to implement even when trying to sort just a few modes.

An alternative method is to try to find a transformation \hat{T} that will directly transform an entire set of modes at once. An example set of modes for which such a transformation is well known are plane wave states, which can be transformed into a set of spatially separated spots by a Fourier transforming lens. Therefore if one can transform a set of modes into plane wave states, sorting can be done with a simple lens.

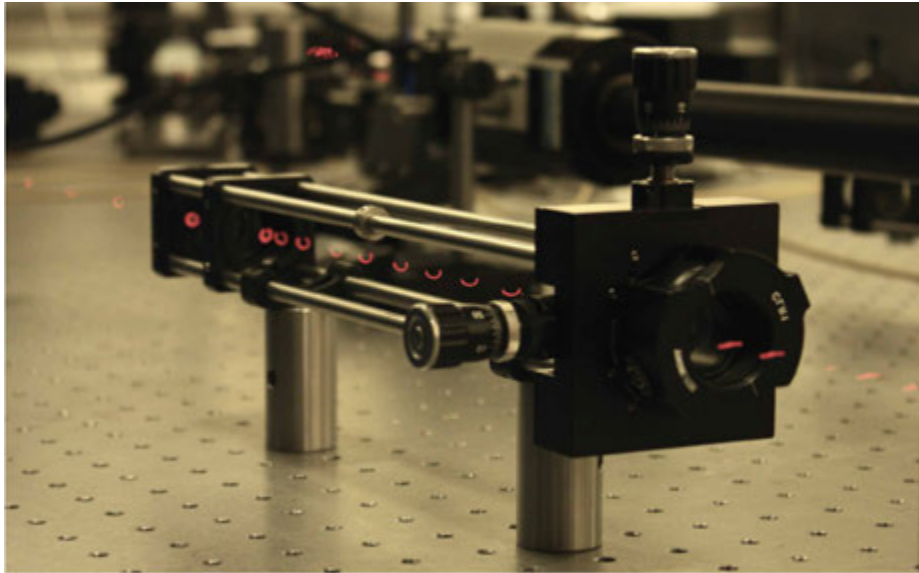


Figure 3.17: Image of the transformation optics necessary to create an optical log-polar mapping. Images of an OAM beam at multiple planes were captured to show the transformation of a circular OAM mode to a linear plane wave state. Image from [51].

It has been shown that there exists a map that takes OAM states to plane wave states [51–53] using an optical log-polar map [54, 55] which makes the geometric transformation

$$(x, y) \mapsto (u, v) = (-a \ln(r/b), a\phi), \quad (3.69)$$

where a and b are scaling parameters, $r^2 = x^2 + y^2$, and $\phi = \arctan(y, x)$. This is done via transmission of the beam U_0 through a phase element with phase

$$\phi_1(x, y) = \frac{2\pi a}{\lambda f} (y\phi - x \ln(r/b) + x). \quad (3.70)$$

The field is then taken to a Fourier plane of a lens with focal length f which gives a transformed field [52]

$$\mathcal{F} \left(U_0(x, y) e^{i\phi_1(x, y)} \right) \approx U_0(u, v) e^{i\phi_2(u, v)} \quad (3.71)$$

where

$$\phi_2(u, v) = \frac{2\pi ab}{\lambda f} \exp(-u/a) \cos(v/a). \quad (3.72)$$

A second phase element is then used to correct the additional phase ϕ_2 in the final beam. Therefore if one has an OAM mode $U_0 \sim e^{i\ell\phi}$, then this will be transformed to

$$U_0 \sim e^{i\ell\phi} \rightarrow e^{i\ell v/a}, \quad (3.73)$$

which is a truncated plane wave with ℓ waves of tilt across the beam. An image of the transformation optics used in many of our experiments is shown in Fig. 3.17 transforming an OAM beam into a plane wave state.

3.3 OAM QKD

In order to demonstrate the use of the methods developed in sections 3.1 – 3.2 we implemented a high-dimensional quantum key distribution system based on the azimuthal degree of freedom spanned by the seven lowest order OAM spatial modes for the encoding [3]. A schematic of the setup used is shown in Fig. 3.18. A collimated Helium-Neon laser beam illuminates a DMD to generate spatial modes at up to 4 KHz using the method described in section 3.1.3. We use a scheme that is a high dimensional generalization of the BB84 protocol described in chapter 1 in which Alice picks a random sequence of desired symbols from multiple MUBs and transmits them to Bob. For each symbol, Alice triggers the DMD and modulates the beam using an acousto-optic modulator to create rectangular pulses of 125 ns width. The beam is attenuated such that each pulse contains an average photon number of $\bar{n} = 0.1$, ensuring that the probability of a pulse containing multiple photons is negligible. The prepared states are then imaged to Bob’s receiving aperture via a $4f$ telescope, forming a two meter long communication link.

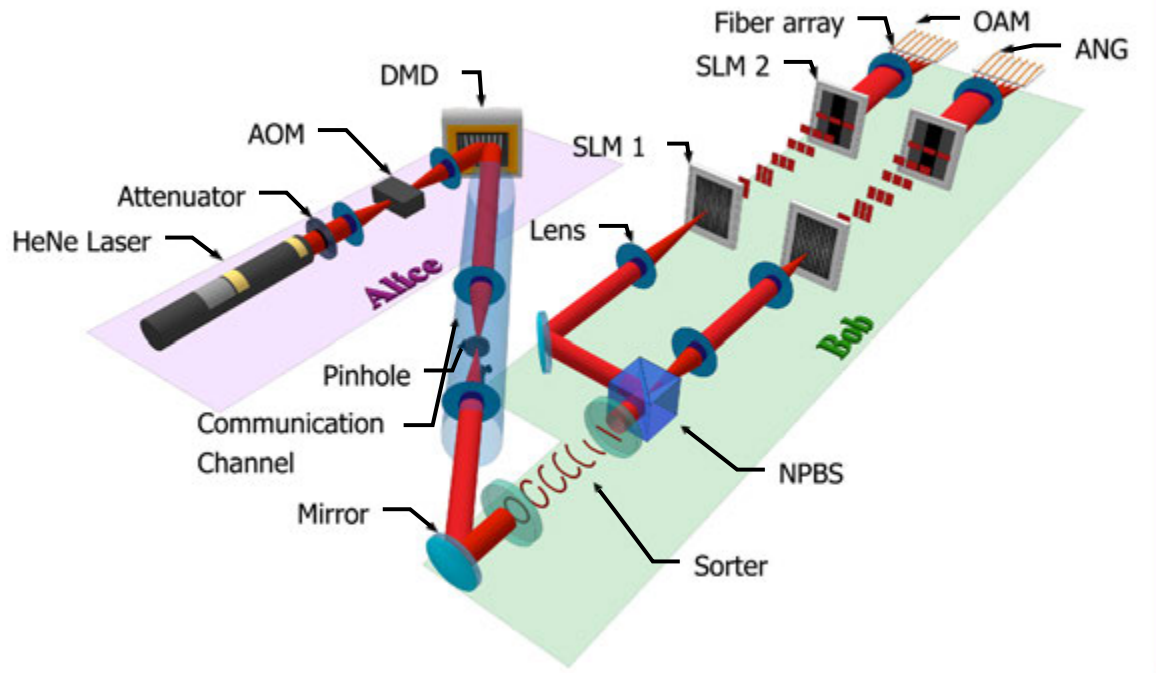


Figure 3.18: Setup used for demonstration of a free-space, spatially encoded quantum key distribution system.

As was discussed in section 1.2, a QKD system based on the BB84 protocol needs encoding in at least two sets of MUBs for security. Our first basis was a pure vortex OAM basis given by

$$\Psi_\ell(\phi) = \frac{1}{2\pi} e^{i\ell\phi}, \quad (3.74)$$

where $\ell \in [-3, 3]$. Our second MUB was constructed from the OAM modes via a discrete Fourier transform of the state space to ensure the states are unbiased. These states are localized in the azimuthal angle and we thus call such states angular (ANG) states, which can be expressed as

$$\Theta_n = \frac{1}{\sqrt{d}} \sum_{\ell=-N}^N \Psi_\ell \exp\left(\frac{i2\pi n\ell}{d}\right), \quad (3.75)$$

where

$$d = 2N + 1 = 7 \quad (3.76)$$

is the dimension of the space. It is immediately obvious that these states are mutually unbiased with respect to the OAM states as

$$\begin{aligned} \langle \Psi_\ell | \Theta_n \rangle &= \frac{1}{\sqrt{d}} \sum_{\ell'=-N}^N \langle \Psi_\ell | \Psi_{\ell'} \rangle \exp\left(\frac{i2\pi n \ell'}{d}\right) \\ &= \frac{1}{\sqrt{d}} \sum_{\ell'=-N}^N \delta_{\ell, \ell'} \exp\left(\frac{i2\pi n \ell'}{d}\right) \\ &= \frac{1}{\sqrt{d}} \exp\left(\frac{i2\pi n \ell}{d}\right), \end{aligned} \quad (3.77)$$

and therefore

$$|\langle \Psi_\ell | \Theta_n \rangle|^2 = 1/d \quad \forall n \text{ and } \ell. \quad (3.78)$$

Images of both the OAM and ANG set of modes is shown in Fig. 3.19 as well as sample CGHs used to generate each basis.

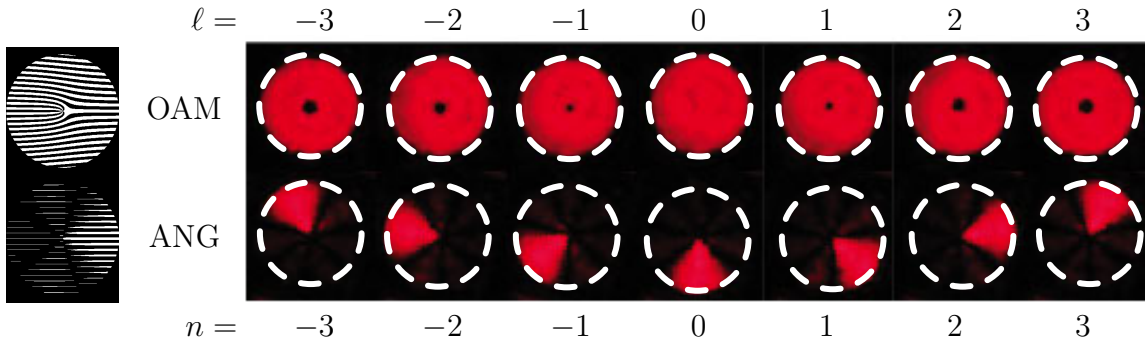


Figure 3.19: CCD images of the spatial light fields of the OAM (top) and ANG (bottom) basis. Example binary holograms used for the generation of these modes are also shown on the left.

Bob’s system consists of two refractive elements that perform the log-polar transformation that was described in section 3.2. After this transformation the OAM modes are converted to plane-wave states, while the ANG modes are mapped to localized spots. The OAM modes are Fourier transformed to spots focused onto an array of fibers coupled to APDs, while the ANG spots are imaged to a similar array of fibers. The additional two SLMs (labeled “SLM 1” and “SLM 2” in the figure setup) are used to create coherent copies of the spots and recombine them in such a way that the overlap between the modes is suppressed, thus eliminating most of the cross-talk in detection [56, 57].

As was described in section 1.1 we can characterize the capacity of the channel by the mutual information (Eq. (1.11)) between Alice and Bob given by

$$I(A; B) = H(B) - H(B|A) = \log(d) + \sum_{a,b} \frac{p(b|a)}{d} \log(p(b|a)), \quad (3.79)$$

where $p(b|a)$ is the conditional probability of Bob detecting mode $B = b$ given that Alice sent mode $A = a$. A plot of the measured values for $p(b|a)$ is shown in Fig. 3.20. If we assume that only Bob detects each mode with the same fidelity F that characterizes the probability of measurement of the “correct” mode and the probability of measuring the wrong state is equally likely in any of the remaining $d - 1$ modes, then Eq. (3.79)

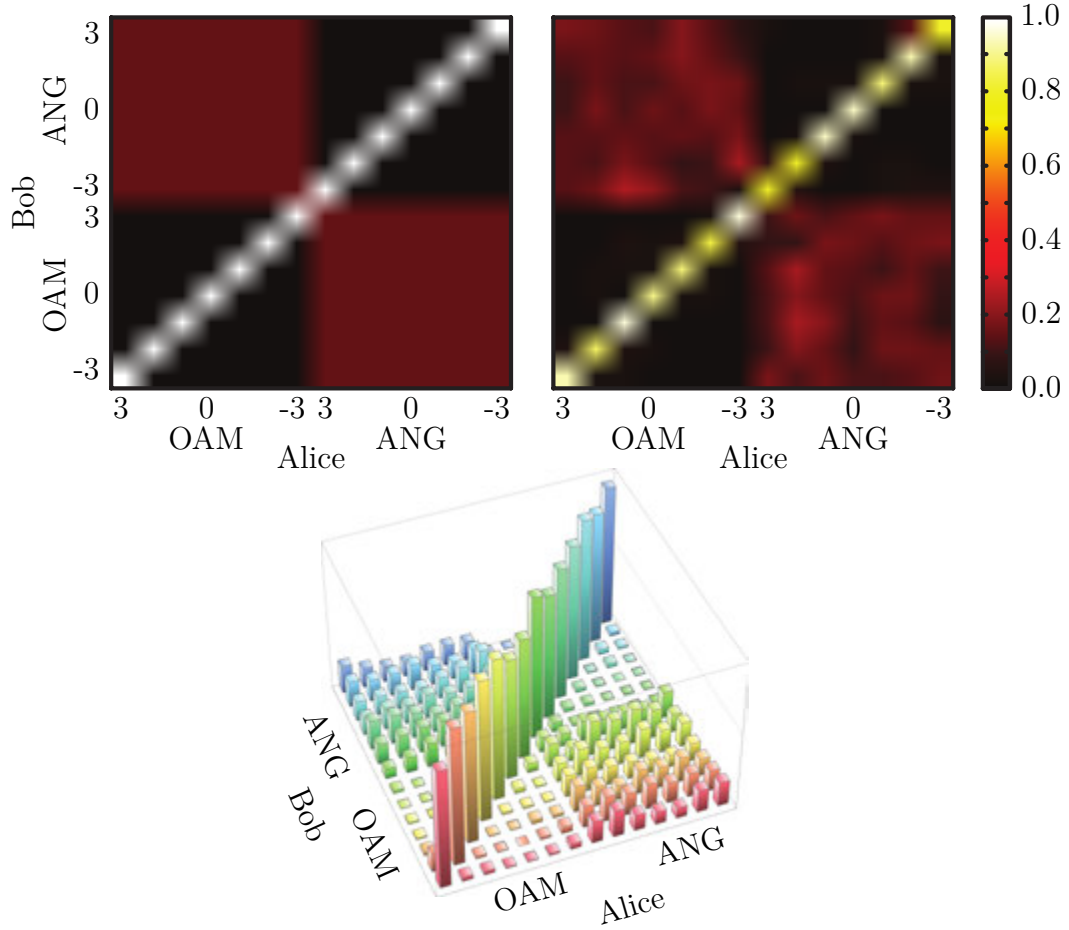


Figure 3.20: Measured conditional probabilities $p(b|a)$ that Bob measured state b given that Alice sent mode a . Top left shows the plot of an ideal system, while the right and bottom show the plot and histograms for the measured data.

takes on the form

$$\begin{aligned}
 I(A; B) &= \log(d) + \sum_{a,b} \frac{p(b|a)}{d} \log(p(b|a)) \\
 &= \log(d) + \sum_b p(b) \log(p(b)) \\
 &= \log(d) + F \log(F) + (1 - F) \log\left(\frac{1 - F}{d - 1}\right).
 \end{aligned} \tag{3.80}$$

For our experiment the average fidelity was given by $F = 0.895$, and thus Bob's symbol error probability is

$$e_B = 1 - F = 0.105, \tag{3.81}$$

or 10.5%. About 4% of the error is measured to be from the APD dark counts, while the remaining 6.5% is due to cross-talk among different modes within the same measured basis. From this information the measured mutual information is

$$I(A; B) = 2.05 \text{ bits/sifted photon.} \tag{3.82}$$

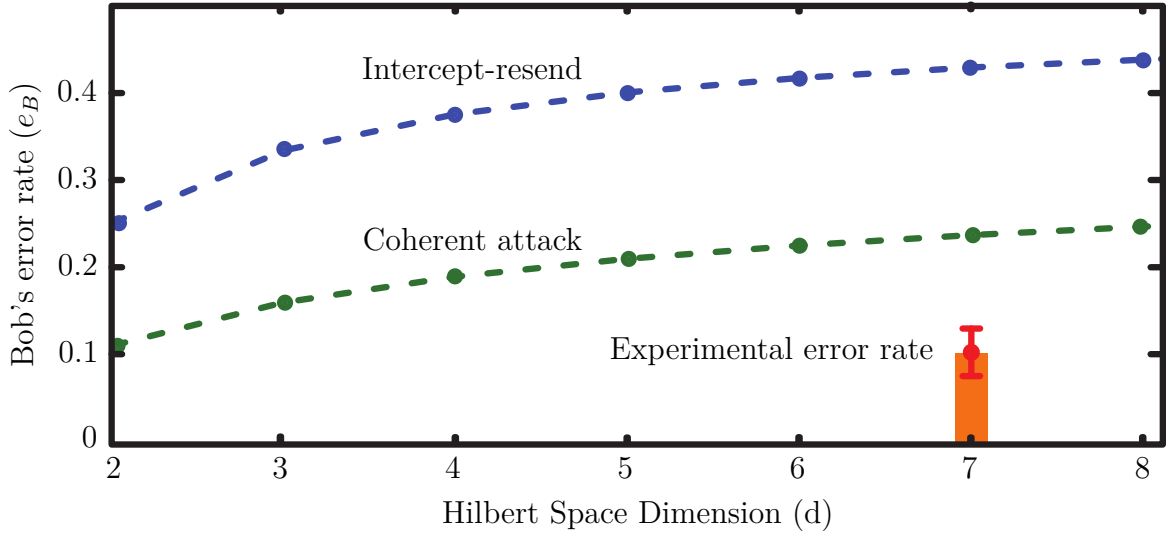


Figure 3.21: Error-bounds for unconditional security using a alphabet size of dimension d . Shown are the bounds for an intercept-resend strategy (assuming only two MUBs), as well as a full coherent attack. In addition, the measured error rate of our system is shown demonstrating we are well below both security bounds.

As was discussed in section 1.2 the measurement of the error will determine if there was an eavesdropper in the channel and if one can still extract a secure key. A

plot of the security error bounds on e_B as a function of the size of the Hilbert space dimension d is shown in Fig. 3.21. Plotted are the error bounds for an intercept-resend attack as well as the more optimal coherent based attack [14]. Our measured error rate demonstrates our system was unconditionally secure against both such attacks.

Our raw key generation rate was found to be 16.4 bits/s. After performing basis reconciliation between Alice and Bob, as well as error correction and privacy amplification to reduce Eve's information to zero, our final secure key rate was estimated to be 6.5 bits/s. This is more than three orders of magnitude larger than any previously demonstrated spatial mode encoded QKD scheme [17].

Chapter 4

Communication with a noisy channel

Understanding how light propagates is one of the most fundamental topics in the field of optics. For deterministic systems, such as the treatment presented in chapter 2, this problem is well understood. However, the problem of understanding how light behaves in random or fluctuating media is still a very active area of research [58–60]. Even propagation through the air, which at first glance might be thought of as being equivalent to vacuum or free-space propagation, will show stochastic behavior when observed over sufficiently long distances due to the atmospheric turbulence, which induces small random fluctuations in the refractive index along the path.

4.1 Atmospheric turbulence

Turbulence is a phenomenon that occurs in any fluid that is characterized by a large Reynolds number

$$\mathcal{R} = \bar{v}\mathcal{L}/\nu, \tag{4.1}$$

where \bar{v} is the fluid's mean velocity, \mathcal{L} is the length scale of the fluid, and ν is the viscosity. The fluid will then break up into a cascade of turbulent eddies of decreasing size until the length scale, $\mathcal{L} = l_0$ is such that $\mathcal{R} \leq 1$ and the kinetic energy can be dissipated as heat [61]. The length l_0 is known as the inner scale and is typically on the order of millimeters near the ground, and is often considered negligibly small relative to the length scales in a free-space communication channel [58]. The viscosity of air is of order 10^{-5} m²/s, near the ground, \mathcal{L} is on the scale of meters, and wind speeds are typically many tens of meters per second. Therefore the atmosphere has a typical Reynolds number

$$\mathcal{R} \sim 10^6 \gg 1, \quad (4.2)$$

and thus it is safe to assume the atmosphere is always turbulent.

The fluid velocity $v(r)$ at any point r in a turbulent fluid is a random process whose spatial structure can be described by the structure function, defined as

$$D_v(\mathbf{r}_1, \mathbf{r}_2) \equiv \langle |v(\mathbf{r}_1) - v(\mathbf{r}_2)|^2 \rangle. \quad (4.3)$$

For $\|\mathbf{r}_1 - \mathbf{r}_2\| > l_0$ the structure function is governed by “Kolmogorov statistics,” given by

$$D_v = C_v^2 \delta r^{2/3}, \quad (4.4)$$

where $\delta r \equiv \|\mathbf{r}_1 - \mathbf{r}_2\|$, and where C_v^2 is known as the velocity structure parameter which characterizes the strength of the fluctuations [61]. The turbulent eddies will

mix the air, creating pockets of slightly different temperatures and thus pressures. As a consequence of this variation in air pressure, the index of refraction will also vary statistically in the same way, leading to the refractive index structure function [62]

$$D_n = C_n^2 \delta r^{2/3}. \quad (4.5)$$

The random fluctuations in the index of refraction is characterized by D_n and lead to a random phase, $\phi(\mathbf{r})$ at the receiver. It was shown by Fried [63] that for Kolmogorov turbulence the phase structure function can be given by

$$D_\phi = 6.88 \left(\frac{\delta r}{r_0} \right)^{5/3}, \quad (4.6)$$

where r_0 is an effective coherence length known as Fried's parameter and can be calculated from C_n^2 by the formula

$$r_0 = \left[\frac{2.91}{6.88} k^2 \int_0^L C_n^2(z) dz \right]^{-3/5} = \left[\frac{2.91}{6.88} k^2 C_n^2 L \right]^{-3/5}, \quad (4.7)$$

where we have assumed for simplicity a constant value for C_n^2 along the path.

A random phase imprinted on an optical beam will, upon propagation lead to variations in the amplitude as well. Thus the field is modified at the receiver in both

the phase and the amplitude. We can write the field as

$$U(\mathbf{r}) = U_0(\mathbf{r}) \exp(i\phi(\mathbf{r}) + \chi(\mathbf{r})), \quad (4.8)$$

where U_0 is the field in the absence of turbulence, ϕ is the random phase, and χ is the random log-amplitude. These amplitude fluctuations, or “scintillations” can then be characterized by the variance in χ which is calculated from C_n^2 as [62]

$$\sigma_\chi^2 = 0.563k^{7/6} \int_0^L C_n^2(z) z^{5/6} dz = \frac{0.563 * 6}{11} k^{7/6} C_n^2 L^{11/6}. \quad (4.9)$$

Not only does χ cause scintillation within the beam, but this also leads to fluctuations in the total power of the beam, even if there are no losses in the path itself. These power fluctuations are due to beam wander and clipping by the finite aperture at the receiver. The normalized power over the aperture Σ of area A_Σ , defined by

$$P \equiv \frac{1}{A_\Sigma} \int_\Sigma d\mathbf{r} \exp(2\chi(\mathbf{r})), \quad (4.10)$$

is used to numerically find the normalized power variance in the aperture,

$$\sigma_P^2 \equiv \langle P^2 \rangle - \langle P \rangle^2 = \langle P^2 \rangle - 1 = \frac{1}{A_\Sigma^2} \iint_{\Sigma\Sigma'} \left(e^{4C_\chi(\mathbf{r},\mathbf{r}')} - 1 \right) d\mathbf{r} d\mathbf{r}' - 1, \quad (4.11)$$

where

$$C_\chi(\mathbf{r}, \mathbf{r}') = \left\langle (\chi(\mathbf{r}) - \langle \chi \rangle) (\chi(\mathbf{r}') - \langle \chi \rangle) \right\rangle \quad (4.12)$$

is the log-amplitude covariance function [58].

For thick turbulence it is known that some of the degradations caused by turbulence can still be compensated for by phase-only adaptive optics (AO), correcting for low-spatial-frequency aberrations for a horizontal path of a few kilometers or more [64]. For stronger scintillation one will begin to see intensity nulls that are associated with phase vortices [65, 66]. These phase vortices, or branch points, are known to degrade the performance of AO systems [67], and there is a complete breakdown in the performance for horizontal paths greater than approximately 5 km due to this effect [68]. For communication systems that communicate using OAM, this phenomenon presents an additional problem as phase vortices are precisely the means of the encoding, and randomly generated vortices introduce errors into such a scheme.

4.2 Thin-phase turbulence

Early research studying optical propagation along random paths arose in the context of imaging of astronomical objects through the turbulence in atmosphere [69]. The most important effect on image quality in such systems is the random phase imprinted onto the beam by the turbulence. This phase aberration can be described by Fried's parameter r_0 defined in the previous chapter. Fried's parameter defines a coherence

length scale of the turbulence defined in the receiver aperture [63, 70]. If all other effects of turbulence can be ignored (e.g. amplitude fluctuations), then the turbulence can be approximated by a random phase screen in the aperture of the receiver. This approximation, known as the “thin phase screen approximation,” simplifies the problem and allows the turbulence strength to be fully characterized by the dimensionless parameter D/r_0 where D is the diameter of the aperture or beam. Thus the effects of turbulence depend not only on the intrinsic fluctuations in the air, but also on details of the system. This thin screen approximation is often appropriate in astronomical systems as turbulence effects on beam propagation are greatest where the atmosphere is thickest, which is typically located directly in front of the telescope. Although this approximation is less appropriate for communication through a continuous turbulent channel, it nevertheless provides a simple model that makes studying the basic effects of turbulence a more tractable problem.

A representation of the thin-phase turbulence model is shown in Fig 4.1. All phase fluctuations due to the turbulence in the channel are summed up and represented as a single thin phase screen in the receiver’s aperture. This random phase screen obeys Kolmogorov statistics specified by Eq. (4.6) and characterized by the single dimensionless parameter D/r_0 . A few realizations of Kolmogorov screens of different strengths are also shown in the figure.

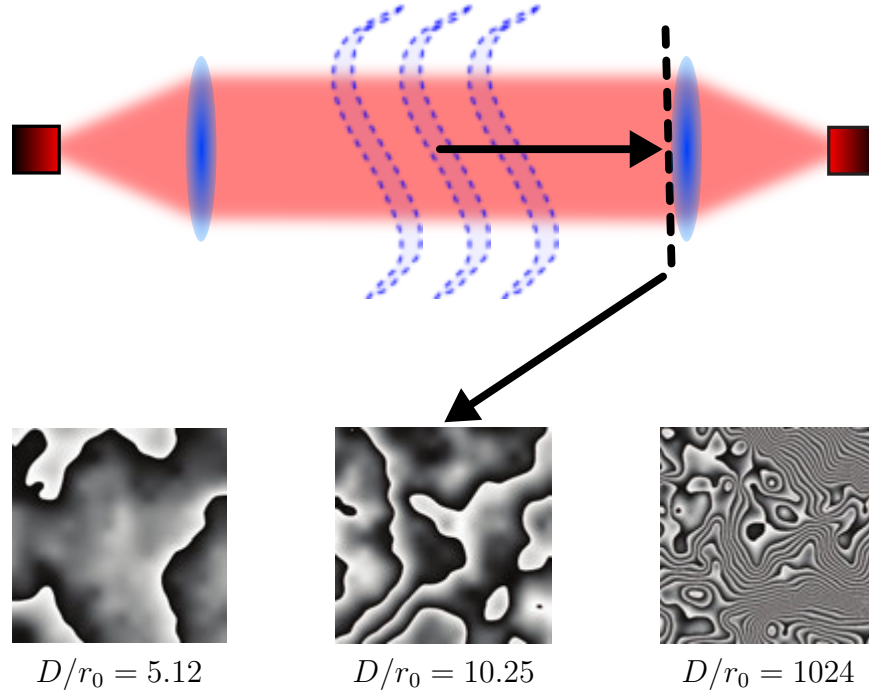


Figure 4.1: Top: channel with turbulence represented by a phase screen at the receiver. Bottom: three different instantaneous realizations of turbulence induced phase variation for different turbulence strengths D/r_0 .

4.2.1 OAM encoding with thin-phase turbulence

A turbulent channel, represented by a single thin random phase screen can be simulated using the methods developed in chapter 3. We used this method to first examine the effects of thin-phase turbulence on OAM encoding [5, 6]. If in the absence of turbulence Bob would have received mode

$$\langle \mathbf{r} | \Psi_\ell \rangle = \psi_\ell(r) e^{i\ell\theta}, \quad (4.13)$$

then with turbulence Bob will actually receive the (instantaneous) mode

$$\langle \mathbf{r} | \exp(i\hat{\phi}) | \Psi_\ell \rangle = \psi_\ell(r) e^{i\ell\theta} e^{i\phi(\mathbf{r})}, \quad (4.14)$$

where $\phi(\mathbf{r})$ is a random screen with Kolmogorov statistics.

Since the thin-phase turbulence operator $\exp(i\hat{\phi})$ is unitary, there is no loss in this model. Therefore the effect of $\exp(i\hat{\phi})$ on the channel will be to diminish the mutual information between Alice and Bob. This is quantified by the modification of the conditional probabilities in the expression for the mutual information (Eq. (1.11)). The conditional probability of measuring a field with OAM value $\ell + \Delta$, given that Alice sent mode Ψ_ℓ is given by

$$\begin{aligned} p(\ell + \Delta | \Psi_\ell) &= \sum_m \left| \langle m, \ell + \Delta | \exp(i\hat{\phi}) | \Psi_\ell \rangle \right|^2 \\ &= \sum_m \left| \int d\mathbf{r} \langle m, \ell + \Delta | \mathbf{r} \rangle \psi_\ell(r) e^{i\ell\theta} e^{i\phi(\mathbf{r})} \right|^2 \\ &= \sum_m \left| \int d\mathbf{r} R_{m, \ell + \Delta}^*(r) e^{-i(\ell + \Delta)\theta} \psi_\ell(r) e^{i\ell\theta} e^{i\phi(\mathbf{r})} \right|^2 \\ &= \sum_m \left| \int d\mathbf{r} R_{m, \ell + \Delta}^*(r) e^{-i\Delta\theta} \psi_\ell(r) e^{i\phi(\mathbf{r})} \right|^2, \end{aligned} \quad (4.15)$$

where

$$\langle \mathbf{r} | m, \ell \rangle = R_{m, \ell}(r) e^{i\ell\theta} \quad (4.16)$$

is a complete, orthonormal set of spatial modes.

Now $\phi(\mathbf{r})$ is a random variable and so we also need to perform an ensemble average to compute the average or scattered mode s_Δ . This is given by

$$\begin{aligned}
s_\Delta &\equiv \langle p(\ell + \Delta | \Psi_\ell) \rangle \\
&= \iint d\mathbf{r} d\mathbf{r}' \left(\sum_m R_m^*(r) R_m(r') \right) e^{i\Delta(\theta - \theta')} \psi_\ell^*(r') \psi_\ell(r) \langle e^{-i[\phi(\mathbf{r}) - \phi(\mathbf{r}')] } \rangle \\
&= \iint d\mathbf{r} d\mathbf{r}' \left(\frac{\delta(r - r')}{r'} \right) e^{i\Delta(\theta - \theta')} \psi_\ell^*(r') \psi_\ell(r) \langle e^{-i[\phi(\mathbf{r}) - \phi(\mathbf{r}')] } \rangle \\
&= \int r dr \iint d\theta d\theta' e^{i\Delta(\theta - \theta')} |\psi_\ell(r)|^2 \langle e^{-i[\phi(r, \theta) - \phi(r, \theta')] } \rangle \\
&= \int r dr \iint d\theta d\theta' e^{i\Delta\delta\theta} |\psi_\ell(r)|^2 C(r, \delta\theta),
\end{aligned} \tag{4.17}$$

where $\delta\theta = \theta - \theta'$ and $C(r, \delta\theta)$ is the rotational coherence function [71]. The coherence function can be written as

$$\begin{aligned}
C(r, \delta\theta) &= \langle e^{-i[\phi(r, \delta\theta) - \phi(r, 0)] } \rangle \\
&= e^{-1/2 \langle [\phi(r, \delta\theta) - \phi(r, 0)]^2 \rangle} \\
&= e^{-3.44(D/r_0)^{5/3} (\rho \sin(\delta\theta/2))},
\end{aligned} \tag{4.18}$$

where D is the diameter of the mode, ρ is a unitless radius, and we have used the fact that ϕ obeys Kolmogorov statistics. If we can ignore the radial variation in mode intensity (i.e. assume that the radial intensity is equal to a top-hat beam of width D)

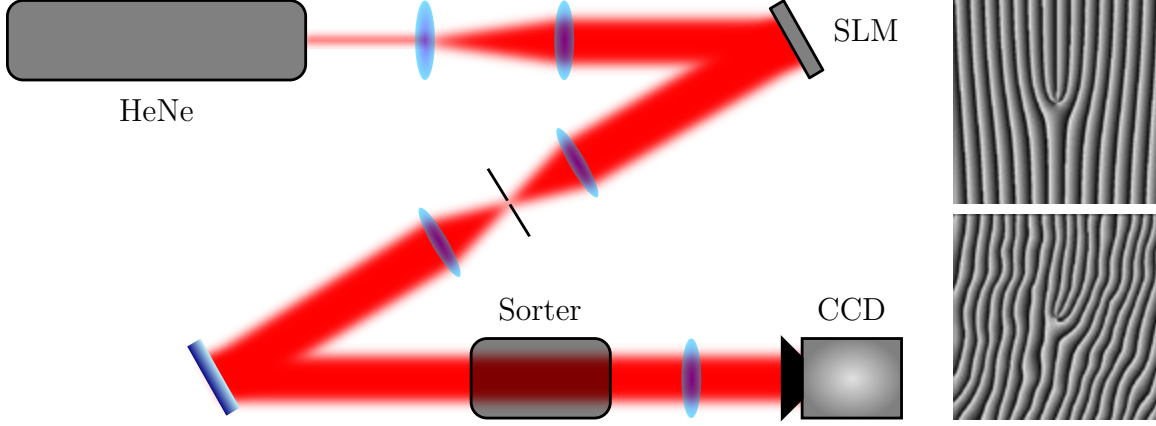


Figure 4.2: Left: an experimental setup used to simulate a channel with thin-phase turbulence. Right: typical blazed grating holograms used to generate an OAM mode with (top) and without (bottom) turbulence.

then Eq. (4.17) becomes [72],

$$\begin{aligned}
 s_{\Delta} &= \frac{1}{\pi} \int |\psi_{\ell}(\rho D/2)|^2 \rho d\rho \int e^{-3.44(D/r_0)^{5/3}(\rho \sin(\theta/2))^{5/3}} \cos(\Delta\theta) d\theta \\
 &\approx \frac{1}{\pi} \int_0^1 \rho d\rho \int e^{-3.44(D/r_0)^{5/3}(\rho \sin(\theta/2))^{5/3}} \cos(\Delta\theta) d\theta.
 \end{aligned} \tag{4.19}$$

Since the instantaneous effect of turbulence is simply a constant random phase $\phi(\mathbf{r})$, we can simulate a turbulent channel by adding this phase to the prepared mode. A schematic for this setup is shown in Fig. 4.2 along with typical holograms used to generate an OAM mode both with and without turbulence. The generated mode (including the turbulent phase) is then imaged onto the OAM mode transformer that was described in section 3.2 and the Fourier transforming lens focuses the spatially separated OAM spectrum onto a CCD.

Adjacent, equally sized regions are selected on the CCD image, with each region corresponding to a specific OAM mode. The horizontal sum of the measured pixel

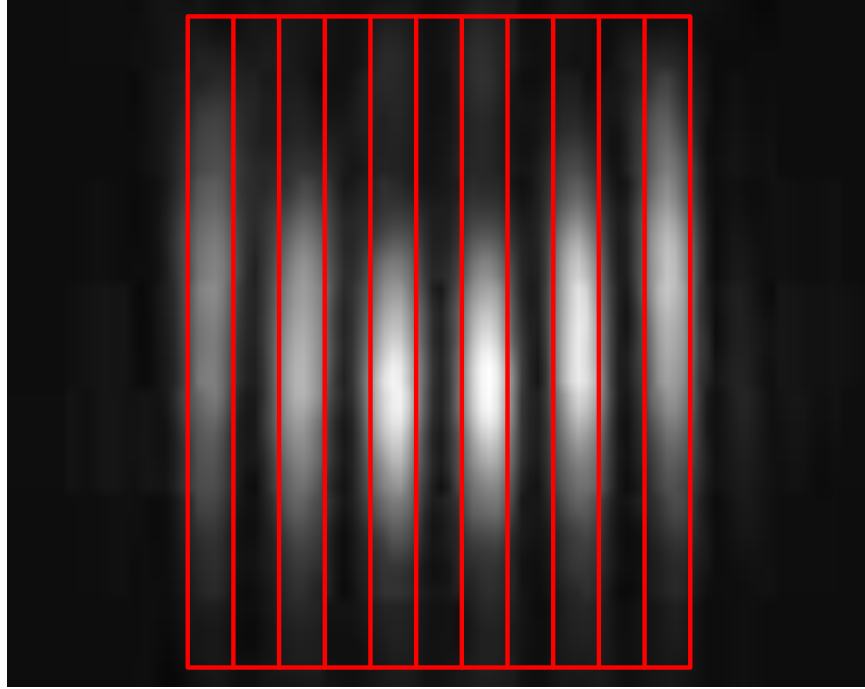


Figure 4.3: Incoherent image of the odd OAM modes with indices $\ell \in [-5, 5]$. The red boxes indicate the binned area representing each of the eleven OAM modes measured in the spectrum.

values in each of these regions is proportional to the power of the beam in each OAM mode at a particular radial location. By also summing over the pixels vertically, we also get a sum over radial modes. For each input mode, this power is measured across eleven regions corresponding to the range $\ell \in [-5, 5]$ and normalized with respect to the signal for input $\ell = 0$ with no turbulence applied. An image comprised of an incoherent superpositions of OAM modes at the location of the CCD are shown in Fig. 4.3 along with the outlines of the spatial bins used.

A range of turbulence levels characterized by $D/r_0 \in [10^{-2}, 10^2]$ were tested, with each data point averaged over one hundred realizations. Care was taken to stay within the spatial frequency bandwidth of the SLM, as features smaller than the pixel

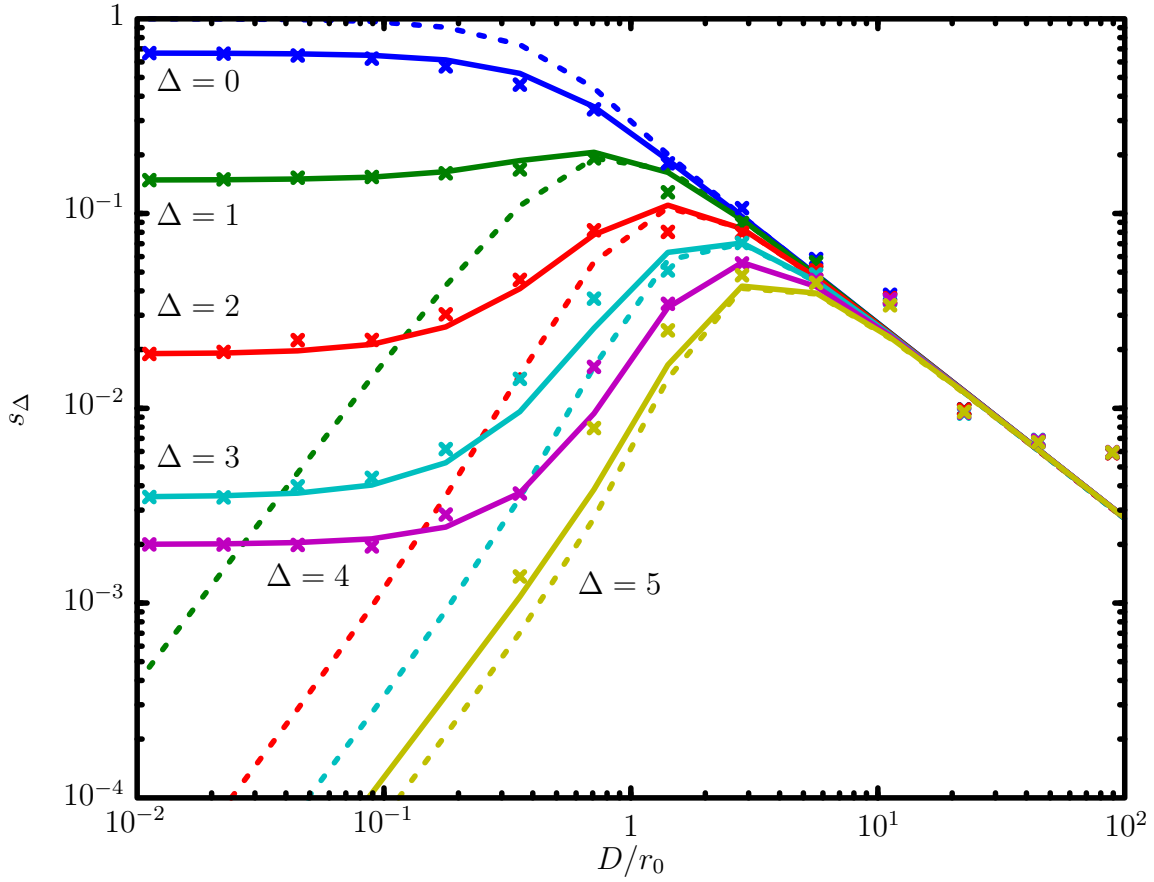


Figure 4.4: The average OAM power spectrum s_{Δ} detected in OAM mode $\ell + \Delta$ is plotted as a function of turbulence strength D/r_0 for an input mode with $\ell = 0$. Experimental data (crosses) is co-plotted with the theoretical prediction given by Eq. (4.19) both with the inherent mode sorter crosstalk (solid line) and without (dashed line).

spacing cannot be represented, setting an upper limit on the D/r_0 values that can be represented. The results are plotted in Fig. 4.4 for the case of $\ell = 0$ input. Crosses represent experimental data while dashed lines represent the predictions of Eq. (4.19) while ignoring any inherent crosstalk inherent in the mode sorting itself (i.e. inherent

crosstalk with no turbulence). This crosstalk can be included as

$$s_{\Delta}(D/r_0) = \sum_{\Delta'} s_{\Delta, \Delta'}(D/r_0 = 0) s_{\Delta}^{\text{theory}}(D/r_0), \quad (4.20)$$

where $s_{\Delta, \Delta'}(D/r_0 = 0)$ is the experimentally measured scattering matrix from mode Δ' to Δ for no turbulence and $s_{\Delta}^{\text{theory}}$ is the theoretical prediction of Eq. (4.19). For the ideal case of ideal mode sorting, this scattering matrix would be represented simply as the identity matrix. This result is shown in the figure as the solid line. As predicted, the crosstalk increases with turbulence. In the mid/high turbulence regime shown, we see good agreement between our measurements and the theory proposed in [72]. In the low turbulence regime, the crosstalk between modes arises from residual crosstalk in our mode sorter, which can be attributed to the diffraction limit [51, 52].

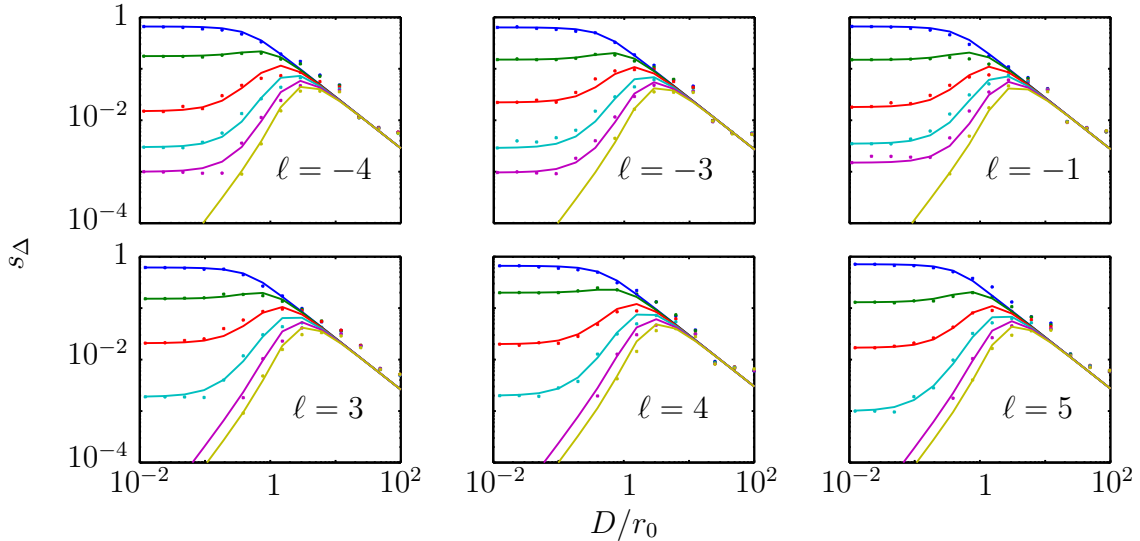


Figure 4.5: The average OAM power spectrum s_{Δ} detected in OAM mode $\ell + \Delta$ for a range of input modes ℓ demonstrating the invariance of the effects of thin-phase turbulence on input mode index.

The theory presented above indicates that the probability of modal crosstalk resulting from atmospheric turbulence is essentially independent of the input mode number, only depending on the mode difference Δ . To examine this theory, we studied the effects of turbulence on different OAM modes ranging from $\ell = -5$ to $\ell = +5$. For each of these modes, the same set of turbulent phase screens was applied. The measured crosstalk is shown in Fig. 4.5. We note that the observed crosstalk is indeed very similar for the entire range of OAM modes that we examined.

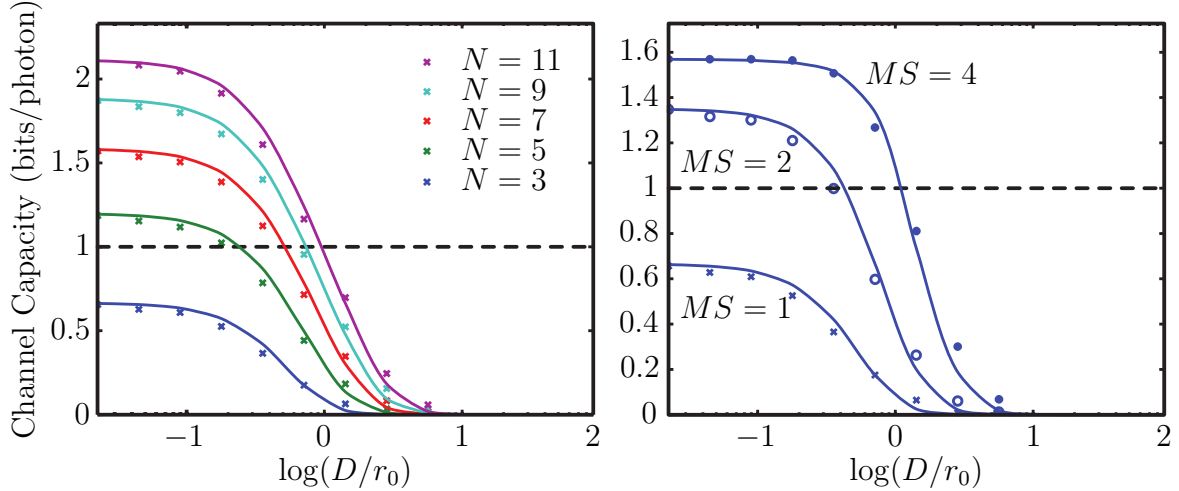


Figure 4.6: Left: plot of the channel capacities per symbol for OAM communication as a function of the turbulence strength D/r_0 for N total states. Right: effects of changing the spacing between detected modes (MS) on the channel capacity of an OAM communication system with $N = 3$ in the presence of turbulence. For a mode-spacing of 4, the maximum channel capacity for a three-dimensional system approaches the theoretical maximum of $\log_2(3) = 1.585$. Also contained in both plots is a dotted line representing the channel capacity for a system employing a two symbol alphabet using polarization for encoding (which is immune to a phase only aberration).

The non-zero crosstalk due to the fact that $s_\Delta \neq \delta_\Delta$ will obviously reduce the channel capacity. Shown in Fig 4.6 is the channel capacity per detected symbol of an OAM encoded communication system as a function of the turbulence strength D/r_0 .

The capacity will always approach 0 for $D/r_0 \gg 1$, however one can see in the left figure that the capacity is a monotonically increasing function of the total number of symbols used N . In addition, effects of turbulence can be mitigated by increasing the mode spacing MS of the modes used (e.g. $\ell \in [1, 2, 3 \dots] \rightarrow [1, 3, 5 \dots]$) due to the fact that turbulence causes a preferential scattering into neighboring modes.

4.2.2 Plane-wave encoding with thin-phase turbulence

As was demonstrated in chapter 2, if one wants to encode a large amount of information per spatial symbol, then one needs a system with a large Fresnel number product D_F . It was also shown that if the spatial frequencies of the encoded modes used is sufficiently small, i.e. in the limit that the size of the alphabet $N \ll D_F$, then the eigenmodes become degenerate and there is no preferred basis. In this limit the system is not limited by diffraction within the channel. Additionally, there is no a priori reason to believe that the communication modes are the most robust against the effects of turbulence, and in fact we've shown that even plane-wave states can be better than OAM states when limited by turbulence [4, 7].

We define an orthogonal set of (one dimensional) plane-wave states by

$$\langle \mathbf{r} | \Psi_m \rangle = \frac{1}{L^2} \text{rect}(y/L) \text{rect}(x/L) e^{i2\pi mx/L}, \quad (4.21)$$

where L is the size of the square aperture. In the presence of turbulence this becomes

$$\langle \mathbf{r} | \exp(i\hat{\phi}) | \Psi_m \rangle = \text{rect}(y/L) \text{rect}(x/L) e^{i2\pi mx/L} e^{i\phi(\mathbf{r})}, \quad (4.22)$$

where $\phi(\mathbf{r})$ is a random screen with Kolmogorov statistics. Computing the conditional probability of measuring mode $m + \Delta$, given that Alice sent mode m gives

$$\begin{aligned} p(m + \Delta | m) &= \left| \langle m + \Delta | \exp(i\hat{\phi}) | m \rangle \right|^2 \\ &= \left| \iint d\mathbf{r} \langle m + \Delta | \mathbf{r} \rangle \langle \mathbf{r} | \Psi_m \rangle e^{i\phi(\mathbf{r})} \right|^2 \\ &= \left| \frac{1}{L^2} \iint_{-L/2}^{L/2} e^{-i2\pi\Delta x/L} e^{i\phi(\mathbf{r})} dx dy \right|^2. \end{aligned} \quad (4.23)$$

Taking an ensemble average over turbulence realizations gives the scattering matrix [4]

$$\begin{aligned} s_\Delta &\equiv \langle p(m + \Delta | m) \rangle \\ &= \frac{1}{L^3} \int_{-L/2}^{L/2} dy \iint_{-L/2}^{L/2} dx dx' e^{i2\pi\Delta(x-x')/L} \langle e^{-i(\phi(x,y) - \phi(x',y))} \rangle \\ &= \frac{1}{L^2} \iint_{-L/2}^{L/2} \exp\left(-3.44 \left(|x - x'|/r_0\right)^{5/3}\right) e^{i2\pi\Delta(x-x')/L} dx dx'. \end{aligned} \quad (4.24)$$

Making the substitution $z = (x - x')/L$, and $z' = (x + x')/L$ allows us to simplify this expression to

$$s_\Delta = 8 \int_0^{1/2} dz (1/2 - z) e^{-3.44(zL/r_0)^{5/3}} \cos(4\pi\Delta z). \quad (4.25)$$

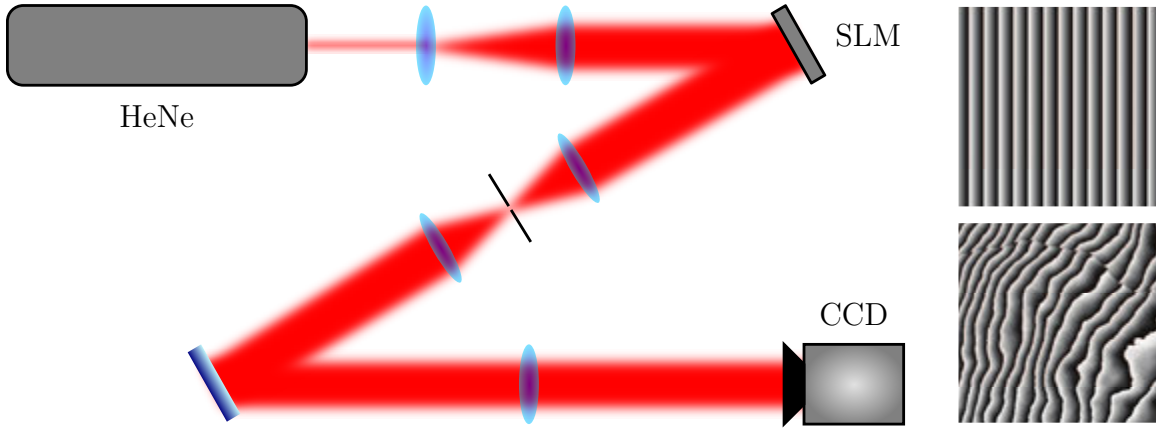


Figure 4.7: Left: an experimental setup used to simulate a channel with thin-phase turbulence. Right: typical blazed grating holograms used to generate a plane-wave mode with (top) and without (bottom) turbulence.

We can simulate a turbulence channel in the same way that was done in the previous section. A schematic of the setup is shown in Fig. 4.7. This setup is identical to the setup used before except there is no mode transformer, as the plane wave states can be sorted directly with a Fourier transforming lens and spatially binned with a CCD. A typical hologram used to generate the mode is also shown both with and without the addition of a random turbulence screen. As before, the inherent crosstalk primarily due to diffraction overlap of the modes at the CCD are measured and taken into account theoretically via Eq. (4.20).

The results for the plane-wave case are also plotted in Fig. 4.8 and are qualitatively very similar to the effects on OAM encoding. An interesting point concerning the studies using alternative encoding is that the optimal modes for communication considering diffraction (i.e. communication modes), are not in general the modes that are most robust against the effects of turbulence. Also shown in Fig. 4.8 is a plot of

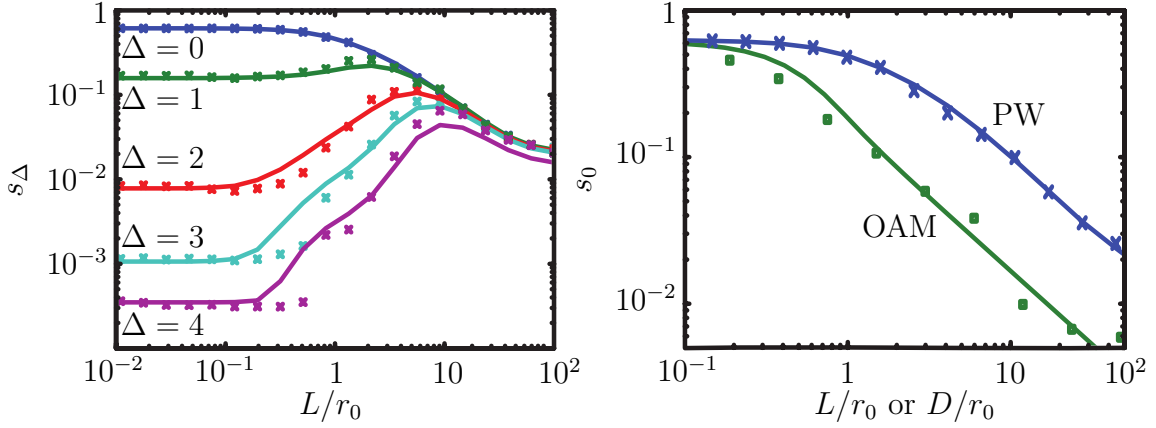


Figure 4.8: Left: the average plane-wave power spectrum s_Δ detected in plane-wave mode $m + \Delta$ is plotted as a function of turbulence strength L/r_0 for an input mode with $m = 0$. Experimental data (crosses) is co-plotted with the theoretical prediction given by Eq. (4.25) (line). Right: s_0 for OAM (dashed line) and plane-wave (solid line) encodings demonstrating the additional robustness of plane-wave modes against the effects of turbulence.

$\langle s_0 \rangle$ for both the OAM and plane-wave schemes to emphasize the fact that plane-wave crosstalk will be equal to the case using OAM for a turbulence strength more than 3 times that of OAM i.e. plane-wave encoding can withstand turbulence that is 3 times stronger than OAM for the same acceptable error rate. We believe physically this is due to the fact that turbulence is dominated by low order aberrations, specifically by tip-tilt [63]. A one dimensional plane-wave encoding in x will be affected by x tilt but not y , whereas an OAM beam is equally effected by x or y tilts.

As before, knowing s_Δ for all the input modes allows us to compute the channel capacity as a function of the turbulence strength L/r_0 . A plot of the results for a number of different alphabet sizes N are shown in Fig. 4.9. Also shown is the equivalent channel capacities using OAM rather than plane-wave encoding demonstrating the

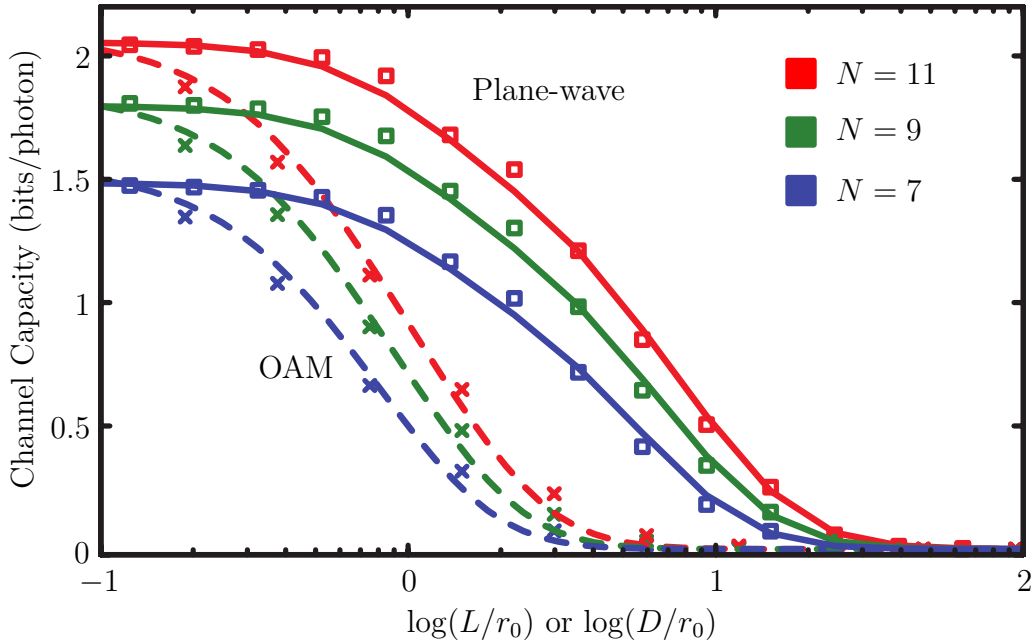


Figure 4.9: Plots of the channel capacities per symbol for both plane-wave (solid lines) and OAM (dashed lines) encoding as a function of the turbulence strength L/r_0 or D/r_0 for N total states.

increased robustness of the plane-wave encoding to the deleterious effects of turbulence as compared with OAM.

4.3 Thick turbulence

The thin-phase model presented in the previous chapter allows for a simple representation of turbulence that makes the analysis of systems with turbulence more tractable. However this simplicity comes at the cost of ignoring many additional physical effects caused by turbulence. In more realistic situations, such as communication along a long horizontal path through which the turbulence is continuously distributed, one will see additional effects such as those described in section 4.1 in addition to the

problems caused by pure phase fluctuations. Additionally, the thin-phase model is not very useful in analyzing systems with active compensations, such as by a phase-only AO. Such a compensation trivially counters the effects of thin-phase turbulence by the application of an equal and opposite phase to cancel $\phi(\mathbf{r})$.

The propagation of an optical beam through thick turbulence is not in general analytically solvable and thus requires either simulation or testing in a real world setup. The cost and lack of control of testing in a real-world setup makes finding suitable methods of simulating turbulence highly desirable for understanding this problem. In this section we describe a method we developed for simulating a thick turbulence channel and show how this can be implemented in a laboratory setup (section 4.3.1) [8]. To demonstrate the power of this method we simulate a one kilometer long free-space OAM-based communication link; these results are presented in section 4.3.2.

4.3.1 Simulating thick turbulence

To examine the effects that a thick horizontal turbulent path might have on OAM-based communication channel while still allowing information transfer and AO correction, we chose to consider a one kilometer path L with aperture sizes of the sender and receiver of $D = 18.2$ cm, at a wavelength of $\lambda = 785$ nm corresponding to a Fresnel number product of

$$D_f = \left(\frac{\pi D^2}{4\lambda L} \right)^2 \approx 1100, \quad (4.26)$$

which supports OAM modes up to (via Eq. (2.145))

$$N \approx \sqrt{2D_F} \approx 50 \quad (4.27)$$

To allow for such a system to be realized in a laboratory setting, one must find a way to incorporate turbulence into the channel, as well as properly scale the system down to more manageable length scales. This section describes a method of emulating a thick turbulence path with 2 thin phase screens that can be represented in the lab with spatial light modulators (SLMs). Scaling rules that are invariant under Fresnel propagation are also detailed below.

Two phase-screen model

We have found that through use of two phase screens we can accurately model the horizontal turbulent channel, faithfully reproducing all of its relevant statistical properties. Specifically we require this path to have the same values for r_0 , σ_χ^2 , and σ_P^2 as described in section 4.1.

We can represent these 3 parameters by using thin Kolmogorov phase screens each with its own value of r_0 . The values of r_0 for each screen, as well as each screen's position along the path, give us 4 independent parameters that can be tuned until the two-screen path reproduces the same 3 parameters of the full horizontal channel. This still gives us an additional degree of freedom, and since phase vortices in $\phi(\mathbf{r})$ create

significant problems for AO correction as well as for OAM based encoding [65–68], we choose the density of branch points, ρ_{BP} , as our fourth parameter to constrain the problem.

For a horizontal path with a constant value of the refractive index structure parameter

$$C_n^2 = 1.8 \times 10^{-14} \text{ m}^{-2/3}, \quad (4.28)$$

which represents a typical horizontal path near ground level, we compute the parameters given in Eqs. (4.7) – (4.11). The computed values are

$$r_0 = 24.4 \text{ mm}, \quad \sigma_\chi^2 = 0.197, \quad \text{and} \quad \sigma_p^2 = 7.04 \times 10^{-3}. \quad (4.29)$$

By Monte-Carlo simulation the density of branch points in $\phi(\mathbf{r})$ is found to be

$$\rho_{\text{BP}} = 500 \text{ m}^{-2}. \quad (4.30)$$

Physically this means that a typical realization of turbulence will create thirteen phase vortices within the receiver’s aperture, which one could imagine being a serious impediment to one’s ability to measure the intended phase vortex of the original transmitted OAM state.

The second step in designing the two-phase-screen model is to find the values for the position and r_0 for each screen that will give the same values of r_0 , σ_χ , σ_p , and

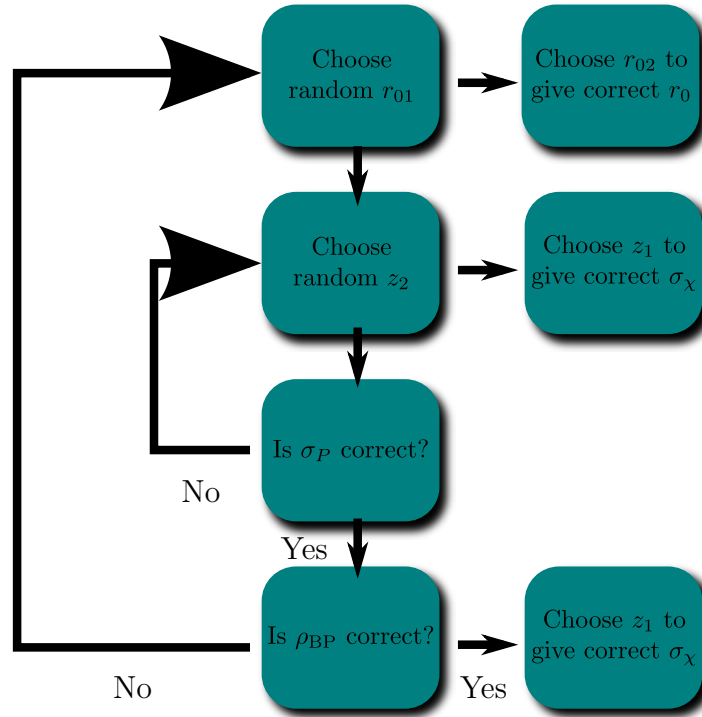


Figure 4.10: Procedure used to compute Fried's parameters and positions of the two thin phase screens needed to reproduce r_0 , σ_χ , σ_p , and ρ_{BP} of the equivalent thick channel.

ρ_{BP} of the thick path. The procedure is diagrammed in Fig. 4.10. One starts with an initial guess for r_{01} (i.e. r_0 for screen one), and then solves for the value of r_{02} that will give the correct value for D/r_0 . Next, one randomly picks a value for the position of the second screen, z_2 , and finds z_1 such that one gets the correct value for σ_χ . z_2 is then varied (along with z_1 to maintain σ_χ) to set the correct value for σ_p . Given this solution, ρ_{BP} is computed by Monte-Carlo simulation. If at this point we get the correct ρ_{BP} , a solution has been found; otherwise one starts over with a new choice for r_{01} . Using this procedure we found we could simulate our one kilometer path with

the parameters (measured from the sender's aperture)

$$r_{01} = 3.926 \text{ cm}, \quad r_{02} = 3.503 \text{ cm}, \quad z_1 = 171.7 \text{ m}, \quad \text{and} \quad z_2 = 769 \text{ m}. \quad (4.31)$$

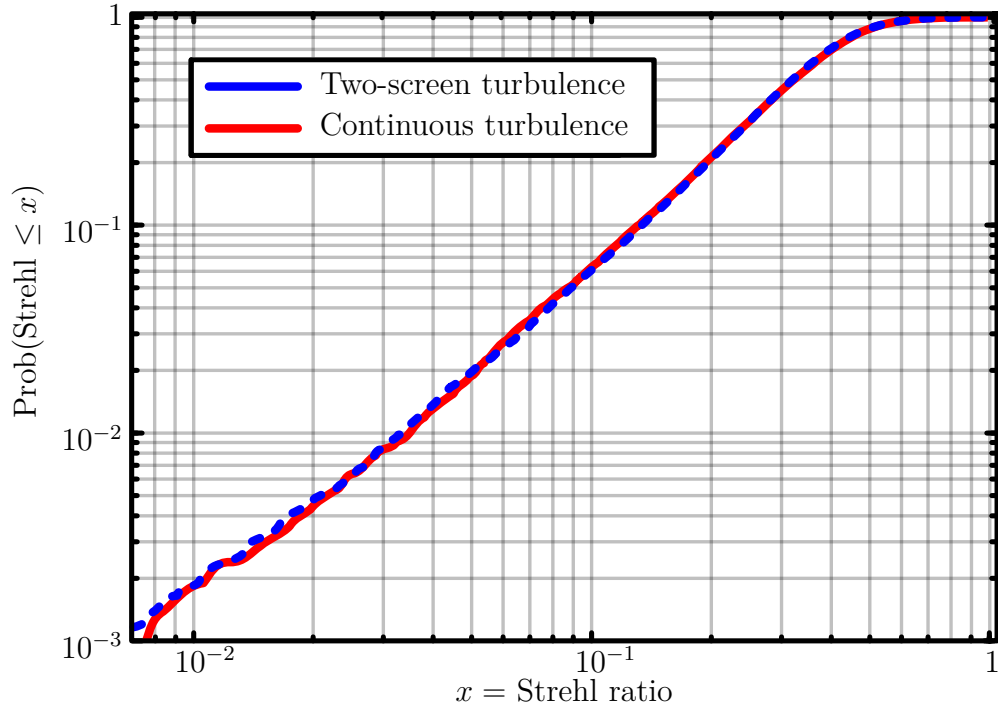


Figure 4.11: Cumulative distribution function of the Strehl ratio for a thick turbulent path represented by ten Kolmogorov phase screens (solid red line) and its equivalent two phase screen solution (dashed blue line).

As an independent test of this solution, a beam propagation simulation was performed to compare a thick turbulent path with the analogous two-screen solution. The continuous path was simulated using a standard split-step method in which the path L is broken up into N discrete steps. Each of the N sections of turbulent atmosphere is replaced by non-turbulent propagation followed by an effective thin random phase screen that represents the effects of refractive index fluctuations within

the slab. The propagation through a slab can be approximated by a thin screen so long as the scintillation due to propagation after encountering a random phase is negligible. As a rule of thumb one must require that the scintillation due to propagation through the slab must be less than ten percent of the total amount [73] in order to be able to represent the slab by a single screen, which is quantified as

$$\sigma_x^2(L/N) < 0.1\sigma_x^2(L). \quad (4.32)$$

We choose $N = 10$, which for the horizontal path considered here becomes by Eq. (4.9)

$$\sigma_x^2(L/N)/\sigma_x^2 = N^{-11/6} \approx 0.01 \ll 0.1. \quad (4.33)$$

In each simulation a different random realization of turbulence was made and the Strehl ratio, defined as the ratio of the peak intensity to ideal peak intensity of a spot at a focal plane of the receiver, was computed. By repeating this many times, a probability distribution for the Strehl ratio was found and the results are shown in Fig. 4.11. As can be seen in the plot, the Strehl ratios of the two-screen and the ‘continuous,’ ten-screen paths show very good agreement with each other. This result demonstrates that the two-screen model not only reproduces the correct mean values for the statistical parameters of interest (by construction), but can also be expected to give similar distributions of possible measurement outcomes.

Fresnel scaling

The second thing that must be done to effectively simulate a turbulent path in a laboratory setting is to scale the optical paths down to more manageable lengths. In order to ensure that the scaled path still represents the desired physical path, the propagation must remain invariant under the scaling.

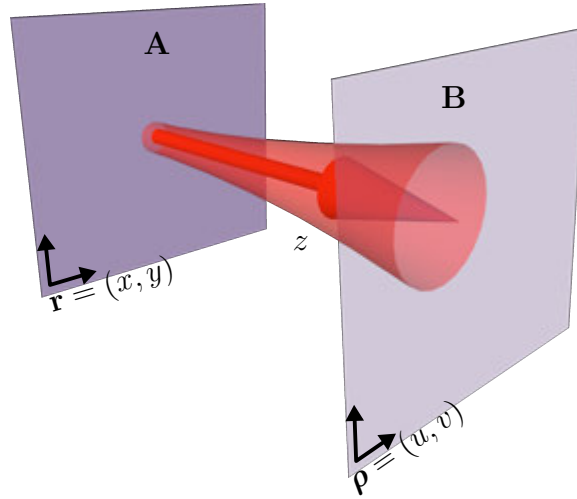


Figure 4.12: Propagation from plane **A**, described by coordinates $r = (x, y)$, to plane **B** with coordinates $\rho = (u, v)$

Fresnel propagation from one plane to another a distance z away as shown in Fig. 4.12 is given by:

$$U_B(\boldsymbol{\rho}) = \frac{ie^{ikz}}{\lambda z} \int U_A(\mathbf{r}) e^{\frac{i\pi}{\lambda z}(\mathbf{r}-\boldsymbol{\rho})^2} d\mathbf{r} \quad (4.34)$$

Now if we scale the coordinates using

$$\mathbf{r}' = \alpha_r \mathbf{r}, \quad \boldsymbol{\rho}' = \alpha_\rho \boldsymbol{\rho}, \quad \text{and} \quad z' = \alpha_z z, \quad (4.35)$$

then the above propagation equation becomes

$$U_B\left(\frac{\boldsymbol{\rho}'}{\alpha_\rho}\right) = \frac{ie^{ikz'/\alpha_z}}{\alpha_r\lambda z'/\alpha_z} \int U_A\left(\frac{\mathbf{r}'}{\alpha_r}\right) e^{\frac{i\pi\alpha_z}{\lambda z'}\left(\frac{\mathbf{r}'}{\alpha_r}-\frac{\boldsymbol{\rho}'}{\alpha_\rho}\right)^2} d\mathbf{r}' \quad (4.36)$$

Since we require the Fresnel number to remain constant then

$$\alpha_z = \alpha_\rho\alpha_r. \quad (4.37)$$

Now we can rewrite equation 4.36 as

$$\frac{e^{ikz'(1-1/\alpha_z)}}{\alpha_\rho} U_B\left(\frac{\boldsymbol{\rho}'}{\alpha_\rho}\right) = e^{-i\frac{\pi\rho'^2}{\lambda f_\rho}} \left(\frac{ie^{ikz'}}{\lambda z'} \int U_A\left(\frac{\mathbf{r}'}{\alpha_r}\right) e^{-i\frac{\pi\mathbf{r}'^2}{\lambda f_r}} e^{\frac{i\pi}{\lambda z'}(\mathbf{r}'-\boldsymbol{\rho}')^2} d\mathbf{r}' \right) \quad (4.38)$$

where

$$f_\rho = \frac{z'}{1-\frac{\alpha_r}{\alpha_\rho}} \quad \text{and} \quad f_r = \frac{z'}{1-\frac{\alpha_\rho}{\alpha_r}}. \quad (4.39)$$

From Eq. 4.38 we see that the horizontal path between planes **A** and **B** can be scaled down (to within a scaling and phase constant) simply by adding a lens with focal length f_r at *A*, propagating a distance z' , and then adding another lens with focal length f_ρ at *B* to cancel out the residual quadratic phase.

4.3.2 OAM encoding with thick-phase turbulence

A diagram of our experimental setup is presented in Fig. 4.13. Alice prepares the beam in a specific OAM mode using a blazed hologram as described in chapter 3 to send to

Bob. The prepared state is then sent through the simulated one kilometer path scaled down as described in section 4.3.1 to a total length of 1.3 m. The two thin-phase screens used to simulate thick turbulence in our setup were implemented using an SLM in a double-pass configuration. In addition, the quadratic phases required for proper scaling of the propagation path were added to the phases on the SLMs.

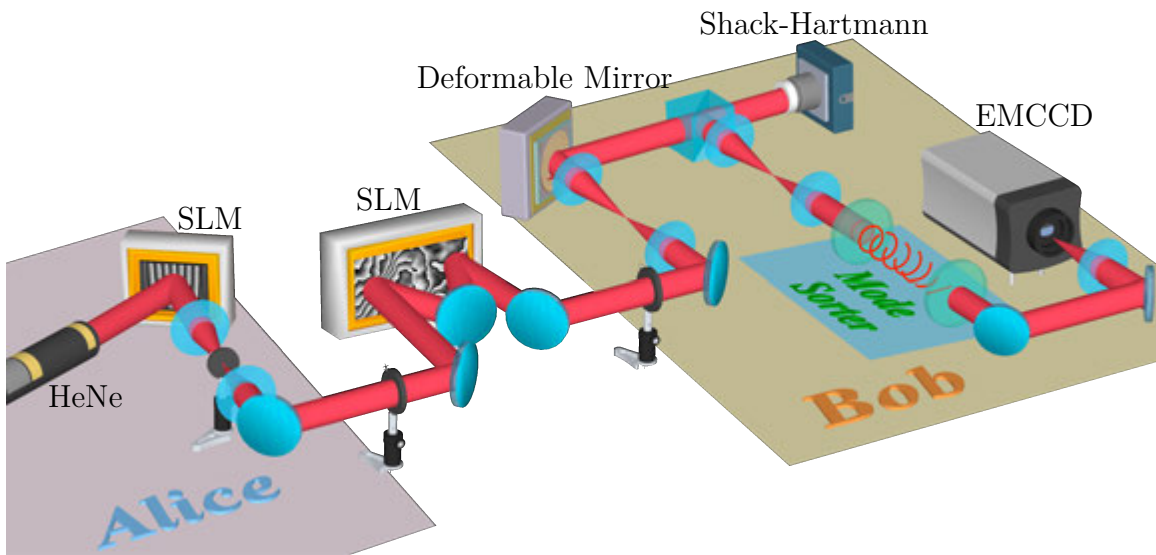


Figure 4.13: Alice sends a beam prepared in a specific OAM state ℓ to Bob. Bob receives the beam after propagation through a channel representing a 1,km turbulence path. The beam is (optionally) corrected using a deformable mirror and sent to a sorter to make a measurement of the of the OAM spectrum of the beam.

After propagation through the turbulent channel, the beam at Bob's aperture is imaged with a $4f$ system onto a Thorlabs adaptive optics kit consisting of a 12×12 actuator deformable mirror and a Shack-Hartmann wavefront sensor. After the AO system, the beam is similarly imaged onto the first element OAM sorter and the we followed the same procedure for measuring the OAM power spectrum as was described in section 4.2.

In order to examine the effects of the turbulent channel on OAM communication, we experimentally measured the OAM spectrum that Bob detects conditioned on what Alice sent. In a perfect channel, if Alice sends OAM mode s , then Bob will measure an OAM spectrum that is simply a Kronecker delta centered at the same mode. However, in an imperfect or turbulent channel, there will be some spreading into neighboring OAM modes to the prepared state. The conditional probability matrix, $p(d|s)$ where d is the detected OAM mode and s is the sent mode, provides a natural expression for this crosstalk induced by the imperfections or turbulence in the channel.

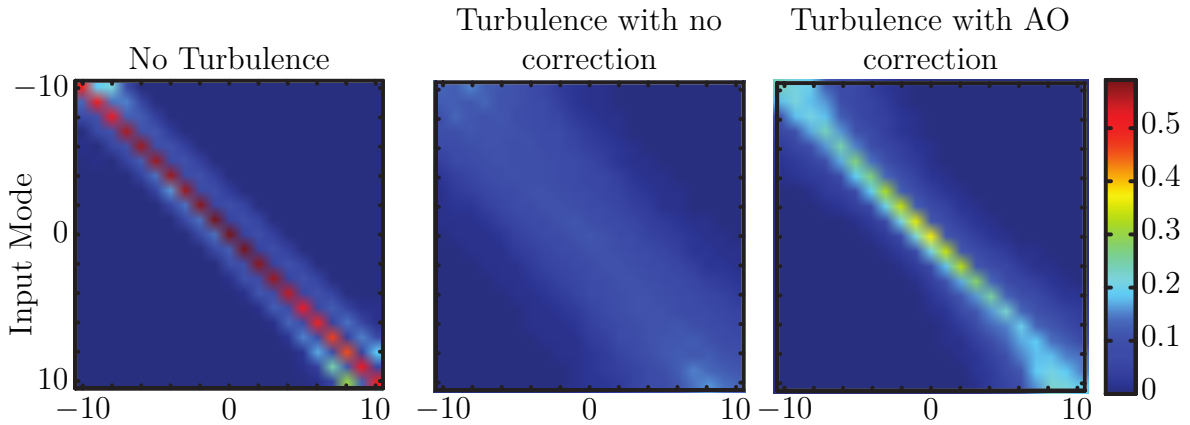


Figure 4.14: Measurement of the crosstalk in the channel represented by the conditional probability matrix, $p(d|s)$ for three cases: Left: no turbulence, Middle: with turbulence, and Right: with turbulence and adaptive correction.

The conditional probability matrix $p(d|s)$ is plotted for 3 different scenarios in Fig. 4.14. The left plot shows $p(d|s)$ when there is no turbulence in the channel, showing only crosstalk due to any misalignment in the system and inherent crosstalk of the sorter. The middle plot shows the effects of thick turbulence ensemble averaged over 100 realizations, which act to greatly spread the signal over many neighboring

channels. This selective spreading of OAM into neighboring modes rather than randomly into any OAM state is qualitatively similar to what is seen in the thin turbulence regime demonstrated in section 4.2. For the third case shown in the right plot, adaptive correction was applied to the turbulence with the AO system, allowing much of the signal to be recovered. The phase aberrations induced from each realization of turbulence was sensed and corrected by the AO using the OAM $\ell = 0$ mode. Each mode was then sent through the channel and AO system, and the OAM spectrum was measured by Bob. This procedure was repeated and averaged over fifty realizations of turbulence.

From Fig. 4.14 we can qualitatively see that thick turbulence greatly degrades the quality of the channel. In order to quantify the crosstalk induced by the turbulence as well as the quality of the AO correction, we compute the mutual information between Alice and Bob for all three cases above. We quantify these results by calculating the mutual information as a function of the encoding dimension N . The mutual information for the three cases of no turbulence, thick turbulence, and turbulence with AO correction, is plotted in the left plot of Fig. 4.15 as a function of N . One can see that the AO system allows us to cancel roughly half of the loss of channel capacity due to turbulence.

Further, since turbulence preferentially scatters power into neighboring OAM modes as was found to be the case in the thin turbulence model of section 4.2 one can also increase the channel capacity by choosing to use a less dense set of OAM

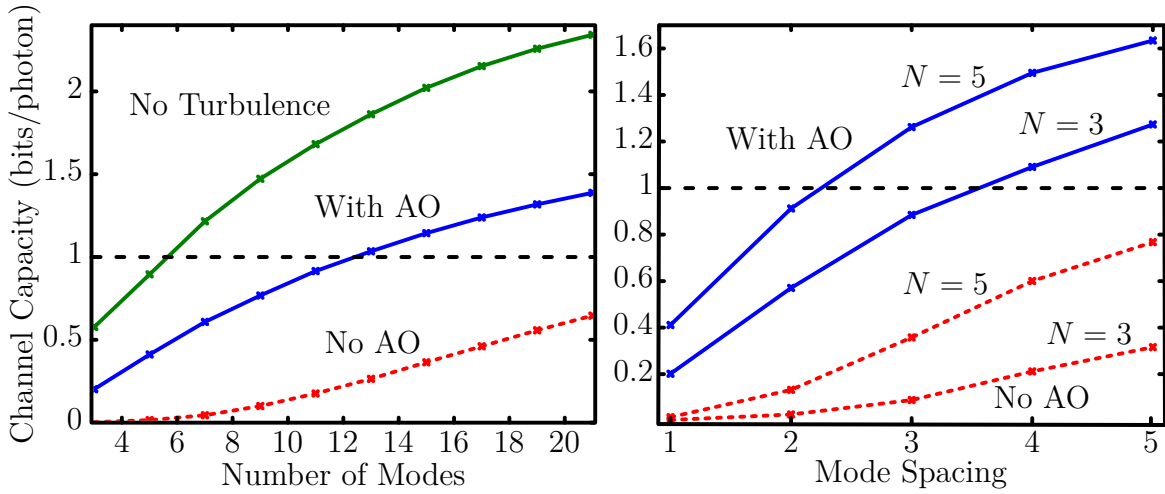


Figure 4.15: Left: measured channel capacity as a function of the number of OAM modes N used for the spatial encoding. Right: measured channel capacity as a function of the spacing between OAM modes used for communication for alphabet size N . Channel capacities without AO correction is shown as the red dotted line, while with AO is shown as the solid blue line. Also for reference is an ideal channel capacity using a binary alphabet.

modes for thick turbulence as well. Changing the encoding is also independent of any AO system one may use, and thus a modified encoding can be used along with AO correction to further enhance the channel capacity. The plot in the right panel of Fig. 4.15 shows the increase in the mutual information one can obtain for a given number of encoded modes, N . The channel capacity of an ideal binary encoded system is shown for reference. It is worth noting that the use of spatial mode encoding shows an improvement over such a system with very moderate resources (i.e. three modes with a channel spacing of four or more).

Chapter 5

Conclusions and Future Work

In this thesis I've tried to demonstrate that Shannon's theory of information provides a toolbox with which to understand, analyze, and motivate research within the field of optics in a general and powerful way. As a framework, this work is naturally open-ended with possible future work in any number of different possible directions.

The most obvious future application of this work is to try to apply the reasoning to other degrees of freedom of an electromagnetic field. This thesis focused specifically on the transverse degree of freedom of a paraxial propagating beam, but one could equally well consider non-paraxial three dimensional fields as well. In addition, within any single spatial mode there exists a continuum of amplitude values as well as temporal states that could be analyzed. One could also consider fields that are not propagating in free-space, but rather propagate in material or metamaterials (either freely or in bound modes). Finally, multiple degrees of freedom could be analyzed together both in terms of simply treating the problem as existing in a higher dimensional state space

comprised of multiple degrees of freedom, as well as considering one degree of freedom as a tool for simply multiplexing multiple similar channels together in the other degree of freedom.

Chapter 2 gave a theoretical analysis of the fundamental information limits of a paraxial free-space channel by introducing the concept of communication modes which are the normal modes of the Green's function description of the channel. The communication modes and corresponding information capacities were computed for both Gaussian apodized, as well as hard aperture channels containing both cylindrical and Cartesian geometries. Future work could of course be extended to any system that can be described using a deterministic Green's function or operator.

In this thesis only system Green's functions that were stationary in time were considered in computing the communication modes. Future work could look at situations in which this is not true, which would physically represent a system that changes in time. The corresponding communication modes would then also be expected to change in time as well. Alternatively one could consider a non-stationary systems in which Alice and Bob only have average or statistical information about the system, such as the case for a system with turbulence, and ask if there exist average (or perhaps partially coherent) modes that represent the best average modes with which to communicate.

Chapter 3 described the implementation of a free-space quantum key distribution system. First, I reviewed methods of mode generation using spatial diffracting gratings

via spatial light modulators. This concluded with a demonstration of how one could use digital micromirror devices to enable rapid generation of spatial modes or generation of spatial modes with arbitrary spatial coherence properties. Future directions could focus on alternative or faster methods of spatial light modulation, such as with static elements and faster modulations methods (such as electro-optic modulators) in order to increase the channel information rate.

Chapter 3 also introduced the problem of efficiently sorting and discrimination of spatial modes. This problem has practical solutions for only a handful of known sets of spatial modes, most notably the orbital angular momentum states that were the focus of much of this work. Algorithms for finding practical solutions for any general basis set of orthogonal modes, or even solutions for other specific bases, is an still an open problem.

The final part of this thesis (chapter 4) looked at the effects a stochastic or turbulent channel has on the information capacity of spatial mode encoding. Theoretically, this is a difficult problem that requires many approximations if one does not want to resort to direct simulation or prototyping. For instance, thin phase models allow for analytic computation of some of the statistical effects, but modeling general propagation through a random medium is still considered an open problem.

This chapter also looked at passive methods of compensation by choosing alternative encoding schemes, such as using fewer modes or using a set of modes other than communication modes. Future work could explore finding an optimal or ideal

set of modes to use for a given turbulent channel (either via a generalization to the communication modes or some other method). Active methods of turbulence compensation using a simple adaptive optics setup to compensate phase fluctuations was also looked at. More sophisticated schemes, such as multi-conjugate adaptive optics would be an appropriate area of further research.

References

- [1] M. Mirhosseini, O. S. Magaña Loaiza, C. Chen, B. Rodenburg, M. Malik, and R. W. Boyd. Rapid generation of light beams carrying orbital angular momentum. *Optics Express* **21**, 30196. doi:10.1364/OE.21.030196 (2013).
- [2] B. Rodenburg, M. Mirhosseini, O. S. Magaña Loaiza, and R. W. Boyd. Experimental generation of an optical field with arbitrary spatial coherence properties. *Journal of the Optical Society of America B* **31**, A51. doi:10.1364/JOSAB.31.000A51 (2014).
- [3] M. Mirhosseini, O. S. Magaña Loaiza, M. N. O’Sullivan, B. Rodenburg, M. Malik, D. J. Gauthier, and R. W. Boyd. High-dimensional quantum cryptography with twisted light. *arXiv:1402.7113* (2014).
- [4] R. W. Boyd, B. Rodenburg, M. Mirhosseini, and S. M. Barnett. Influence of atmospheric turbulence on the propagation of quantum states of light using plane-wave encoding. *Optics Express* **19**, 18310. doi:10.1364/OE.19.018310 (2011).
- [5] B. Rodenburg, M. P. J. Lavery, M. Malik, M. N. O’Sullivan, M. Mirhosseini, D. J. Robertson, M. J. Padgett, and R. W. Boyd. Influence of atmospheric turbulence on states of light carrying orbital angular momentum. *Optics Letters* **37**, 3735. doi:10.1364/OL.37.003735 (2012).
- [6] M. Malik, M. N. O’Sullivan, B. Rodenburg, M. Mirhosseini, J. Leach, M. P. J. Lavery, M. J. Padgett, and R. W. Boyd. Influence of atmospheric turbulence on optical communications using orbital angular momentum for encoding. *Optics Express* **20**, 13195. doi:10.1364/OE.20.013195 (2012).
- [7] M. Mirhosseini, B. Rodenburg, M. Malik, and R. W. Boyd. Free-space communication through turbulence: a comparison of plane-wave and orbital-angular-momentum encodings. *Journal of Modern Optics* **61**, 43–48. doi:10.1080/09500340.2013.834084 (2014).

- [8] B. Rodenburg, M. Mirhosseini, M. Malik, O. S. Magaña Loaiza, M. Yanakas, L. Maher, N. K. Steinhoff, G. A. Tyler, and R. W. Boyd. Simulating thick atmospheric turbulence in the lab with application to orbital angular momentum communication. *New Journal of Physics* **16**, 033020. doi:10.1088/1367-2630/16/3/033020 (2014).
- [9] C. E. Shannon. A mathematical theory of communication. *Bell System Technical Journal* **27**, 379–423 (1948).
- [10] C. E. Shannon. Coding theorems for a discrete source with a fidelity criterion. *IRE Nat. Conv. Rec* **4**, 142–163. doi:10.1234/12345678 (1959).
- [11] M. Nielsen and I. Chuang. *Quantum Computation and Quantum Information*. Cambridge University Press (2010).
- [12] C. H. Bennett and G. Brassard. Quantum cryptography: Public key distribution and coin tossing. *Proceedings of IEEE International Conference on Computers Systems and Signal Processing* **175**, 175–179 (1984).
- [13] M. Bourennane, A. Karlsson, and G. Björk. Quantum key distribution using multilevel encoding. *Physical Review A* **64**, 012306. doi:10.1103/PhysRevA.64.012306 (2001).
- [14] N. Cerf, M. Bourennane, A. Karlsson, and N. Gisin. Security of Quantum Key Distribution Using d-Level Systems. *Physical Review Letters* **88**. doi:10.1103/PhysRevLett.88.127902 (2002).
- [15] J. Wang, J.-Y. Yang, I. M. Fazal, N. Ahmed, Y. Yan, H. Huang, Y. Ren, Y. Yue, S. Dolinar, M. Tur, and A. E. Wilner. Terabit free-space data transmission employing orbital angular momentum multiplexing. *Nature Photonics* **6**, 488–496. doi:10.1038/nphoton.2012.138 (2012).
- [16] R. W. Boyd, A. Jha, M. Malik, C. O’Sullivan, B. Rodenburg, and D. J. Gauthier. Quantum key distribution in a high-dimensional state space: exploiting the transverse degree of freedom of the photon. *Proceedings of SPIE* **7948**, 79480L–6. doi:10.1117/12.873491 (2011).
- [17] S. Etcheverry, G. Cañas, E. S. Gómez, W. A. T. Nogueira, C. Saavedra, G. B. Xavier, and G. Lima. Quantum key distribution session with 16-dimensional photonic states. *Scientific reports* **3**, 2316. doi:10.1038/srep02316 (2013).
- [18] J. Mercer. Functions of Positive and Negative Type, and their Connection with the Theory of Integral Equations. *Philosophical Transactions of the Royal Society A: Mathematical, Physical and Engineering Sciences* **209**, 415–446. doi:10.1098/rsta.1909.0016 (1909).

- [19] P. Martinsson, P. Ma, A. Burvall, and A. T. Friberg. Communication modes in scalar diffraction. *Optik - International Journal for Light and Electron Optics* **119**, 103–111. doi:10.1016/j.ijleo.2006.07.009 (2008).
- [20] J. W. Goodman. *Introduction to Fourier Optics*. Roberts and Company Publishers, 3rd ed. (2004).
- [21] J. H. Shapiro, S. Guha, and B. I. Erkmen. Ultimate channel capacity of free-space optical communications [Invited]. *Journal of Optical Networking* **4**, 501. doi:10.1364/JON.4.000501 (2005).
- [22] G. N. Watson. Notes on Generating Functions of Polynomials: (2) Hermite Polynomials. *Journal of the London Mathematical Society* **s1-8**, 194–199. doi:10.1112/jlms/s1-8.3.194 (1933).
- [23] A. Thaning, P. Martinsson, M. Karelin, and A. T. Friberg. Limits of diffractive optics by communication modes. *Journal of Optics A: Pure and Applied Optics* **5**, 153–158. doi:10.1088/1464-4258/5/3/301 (2003).
- [24] D. Slepian and H. O. Pollak. Prolate spheroidal wave functions, Fourier analysis and uncertainty—I. *Bell System Technical Journal* **40**, 43–63 (1961).
- [25] G. T. di Francia. Degrees of Freedom of an Image. *Journal of the Optical Society of America* **59**, 799. doi:10.1364/JOSA.59.000799 (1969).
- [26] B. R. Frieden. VIII Evaluation, Design and Extrapolation Methods for Optical Signals, Based on Use of the Prolate Functions. *Progress in Optics* **9**, 311–407. doi:10.1016/S0079-6638(08)70049-0 (1971).
- [27] G. N. Watson. *A Treatise on the Theory of Bessel Functions*. Cambridge University Press, 2nd ed. (1966).
- [28] G. N. Watson. Notes on Generating Functions of Polynomials: (1) Laguerre Polynomials. *Journal of the London Mathematical Society* **s1-8**, 189–192. doi:10.1112/jlms/s1-8.3.189 (1933).
- [29] I. Kimel and L. Elias. Relations between Hermite and Laguerre Gaussian modes. *IEEE Journal of Quantum Electronics* **29**, 2562–2567. doi:10.1109/3.247715 (1993).
- [30] D. Slepian. Prolate spheroidal wave functions, Fourier analysis and uncertainty-IV: Extension to many dimensions; generalized prolate spheroidal functions. *Bell System Technical Journal* **43**, 3009–3057 (1964).
- [31] A. Karoui and T. Moumni. Spectral analysis of the finite Hankel transform and circular prolate spheroidal wave functions. *Journal of Computational and Applied Mathematics* **233**, 315–333. doi:10.1016/j.cam.2009.07.037 (2009).

- [32] M. Soskin and M. Vasnetsov. Singular Optics. *Progress in Optics* **42**, 219–276 (2001).
- [33] E. Noether. Invariant Variation Problems. *Nachrichten von der Gesellschaft der Wissenschaften zu Göttingen, Mathematisch-Physikalische Klasse* 235–257. doi:10.1080/00411457108231446 (1918).
- [34] L. Allen, M. Beijersbergen, R. Spreeuw, and J. P. Woerdman. Orbital angular momentum of light and the transformation of Laguerre-Gaussian laser modes. *Physical Review A* **45**, 8185–8189. doi:10.1103/PhysRevA.45.8185 (1992).
- [35] S. Van Enk and G. Nienhuis. Commutation Rules and Eigenvalues of Spin and Orbital Angular Momentum of Radiation Fields. *Journal of Modern Optics* **41**, 963–977. doi:10.1080/09500349414550911 (1994).
- [36] L. Allen, M. J. Padgett, and M. Babiker. The Orbital Angular Momentum of Light. *Progress in Optics* **39**, 291–372. doi:10.1016/S0079-6638(08)70391-3 (1999).
- [37] D. C. Chu, J. R. Fienup, and J. W. Goodman. Multiemulsion on-axis computer generated hologram. *Applied optics* **12**, 1386–8. doi:10.1364/AO.12.001386 (1973).
- [38] B. R. Brown and A. W. Lohmann. Complex Spatial Filtering with Binary Masks. *Applied Optics* **5**, 967–969. doi:10.1364/AO.5.000967 (1966).
- [39] J. A. Davis, D. M. Cottrell, J. Campos, M. J. Yzuel, and I. Moreno. Encoding Amplitude Information onto Phase-Only Filters. *Applied Optics* **38**, 5004. doi:10.1364/AO.38.005004 (1999).
- [40] E. Bolduc, N. Bent, E. Santamato, E. Karimi, and R. W. Boyd. Exact solution to simultaneous intensity and phase encryption with a single phase-only hologram. *Optics Letters* **38**, 3546–3549. doi:10.1364/OL.38.003546 (2013).
- [41] V. Arrizón, U. Ruiz, R. Carrada, and L. A. González. Pixelated phase computer holograms for the accurate encoding of scalar complex fields. *Journal of the Optical Society of America A* **24**, 3500. doi:10.1364/JOSAA.24.003500 (2007).
- [42] B. R. Brown and A. W. Lohmann. Computer-generated Binary Holograms. *IBM Journal of Research and Development* **13**, 160–168. doi:10.1147/rd.132.0160 (1969).
- [43] W.-H. Lee. High efficiency multiple beam gratings. *Applied Optics* **18**, 2152. doi:10.1364/AO.18.002152 (1979).
- [44] D. Dudley, W. M. Duncan, and J. Slaughter. Emerging digital micromirror device (DMD) applications. *Proc. SPIE* **4985**, 14–25. doi:10.1117/12.480761 (2003).

- [45] L. Mandel and E. Wolf. *Optical Coherence and Quantum Optics*. Cambridge University Press (1995).
- [46] E. Wolf. New spectral representation of random sources and of the partially coherent fields that they generate. *Optics Communications* **38**, 3–6. doi:10.1016/0030-4018(81)90295-9 (1981).
- [47] A. Starikov and E. Wolf. Coherent-mode representation of Gaussian Schell-model sources and of their radiation fields. *Journal of the Optical Society of America* **72**, 923. doi:10.1364/JOSA.72.000923 (1982).
- [48] A. Mair, A. Vaziri, G. Weihs, and A. Zeilinger. Entanglement of the orbital angular momentum states of photons. *Nature* **412**, 313–6. doi:10.1038/35085529 (2001).
- [49] M. Reck and A. Zeilinger. Experimental realization of any discrete unitary operator. *Physical Review Letters* **73**, 58–61. doi:10.1103/PhysRevLett.73.58 (1994).
- [50] J. Leach, M. Padgett, S. Barnett, S. Franke-Arnold, and J. Courtial. Measuring the Orbital Angular Momentum of a Single Photon. *Physical Review Letters* **88**, 257901. doi:10.1103/PhysRevLett.88.257901 (2002).
- [51] M. P. J. Lavery, D. J. Robertson, G. Berkhout, G. D. Love, M. J. Padgett, and J. Courtial. Refractive elements for the measurement of the orbital angular momentum of a single photon. *Optics Express* **20**, 2110. doi:10.1364/OE.20.002110 (2012).
- [52] G. Berkhout, M. P. J. Lavery, J. Courtial, M. Beijersbergen, and M. J. Padgett. Efficient Sorting of Orbital Angular Momentum States of Light. *Physical Review Letters* **105**. doi:10.1103/PhysRevLett.105.153601 (2010).
- [53] M. P. J. Lavery, D. Robertson, M. Malik, B. Robenburg, J. Courtial, R. W. Boyd, and M. J. Padgett. The efficient sorting of light’s orbital angular momentum for optical communications. *Proceedings of SPIE* **8542**, 85421R. doi:10.1117/12.979934 (2012).
- [54] O. Bryngdahl. Geometrical transformations in optics. *Journal of the Optical Society of America* **64**, 1092. doi:10.1364/JOSA.64.001092 (1974).
- [55] W. Hossack, A. Darling, and A. Dahdouh. Coordinate Transformations with Multiple Computer-generated Optical Elements. *Journal of Modern Optics* **34**, 1235–1250. doi:10.1080/09500348714551121 (1987).
- [56] M. N. O’Sullivan, M. Mirhosseini, M. Malik, and R. W. Boyd. Near-perfect sorting of orbital angular momentum and angular position states of light. *Optics Express* **20**, 24444. doi:10.1364/OE.20.024444 (2012).

- [57] M. Mirhosseini, M. Malik, Z. Shi, and R. W. Boyd. Efficient separation of the orbital angular momentum eigenstates of light. *Nature communications* **4**, 2781. doi:10.1038/ncomms3781 (2013).
- [58] L. C. Andrews and R. L. Phillips. *Laser Beam Propagation through Random Media*. Press Monographs. SPIE, 1000 20th Street, Bellingham, WA 98227-0010 USA, 2nd ed. (2005). doi:10.1117/3.626196.
- [59] S. M. Popoff, G. Lerosey, R. Carminati, M. Fink, A. C. Boccarda, and S. Gigan. Measuring the Transmission Matrix in Optics: An Approach to the Study and Control of Light Propagation in Disordered Media. *Physical Review Letters* **104**, 100601. doi:10.1103/PhysRevLett.104.100601 (2010).
- [60] J. J. Metzger, R. Fleischmann, and T. Geisel. Intensity Fluctuations of Waves in Random Media: What Is the Semiclassical Limit? *Physical Review Letters* **111**, 013901. doi:10.1103/PhysRevLett.111.013901 (2013).
- [61] A. N. Kolmogorov. The Local Structure of Turbulence in Incompressible Viscous Fluid for Very Large Reynolds Numbers. *Doklady Akademiia Nauk SSSR* **30**, 301–305. doi:10.1098/rspa.1991.0075 (1941).
- [62] V. I. Tatarski. *Wave Propagation in a Turbulent Medium*. McGraw-Hill Books (1961).
- [63] D. L. Fried. Statistics of a Geometric Representation of Wavefront Distortion. *Journal of the Optical Society of America* **55**, 1427. doi:10.1364/JOSA.55.001427 (1965).
- [64] B. M. Levine, E. A. Martinsen, A. Wirth, A. Jankevics, M. Toledo-Quinones, F. Landers, and T. L. Bruno. Horizontal Line-of-Sight Turbulence Over Near-Ground Paths and Implications for Adaptive Optics Corrections in Laser Communications. *Applied Optics* **37**, 4553. doi:10.1364/AO.37.004553 (1998).
- [65] D. L. Fried and J. L. Vaughn. Branch cuts in the phase function. *Applied Optics* **31**, 2865. doi:10.1364/AO.31.002865 (1992).
- [66] G. A. Tyler. Reconstruction and assessment of the least-squares and slope discrepancy components of the phase. *Journal of the Optical Society of America A* **17**, 1828. doi:10.1364/JOSAA.17.001828 (2000).
- [67] D. L. Fried. Branch point problem in adaptive optics. *Journal of the Optical Society of America A* **15**, 2759. doi:10.1364/JOSAA.15.002759 (1998).
- [68] C. A. Primmerman, T. R. Price, R. A. Humphreys, B. G. Zollars, H. T. Barclay, and J. Herrmann. Atmospheric-compensation experiments in strong-scintillation conditions. *Applied Optics* **34**, 2081. doi:10.1364/AO.34.002081 (1995).

- [69] A. T. Young. Seeing: its Cause and Cure. *The Astrophysical Journal* **189**, 587. doi:10.1086/152838 (1974).
- [70] D. L. Fried. Diffusion Analysis for the Propagation of Mutual Coherence. *Journal of the Optical Society of America* **58**, 961. doi:10.1364/JOSA.58.000961 (1968).
- [71] C. Paterson. Atmospheric Turbulence and Orbital Angular Momentum of Single Photons for Optical Communication. *Physical Review Letters* **94**, 153901. doi:10.1103/PhysRevLett.94.153901 (2005).
- [72] G. A. Tyler and R. W. Boyd. Influence of atmospheric turbulence on the propagation of quantum states of light carrying orbital angular momentum. *Optics Letters* **34**, 142. doi:10.1364/OL.34.000142 (2009).
- [73] J. M. Martin and S. M. Flatté. Intensity images and statistics from numerical simulation of wave propagation in 3-D random media. *Applied Optics* **27**, 2111–2126. doi:10.1364/AO.27.002111 (1988).